Spin Projection and Correlation Experiments in Nanoelectronic Devices

Inauguraldissertation

zur
Erlangung der Würde eines Doktors der Philosophie
vorgelegt der
Philosophisch-Naturwissenschaftlichen Fakultät
der Universität Basel

von

Arunav Bordoloi

2021

Genehmigt von der Philosophisch-Naturwissenschaftlichen Fakultät
auf Antrag von
Prof. Dr. Christian Schönenberger
Prof. Dr. Ilaria Zardo
Prof. Dr. Thomas Schäpers
Prof. Dr. Takis Kontos
Dr. Andreas Baumgartner

Basel, 15.09.2020

Prof. Dr. Martin Spiess
Dekan

Contents

1 Introduction

During the last 60 years, the world has witnessed a major revolution in the realm of microelectronic devices based on the flow of electron charges. Such relentless growth of digital microelectronics can be summarized by Moore's law [1, 2], which states that the number of transistors and microprocessors in an integrated chip will double about every two years due to device miniaturization. Yet Moore's law is starting to fail [3] as the size of devices approaches the dimensions of atoms. Therefore, potential replacements for traditional charge based electronics is actively sought after to enhance the computational power and functionality of devices. One such intrinsic property of the electron, known as *spin*, has been exploited to control electric currents for information processing [4–6]. The electron spin degree of freedom offers many advantages, such as long coherence times [7–9] for quantum computing [10], unlike charge states which gets easily destroyed by scattering with impurities, defects or other charges. These characteristics pave the path for more powerful and smaller devices in the field of spintronics [11–15] (or spin electronics) and the opportunity to exploit quantum mechanics in the ultimately powerful computing schemes, a quantum computer [16].

One such spin device already implemented for technological applications is based on the concept of *giant magnetoresistance* (GMR) [17, 18], where a non-magnetic metal layer is sandwiched between two ferromagnetic layers. The electrical current through this structure changes from small to large values depending on the relative magnetization orientation in the ferromagnetic layers. Such structures, known as *spin valves* [19–21], have resulted in extremely sensitive detectors of changing magnetic fields, resulting in new generations of read/write heads for data storage in hard-drives [22] as well as magnetoresistive random access memories (MRAMs) [23]. In addition, replacing the non-magnetic layer by a gate tunable semiconducting layer has enabled electric field control of the spin transport channel [24–26], a key ingredient essential for realization of heavily sought after Datta-Das spin field effect transistor[27–29]. Therefore, the spintronics community is primarily focused on developing such devices with larger well-controllable spin polarizations. One approach is to advance the existing GMR-based technology by developing new materials or by improving existing devices for better spin filtering , while the other approach is to find novel ways to generate and control spin polarized currents

[30, 31] for efficient spin valves and spin polarizers.

One such well-controlled platform to support single electron spins is quantum dots (QDs) in semiconductors [32, 33]. QDs, also known as artificial atoms, offer tunable discrete energy levels resulting from the confinement of electrons in all three spatial dimensions. All the parameters of a QD can be well controlled, such as the spin degenerate energy levels can be Zeeman split by an external magnetic field. This allows one to electrically control the spin polarized current through a QD, enabling one to achieve efficient spin injection and detection in spin valves as well as study various other phenomena such as spin orbit scattering [34–37], spin relaxation mechanisms [38–40], magnetic resonance [41] and spin dynamics in such nanostructures. In addition, the electrons in a QD can be used to form a *spin qubit* [42–45], a quantum mechanical two level system, which forms the basis for new and faster algorithms for quantum computing [46, 47], quantum cryptography [48] and teleportation [49].

A key element in such quantum computing applications is the ability to measure non-local correlations, known as *entanglement* [50], as well as reliably generate them. A naturally occurring source of entangled spin pairs is the superconducting condensate, from which spin singlet Cooper pairs [51] can be split into two QDs on each side of a s-wave superconductor. Such Cooper pair splitter (CPS) devices have already been demonstrated in various systems, such as InAs nanowires (NWs) [52–57], carbon nanotubes (CNTS) [58, 59] and graphene [60, 61]. A strong charge current correlation between the two output terminals has been demonstrated already [59], but a spin correlation, as expected for split singlet states, is missing and is even conceptually problematic so far. Such spin correlation measurements, i.e. the expectation value of the product of spin projection operators $\langle \sigma_1 \otimes \sigma_2 \rangle$ of the two QDs in a CPS device, requires efficient spin readout of the split electrons without destroying the superconducting state of the emitter. The idea is to use the two QDs for spin filtering [62–64], achievable by applying locally different magnetic fields. A lower CPS current is then expected for the parallel spin projection axes with respect to the antiparallel ones. In general, the most essential requirements for such an complex experiment can be summarized as: (1) highly polarized QDs with large electrical tunability of the QD spin polarization for efficient spin detection in close proximity to a superconductor; (2) coexistence of superconductivity and locally varying magnetic fields in close proximity to each other, such that the critical field of the superconductor is much higher than the local magnetic field strength; and (3) the CPS current in both QDs should exhibit non-local spin correlations in a specific pattern, i.e. higher for antiparallel spin projection axes.

In this thesis, we investigate all the above criteria using electron spin transport through engineered QDs in InAs NWs, chosen predominantly due to their large g-factors in QDs [65, 66] . We first show a new approach to control elec-

tron spin currents in QDs using stray magnetic fields locally generated from individual nanomagnets. Using this approach, we demonstrate electrically tunable highly efficient spin injection and detection in a double quantum dot spin valve (DQD-SV). We then use this efficient spin detection technique in a Cooper pair splitter device to perform spin readout and filtering of the CPS conductance signal. In addition, electron spin state engineering at very large magnetic fields through the Pauli spin blockade (PSB) effect is also presented.

Outline of the thesis

This thesis starts with an introduction to the relevant theoretical concepts in **Chapter 2**. A concise description of electron transport in single and double quantum dots is presented, followed by a brief introduction to ferromagnetism. Then, various concepts and phenomena associated with ferromagnetic devices, such as spin valve structures, tunneling magnetoresistance (TMR), magneto-Coulomb effect, are discussed. In addition, a brief introduction to superconductivity and Cooper pair splitting with quantum dots is introduced. In **Chapter 3**, an overview of the most important fabrication techniques and experimental setup is shown, with the exact fabrication recipes presented in Appendix A. The deposition of InAs NWs and fabrication of the ferromagnetic split gates are shown, followed by a description of the low temperature measurement setup. **Chapter 4** presents a brief description on the growth and electronic properties of the InAs NWs used in this thesis. In addition, a brief summary of magnetotransport experiments with InAs NWs is presented. In **Chapter 5**, we investigate the magnetoconductance (MC) of a single QD in the presence of a reversible stray magnetic field locally generated from Permalloy nanomagnets, which we term as ferromagnetic split gates (FSGs). We determine the characteristic switching field of the FSG and the generated stray field in the FSG gap as well as far away from the FSGs. In addition, magnetoconductance experiments with cobalt FSGs are also shown. **Chapter 6** presents an alternative route for spin injection and detection in InAs NWs using two such Zeeman split QD-FSG units in a double quantum dot spin valve (DQD-SV). We show that the magnetization orientation of the two FSGs can be reoriented individually, enabling us to access four magnetization states (two parallel and anti-parallel states) at zero external magnetic field. In tunneling magnetoresistance (TMR) experiments, we show an electrically tunable large TMR signal as well as large QD polarizations, signifying that the QD-FSG units can serve as highly efficient spin injectors and detectors. Using this spin detection technique, we perform spin readout of the CPS conductances in a CPS device in **Chapter 7**. We show coexistence of superconductivity and stray magnetic field in close proximity in our device and determine the CPS conductance change with the four FSG magnetization states. We observe a suppressed conductance for the parallel magnetization states with respect

to the antiparallel states, consistent with the interpretation of negative spin cross correlation between the split electrons. In **Chapter 8**, we present electron spin control at large magnetic fields by the Pauli spin blockade (PSB) effect in double quantum dots. We observe standard PSB at zero external magnetic field and a singlet-triplet transition of the DQD ground state at $B_{\text{S-T}} \approx 1.5\,\text{T}$. Beyond 1.5 T, we find an unconventional spin blockade effect with an odd number of total electrons in the double quantum dot.

Finally, we summarize the main findings of this thesis in **Chapter 9**, and present a brief outlook on further improvements and experiments.

2 Theoretical background

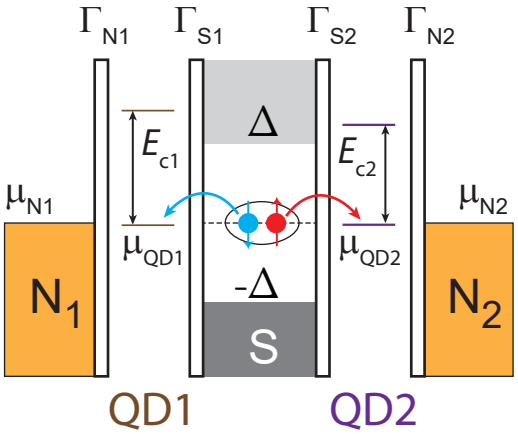

This chapter provides the most important theoretical concepts that are needed for the experiments presented in this thesis. First, an introduction to electron transport in single and double quantum dots is discussed. Second, a brief introduction to ferromagnetism is presented, followed by a description of the various experimental phenomena and concepts associated with ferromagnetic devices. In addition, a brief description of superconductivity and Cooper pair splitting with quantum dots is introduced. The quantum dots and superconductivity part partially follow the references [67–69], whereas the ferromagnetism part follows partially the reference [70] .

2.1. Quantum dots

Quantum dots (QDs) are a key ingredient in this thesis as they form an integral part of Cooper Pair splitters [52, 59]. Quantum dots are quasi-zero dimensional islands where the motion of electrons is confined in all three spatial dimensions resulting in their kinetic energies becoming quantized. As a result, their energy spectrum is quantized and are commonly referred to as 'artificial atoms' [33]. However in contrast to natural atoms, QDs can be coupled to source-drain electrodes and tuned by electrostatic gates, enabling us to investigate their electrical properties in transport experiments at low temperatures. QDs have been realized in different solid state systems, such as semiconducting nanowires[71–73], graphene nanoribbons [74], carbon nanotubes [75–77], two dimensional electron gases (2DEGs) [78–80] and two dimensional Van-der-Waals materials [81].

In a typical one dimensional system, for example, semiconducting nanowires (NWs), the electronic wavefunction along the radial direction is already quantized due to their small diameters, which are typically on the order of few tens of nanometers. In order to realize a QD, we need to introduce a confinement along the NW axis. Experimentally, this is achieved by either forming Schottky barriers [82], or by more controllable methods such as electrostatic gating and epitaxially defined in-situ grown tunnel barriers [72, 83]. At sufficiently low temperatures, the transport process across the metal-NW-metal nanostructure is dominated by tunneling events as the resistance of the NW-metal contact barriers are on the order of the resistance quantum, i.e., $R \geq h/e^2$. Such a system is equivalent to a particle-in-a-box problem [84], where the energy level spacing δE depends on the dispersion relation of the system, which in turn, depends on the precise geometry of the QD. Furthermore, the shell filling of the energy levels follow the Pauli exclusion principle, similar to atoms.

In order to completely describe a QD, we need to consider another phenomena along with quantum confinement: Coulomb interaction between the electrons. Due to their small size, the associated capacitance C of the island is small. The Coulomb interaction is then not negligible and can even be the dominating energy scale at low temperatures. This leads to a large energy cost, called the charging energy E_c, for adding or removing an electron from the island. This property, termed as Coulomb blockade (CB) [33], is the most universal property of a QD and discussed in detail in the next section. Therefore, an ideal QD would be weakly coupled to the metal contacts such that electrons can tunnel on and off the island, while keeping it isolated from the environment.

2.1.1. Coulomb blockade and single electron tunneling

The phenomena of Coulomb blockade can be well described within the framework of the constant interaction model (CIM) [32], which assumes that: (1) the capacitance C assigned to the dot is always constant, and (2) the energy

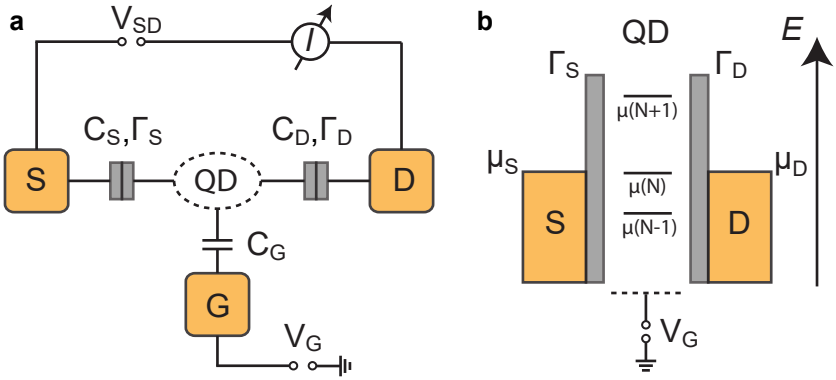

Figure 2.2. **a.** Capacitance model and typical measurement schematics of a single quantum dot coupled by two tunnel barriers with capacitive coupling $C_{S,D}$ and tunnel coupling strengths $\Gamma_{S,D}$ to a source (S) and drain (D) contact, respectively. A single gate (G) capacitively couples to the quantum dot (QD) with capacitance C_G allowing us to tune the electrochemical potential of the QD with voltage V_G. **b.** Illustration of the energy level diagram of a single QD showing the electrochemical potential energies $\mu(N)$ relative to those of the S-D contacts, $\mu_{S,D}$. Schematics adapted from Refs [33, 69, 85, 86].

spectrum of the QD is independent of the electron-electron interactions or electron number N of the QD [33, 84, 85]. Let us consider a typical QD device consisting of a single QD tunnel coupled to a source and drain contact with tunnel coupling strengths Γ_S, Γ_D and capacitive coupling with capacitances C_S and C_{SD}, respectively as shown in Fig. 2.2a. By applying a finite bias voltage $V_{SD} = V_S - V_D$, electrons can tunnel between the source and drain contacts through the QD. This allows us to measure the DC current I or differential conductance $G = dI/dV_{SD}$ across the quantum dot. The QD is simultaneously tuned by the gate voltage V_G, which is capacitively coupled to the dot with a capacitance C_G. The total capacitance of the QD is then given by: $C = \sum_i C_i = C_S + C_D + C_G$, and the total ground state energy of the dot with N charge carriers is:

$$E_{\mathrm{tot}}(N) = \frac{Q_{\mathrm{tot}}^2}{2C} + \sum_{n=1}^{N} E_n = \frac{1}{2C}[-|e|(N - N_0) + \sum_i C_i V_i]^2 + \sum_{n=1}^{N} E_n \quad (2.1)$$

where N_0 is the dot occupancy for all $V_i = 0$ with $i \in S, D, G$ [33, 85]. The first term in Eq. 2.1 refers to the electrostatic energy of the QD, where the number of electrons N in the dot varies in discrete steps, while the gate-induced charges $C_i V_i$ changes the QD potential continuously (gating). The second term describes the sum over all the occupied quantum mechanical energy levels E_n.

It is clearly seen from Eq. 2.1 that the energy required to add the Nth electron to the QD is given by the difference between two single particle energy levels defined as the electrochemical potential $\mu(N)$ of the QD, i.e.

$$\mu(N) = E_{\mathrm{tot}}(N) - E_{\mathrm{tot}}(N-1) = E_{\mathrm{N}} + \frac{e^2}{C}[N - N_0 - \frac{1}{2}] - \frac{|e|}{C} C_{\mathrm{G}} V_{\mathrm{G}} \quad (2.2)$$

This expression represents a “ladder" of electrochemical potential levels, as shown in Fig. 2.2b. The spacing between these levels is the addition energy given by:

$$E_{\mathrm{add}} = \mu(N+1) - \mu(N) = \frac{e^2}{C} + \delta E \quad (2.3)$$

where $E_{\mathrm{C}} = e^2/C$ is the charging energy and δE is the quantized energy level spacing of the QD [33, 85]. This ladder of electrochemical potential levels can be shifted linearly by $e\alpha_{\mathrm{G}}\Delta V_{\mathrm{G}}$ using a gate voltage V_{G}, where $\alpha_{\mathrm{G}} = C_{\mathrm{G}}/C$ is the gate lever arm or efficiency factor.

For the low temperature regime $kT \ll \delta E \ll E_{\mathrm{C}}$ and linear bias regime $V_{\mathrm{SD}} \sim 0$, the Fermi distribution of the lead electrons $f_{\mathrm{S/D}}(E) = \frac{1}{e^{(E-\mu_{\mathrm{S/D}})/kT}+1}$ can be approximated as a step function with a small thermal broadening $\approx kT$ around $\mu_{\mathrm{S/D}}$. If $\mu(N) < \mu_{\mathrm{S}} = \mu_{\mathrm{D}} < \mu(N+1)$ as shown in Fig. 2.3b, electron transport is blocked, i.e. the so-called Coulomb blockade (CB) situation, where the number of electrons in the QD is fixed. By tuning the gate voltage V_G, the electrochemical potential of the QD can be aligned with those of the source-drain contacts, i.e. $\mu(N) = \mu_{\mathrm{S}} = \mu_{\mathrm{D}}$, as shown in Fig. 2.3a. The QD is said to be on-resonance and an electron from the leads can sequentially tunnel through the QD: *single electron resonant tunneling*. If one now measures G as a function of gate voltage V_{G}, one obtains a series of positive step-like increase in G, i.e. the so-called Coulomb peaks or resonances [33] (Fig. 2.3c), when the QD is on resonance. However, the CB peaks are typically broadened by various effects, such as applied bias voltage, finite temperature of the lead reservoirs and the QD lifetime such that they acquire an intrinsic line shape, as discussed in the next section.

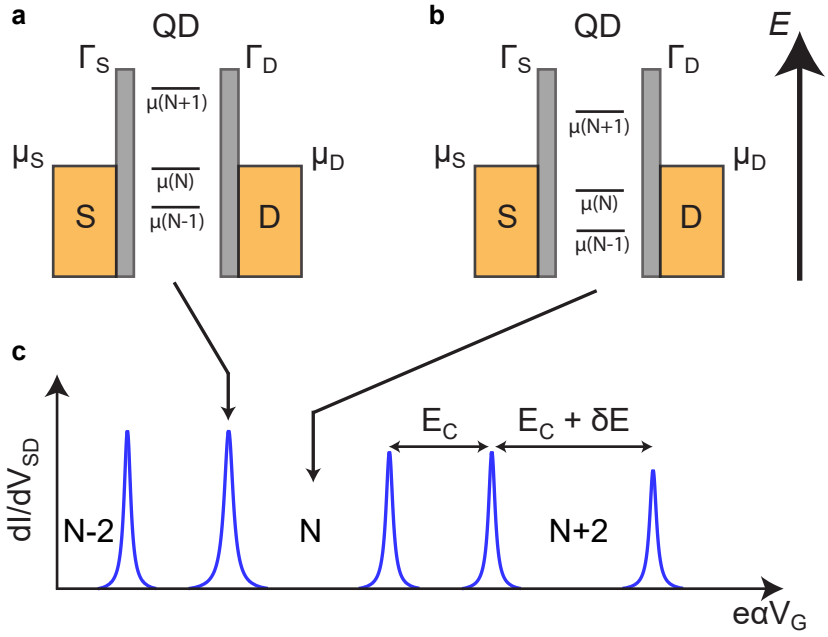

Figure 2.3. Coulomb Blockade in a single QD. a. Single QD energy level diagram describing the on-resonance configuration. An electron can tunnel through the single QD when the electrochemical potential μ of the QD aligns with the electrochemical potential of the source-drain contacts, i.e. $\mu_{\mathrm{N}} = \mu_{\mathrm{S,D}}$. **b.** Energy level diagram when the single QD is in Coulomb blockade. Electron tunneling through the QD is forbidden when $\mu_{\mathrm{N}} \neq \mu_{\mathrm{S,D}}$. **c.** Expected differential conductance $G = dI/dV_{\mathrm{SD}}$ as a function of V_{G} at $V_{\mathrm{SD}} = 0$ with two-fold degenerate energy levels. Schematics adapted from Refs [33, 69, 85, 86].

In addition, the CB resonances also directly reveal the two-fold spin degeneracy of QD energy level spectrum. This signifies that although each of the Coulomb peaks are separated by E_{add}, the first electron occupying a new orbital needs an energy $E_{\mathrm{add}} = E_{\mathrm{C}} + \delta E$, while for the second electrons $\delta E = 0$ leading to an addition energy of $E_{\mathrm{add}} = E_C$.

2.1.2. Resonance line shapes

Until now, the QD was assumed to be a perfectly isolated system such that the tunnel coupling $\Gamma_{\mathrm{S/D}}$ to the source-drain leads are always smaller than

any other relevant energy scales of the system. However, even a small coupling leads to a finite lifetime τ of the electrons on the QD. This provides an energy window of h/τ (Heisenberg's uncertainty principle) to tunnel slightly off resonance onto the QD - resulting in a finite resonance width even at $T = 0$. In the lifetime-broadened or strong coupling regime, i.e. $kT \ll \Gamma \ll \delta E, E_C$, the Coulomb peak can be expressed by a Breit-Wigner function [87]:

$$G(\Delta E) = \frac{e^2}{h} \frac{4\Gamma_S \Gamma_D}{\Gamma^2} \frac{(\Gamma/2)^2}{\Delta E^2 + (\Gamma/2)^2} \tag{2.4}$$

where $\Delta E = -e\alpha_G(V_G - V_G^{(0)})$ is the level detuning of the resonance at position $V_G^{(0)}$. The tunnel coupling $\Gamma = \Gamma_S + \Gamma_D$ is given by the full width at half maximum (FWHM), while the conductance maximum is determined by the tunnel barriers asymmetry.

On the other hand, in the thermally broadened or weak coupling regime, i.e. $\Gamma \ll kT \ll \delta E, E_C$, the lineshape is described by [88]:

$$G(\Delta E) = \frac{e^2}{h} \frac{\pi}{2k_B T} \frac{\Gamma_S \Gamma_D}{\Gamma_S + \Gamma_D} \cosh^{-2}\left(\frac{\Delta E}{2k_B T}\right) \tag{2.5}$$

In this regime, the FWHM is given by: $FWHM \approx 3.5 k_B T$, while the conductance amplitude depends on the asymmetry A and decays with temperature as $\sim 1/k_B T$.

2.1.3. Coulomb diamonds

In addition to V_G, Coulomb blockade can also be lifted by applying a large finite source-drain bias $V_{S/D}$, as shown in Fig. 2.4. Whenever an electrochemical potential level of the QD enters the bias window defined by: $-|e|V_{SD} = \mu_S - \mu_D$, electrons can tunnel through the QD. By measuring G as a function of V_{SD} and V_G, we observe a pattern of so-called Coulomb diamonds [85], as shown in Fig. 2.4. Inside the diamonds, the number of electrons on the QD is fixed and the system is in CB where no sequential tunneling allowed. However, outside of the diamonds, CB is lifted as there is at least one QD level within the bias window. The boundaries of the CB diamonds mark the onset of charge transport with the negative slope β_- signifying a QD level aligned with the drain μ_D (panel **I** in Fig. 2.4), while for the positive slope β_+ line $\mu_{QD} = \mu_S$ holds (panel **III** in Fig. 2.4).

Assuming asymmetric biasing, i.e. $\mu_D = 0$ and bias is applied at the S contact only, we have to tune the gate V_G for staying along the diamond edges in order to compensate for the electrochemical potential shift of the QD due to the capacitive coupling from the S contact. This allows us to calculate the slopes $\beta_{+/-}$: From $\mu_{QD} = 0 = \mu_D$ for the line with negative slope, one finds $0 = -|e|\frac{C_G}{C}\Delta V_G - |e|\frac{C_S}{C}\ \Delta V_{SD}$ resulting in $\beta_- = -\frac{C_G}{C_S}$. Similarly for the

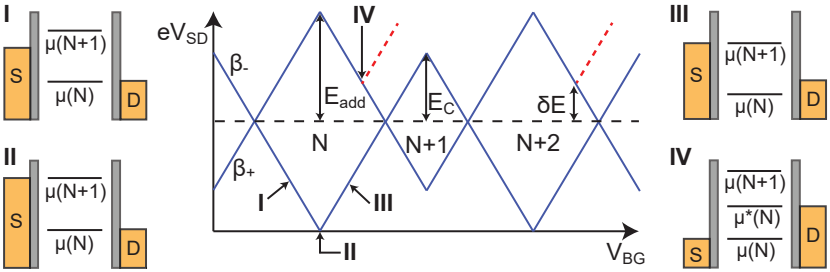

Figure 2.4. Schematics of Coulomb blockade diamonds in a single QD. Differential conductance G of a typical NW QD as a function of source-drain bias voltage V_{SD} and gate voltage V_{G}. The blue lines describe the edges of the Coulomb diamonds with slopes β_+ and β_-. A clear two-fold periodicity is shown, which can be used to extract E_{add}, E_{C} and δE. The energy diagram in panels **I-III** shows different biasing conditions as marked in the Coulomb diamond diagram. The energy diagram **IV** describes transport through the first orbital excited state. Schematics adapted from Refs [33, 69, 85, 86].

positive slope, one obtains $-|e|V_{\mathrm{SD}} = -|e|\frac{C_{\mathrm{G}}}{C}\Delta V_{\mathrm{G}} - |e|\frac{C_{\mathrm{S}}}{C}\ \Delta V_{\mathrm{SD}}$ giving us a positive slope of $\beta_+ = \frac{C_{\mathrm{G}}}{C-C_{\mathrm{S}}}$. We can then estimate various parameters, such as α, C_{S}, C_{D}, C_{G}, from the negative and positive slopes of the diamond edges such that the lever arm of the gate can be determined as $\alpha_{\mathrm{G}} = \frac{\beta_+|\beta_-|}{\beta_+ + |\beta_-|} = \frac{C_{\mathrm{G}}}{C}$. In addition, at the tip of the diamond where the negative and positive slopes cross as shown in panel **II** in Fig. 2.4, the corresponding QD levels are aligned with both μ_{S} and μ_{D} respectively. This allows us to measure the spacing between two adjacent levels of the QD, i.e. the addition energy $E_{\mathrm{add}} = E_{\mathrm{C}} + \delta E$ is given by the size of the big diamond in a two-fold degenerate energy spectrum, while the size of the small diamond corresponds to the charging energy E_{C}.

Excited states and cotunneling

In all the above discussion, we only considered the ground state transitions $E_{\mathrm{tot}}(N+1) \leftrightarrow E_{\mathrm{tot}}(N)$. However when we apply $|eV_{\mathrm{SD}}| > \delta E$, the Nth electron can be excited into the $E_{\mathrm{N+1}}$ orbital and relax back to the ground state. These *excited orbital state* appears as an additional line in G running parallel to the diamond edge and terminating at $|eV_{\mathrm{SD}}| < \delta E$ whenever an excited energy level μ^*(N) falls into the bias window (panel **IV** in Fig. 2.4).

Apart from the above, higher order tunneling processes such as *co-tunneling* are possible with increasing tunnel coupling Γ. In such a process, an electron

can leave the QD under CB, if another electron tunnels onto the QD within the Heisenberg's uncertainty times scale of $\sim \hbar/E_C$. This gives rise to a constant $G \propto V_{SD}$ inside the CB diamond region [89]. This process is defined as elastic co-tunneling or inelastic co-tunneling depending on whether the QD remains in the ground state or excited state, respectively, after the event.

2.1.4. Quantum dot states in magnetic field

As described earlier, the energy spectrum of a QD depicts a two-fold spin degeneracy such that the electrons occupy doubly degenerate levels. This spin degeneracy can be lifted by applying an external magnetic field B. The electron spins in the QD will align either parallel or anti-parallel to the external magnetic field. The energy of such parallel and anti-parallel spin configurations shift linearly in opposite directions such that the energy separation is given by: $\Delta E_{Z,N} = g_N^* \mu_B B$, where g_N^* is the effective g-factor of the nth quantum level and μ_B is the Bohr magneton. This is known as the Zeeman effect [90] from atomic physics.

In addition to the linear Zeeman splitting, the energy of a QD state with spin states $s_z = \pm 1/2$ shows a quadratic dependence on B given by:

$$\Delta E_{N,s_z} = s_z g_N^* \mu_B B + \gamma B^2 \tag{2.6}$$

The second term describes the effect of diamagnetic shift [87] with an experimentally determined proportionality constant γ that accounts for the diamagnetism of the QD when an induced magnetic moment couples with B.

In this formulation, the electron is considered a non-interacting particle such that all the interactions are accounted within the effective g-factor g^*. This reveals an effective g-factor of $g^*_{InAs} = -14.9$ for bulk InAs [65, 91], which is considerably different from the free electron value of $g_e = +2.0023$. This leads to a large separation in the energy of the spin states with relatively small B, leaving the contribution of the diamagnetic shift very small. However, the effective g-factor in a QD can significantly deviate from the bulk value depending on the electronic wave function in the confinement potential. It has been observed that g-factor reduces towards the free electron value of 2 in very small QDs where the effect of confinement becomes prominent - an effect called the quenching of orbital angular momentum [92, 93]. Furthermore in a distorted confinement potential, the orbital angular momentum becomes direction dependent making the g-factor anisotropic.

In our transport spectroscopy investigations, the Coulomb resonances will exhibit position shifts according to Eq. 2.6 while measuring the conductance G as a function of gate voltage and magnetic field B. If the Zeeman energy $\Delta E_Z(B)$ becomes as large as the level spacing $\delta E(B)$, a ground state transition takes place and the N electron state evolves according to the lower energy state

in the $E_N(B)$ spectrum. On the other hand, the Zeeman splitting becomes too obscured if the level spacing is too small.

2.1.5. Magneto-Coulomb effect

Quantum dots serve as extremely sensitive electrostatic sensors to their surroundings such that any small change in the electrochemical potential of a nearby ferromagnet can be detected. Such a ferromagnet in close proximity to the dot induces an effective gating action on the QD upon application of an external magnetic field. This effect is referred to as Magneto-Coulomb effect [94], and has been observed in QD-based spin valves [94–96].

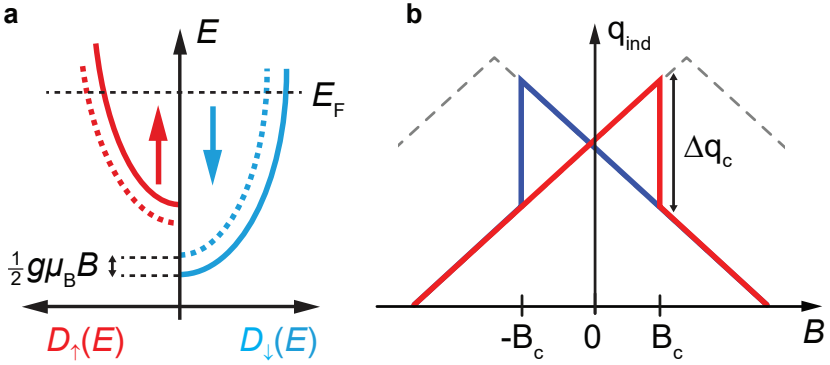

Figure 2.5. The Magneto-Coulomb effect a. Schematics of the spin-split subbands in a typical ferromagnet. An external magnetic field B shifts the two subbands energies in opposite directions by $|\frac{1}{2}g\mu_B B|$, as shown by the dashed lines. **b.** Illustration showing the characteristic sawtooth-like dependence of the induced charge q_{ind} on the QD as a function of B. A sudden change in the induced charge Δq_c is observed when B is swept through the coercive field B_C of the ferromagnet. Schematics adapted from Refs. [96]

For a normal metal, an external magnetic field linearly shifts the electron energies of the two spin species in opposite directions by the Zeeman term $\pm\frac{1}{2}g\mu_B B$. However in the case of a ferromagnet, the electron filling of the two spin subbands as well as the corresponding spin-dependent density of states $D_{\uparrow/\downarrow}(E_F)$ are different, as shown in Fig. 2.5a. Therefore, to preserve the number of electrons, the electrochemical potential of the ferromagnet gets shifted by:

$$\Delta\mu = -\frac{1}{2}Pg_{FM}\mu_B B \tag{2.7}$$

where g_{FM} is the g-factor of the ferromagnet, μ_B is the Bohr magneton and $P = \frac{D_\uparrow(E_F) - D_\downarrow(E_F)}{D_\uparrow(E_F) + D_\downarrow(E_F)}$ is the spin polarization of the ferromagnet. In practice, the ferromagnet is connected to a nonmagnetic lead, i.e. a charge reservoir, that requires the electrochemical potential in both metals to be equal. This shift translates to a change in contact potential $\Delta\phi$ between the ferromagnet and the lead. This potential change induces an additional charge in the QD given by:

$$\Delta q_{\mathrm{ind}}(B) = \frac{C_{FM}}{2e} P g_{FM} \mu_B B \tag{2.8}$$

where C_{FM} is the capacitance of the ferromagnet to the QD. Thus, applying an external magnetic field to a close-by ferromagnet effectively acts as gate voltage to the QD. From Eq. 2.8, we can clearly see that the induced charge and hence the conductance G linearly shifts with B in the absence of any ferromagnetic switching.

Let us now consider the case where magnetization switching of the ferromagnet is allowed. Sweeping the external field B from $B > 0$ towards $B < 0$, the magnetization of the ferromagnet reverses on reaching the coercive field $B = -B_c$. This leads to a sudden jump in the conductance G as the induced charge changes discontinuously at B_C by:

$$\Delta q_c = \frac{C_{FM}}{e} P g_{FM} \mu_B B_C \tag{2.9}$$

A characteristic sawtooth-like profile in the induced charge (and hence the conductance G) is observed, as shown in Fig. 2.5b. In addition, the position of the QD resonances are also shifted in a similar manner in the energy spectrum of the dot.

2.1.6. Double quantum dots

We will now extend our discussions from single quantum dot systems to double quantum dots (DQDs) - an integral component of spin filter and spin valve devices in this thesis. Two QDs can be formed in series by introducing a third tunnel barrier in the NW such that two different regions become energetically confined. Such a structure is called serial double quantum dot [97] (*or artificial molecules*) such that an additional tunneling event takes place between the two QDs determined by spin selection rules.

An electrostatic model/circuit diagram for a serial DQD is shown in Fig. 2.6a. The two QDs are capacitively as well as tunnel coupled to their respective source-drain leads, along with a mutual capacitance C_M and tunnel coupling Γ_M between the dots. Two gate electrodes V_{G1} and V_{G2} tune the electrochemical potential of individual dots QD1 and QD2 respectively. Typically, it is difficult to avoid capacitive cross-talk in such small systems. Therefore, the two

gates tune both QD1 and QD2 to different extents via the cross-capacitances V_{G1x} and V_{G2x}. An electrochemical potential diagram of the DQD is shown in Fig. 2.6b where $\mu_{1,2}(N, M)$ depicts the electrochemical potential and (N, M) describes the electron population/configuration in QD1 and QD2 respectively. We now limit our discussion to the linear bias regime, where V_{SD} is extremely small, i.e. $V_{SD} \to 0$ and $\mu_{S,D} = 0$.

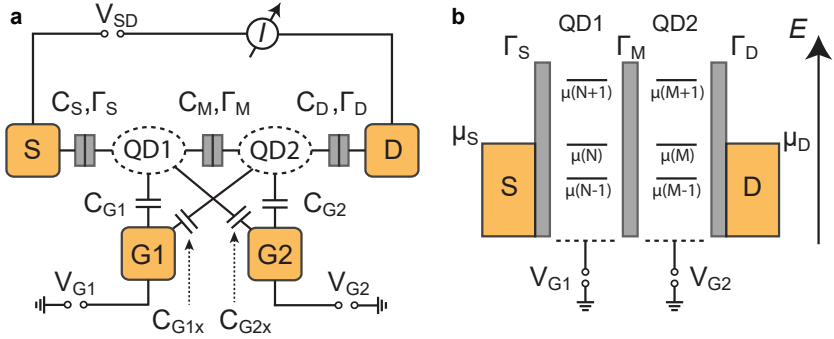

Figure 2.6. Model of a double quantum dot (DQD) in series a. Capacitance model and typical measurement schematics of a DQD. The two quantum dots QD1 (QD2) are capacitively coupled to the source(drain) reservoirs, denoted by S(D), with capacitive coupling C_S (C_D) and tunnel coupling strength Γ_S (Γ_D). Each of the dot QD1 (QD2) can be tuned by the gate G1 (G2) with capacitance C_{G1} (C_{G2}) and cross-capacitance C_{G2x} (C_{G1x}). The two dots are also coupled through a mutual capacitance C_M and inter-dot tunnel coupling strength Γ_M. **b.** Illustration of the energy level diagram of a DQD showing the electrochemical potential energies μ of the two dots relative to those of the S-D contacts, $\mu_{S,D}$. The electron population in the DQD is denoted by (N,M) where N (M) denotes the number of electrons in QD1 (QD2) respectively. Schematics adapted from Refs. [97]

2.1.6.1. Charge stability diagram

In the linear regime, the charge configuration (N, M) of a DQD system can be determined by the so called *charge stability diagram* [97], i.e. conductance G as a function of gate voltages V_{G1} and V_{G2}. The shape of the charge stability diagram is mostly governed by the mutual capacitance C_M between the two dots. Fig. 2.7 shows the stability diagram for a DQD system with (a) weak ($C_M \to 0$), (b) intermediate ($0 < C_M < C_{1,2}$), and (d) large ($C_M/C_{1,2} \to 1$) interdot coupling, where $C_{1(2)} = C_{S(D)} + C_{G1(G2)} + C_M$ is the total capacitance of QD1 and QD2 respectively.

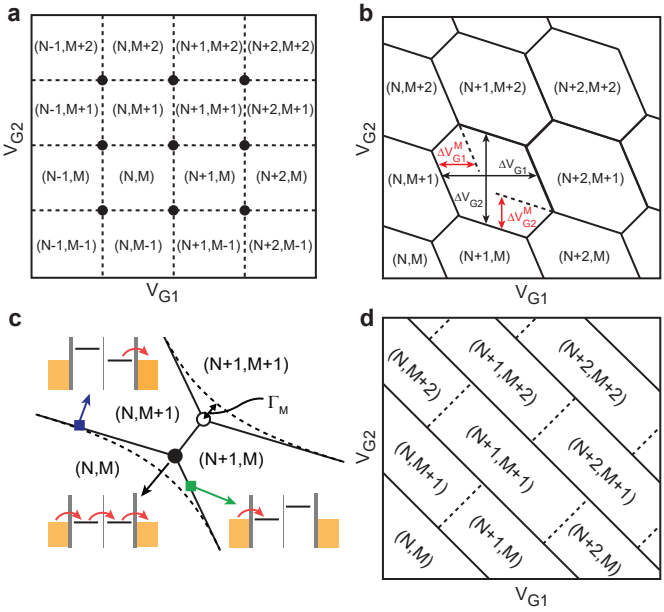

Figure 2.7. Schematics of charge stability diagram of a DQD in series a. Charge stability diagram for the DQD with **a.** small ($C_M \approx 0$) and **b.** intermediate ($0 < C_M < C_{1(2)}$) inter-dot tunnel coupling. The stability diagram evolves into a honeycomb pattern for intermediate inter-dot tunnel coupling strengths, where the degeneracy points (black dots) in **a** splits into so-called triple points due to electrostatic interactions. The dimensions of the honeycomb pattern are used to determine the respective gate and mutual capacitances as given in Eq. 2.10 and Eq. 2.11. **c.** Evolution of the degenerate triple points into avoided crossings (dashed black lines) with increasing inter-dot tunnel coupling strength Γ_N. The insets describe the charge transfer process through the DQD for the relevant edges of the honeycomb pattern. **d.** For large C_M, the DQD effectively behaves as a single QD and the honeycomb pattern evolves into parallel lines. Schematics adapted from Refs. [97]

In the weak interdot coupling regime, the two individual QDs are fully decoupled (neglecting cross capacitances) and electron transport is independent of the other QD, i.e. $V_{G1,G2}$ tunes $QD_{1,2}$ independently. The charge stability diagram reveals a rectangular pattern of perfectly horizontal and vertical lines as shown in Fig. 2.7a. Each line represents a change in the electron number of the corresponding QD by one. For a small bias, electron transport through

the DQD is possible only at the crossing points, where the electrochemical potential of the two individual dots align with source-drain electrochemical potentials, i.e. $\mu_S = \mu_1 = \mu_2 = \mu_D$.

However in a realistic picture, there is always a finite mutual capacitance C_M between the two dots as well as a finite cross capacitance from the two gate electrodes. The rectangular charge stability diagram then evolves to a regular honeycomb pattern with two different slopes that forms the edges of the honeycomb hexagon, as shown in Fig. 2.7b. The number of charge carriers is fixed inside each of the honeycomb hexagon. However, each crossing point splits into *two triple points* where three different charge states (N, M),$(N + 1, M)$ and $(N, M+1)$ are energetically degenerate. Therefore, electrons tunnel through the DQD in two possible charge transfer processes: (1) $(N, M) \rightarrow (N+1, M) \rightarrow (N, M+1) \rightarrow (N, M)$, and (2) $(N+1, M+1) \rightarrow (N+1, M) \rightarrow (N, M+1) \rightarrow (N+1, M+1)$. The former process can be interpreted as an electron sequentially tunneling from the source to drain, while the latter is the sequential tunneling of a hole in the opposite direction. The spacing between the honeycomb edges determines the gate capacitances by:

$$C_{Gi} = \frac{e}{\Delta V_{Gi}} \tag{2.10}$$

where $i \in 1, 2$ refers to QD1, QD2 respectively and ΔV_{Gi} is the corresponding spacing. In addition, the distance between each set of triple points is related to the mutual capacitance C_M by:

$$C_M = C_{1/2} \frac{\Delta V^M_{G1/G2}}{\Delta V_{G1/G2}} \tag{2.11}$$

where $C_{1/2}$ is the total capacitance of QD1/QD2 determined from the non-linear, i.e. finite bias, regime discussed in the next section.

If we now take into account a finite tunnel coupling Γ_M between the two dots, the degeneracy at the triple points is lifted leading to avoided crossings in the charge stability diagram, as shown in Fig. 2.7c. At the triple points, the two QD states hybridize to form bonding and anti-bonding molecular orbitals, rounding off the hexagonal lines into avoided crossing features. The separation of the avoided crossing from the triple points is determined by the strength of the interdot tunnel coupling. If the tunnel coupling Γ_M and the mutual capacitance $(C_M/C_{1,2} \rightarrow 1)$ is very large, the resulting charge stability diagram evolves into parallel lines signifying an effectively large single QD as shown in Fig. 2.7d.

2.1.6.2. Bias triangles

We now consider the case of an asymmetric finite bias $|V_{SD}| > 0$ applied to the DQD such that $\mu_D = 0$ and the bias is applied to the source contact, similar to

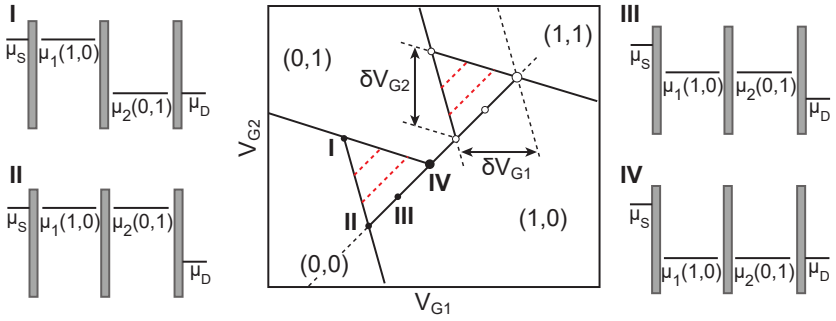

Figure 2.8. Transport through a serial DQD at finite bias voltage V_{SD}. For finite V_{SD}, the triple points in the honeycomb pattern change into bias triangles, where electron transport through the DQD is allowed in the regions within these bias triangles. The insets (**I-IV**) describe the electrochemical energy level diagrams for the relevant points along the bias triangle boundaries. For large V_{SD}, multiple discrete energy levels enter the bias window resulting in electron transport through excited states (red dashed lines).

the single QD description. The conductance regions at the triple points of the honeycomb change into triangular shaped regions, so-called *bias triangles* [97], at finite bias as shown in Fig. 2.8. The boundaries of these bias triangles are determined by the condition: $-|e|V_{SD} = \mu_S \geq \mu_1$, $\mu_1 \geq \mu_2$ and $\mu_2 \geq \mu_D = 0$. An electron is allowed to tunnel through the DQD within these bias triangles, while outside the triangles electron transport is blocked. The dimensions of the triangles δV_{G1} and δV_{G2} are related to the applied bias voltage V_{SD} by:

$$\alpha_{1(2)}\delta V_{G1(G2)} = \frac{C_{G1(G2)}}{C_{1(2)}}|e|\delta V_{G1(G2)} = |eV_{SD}| \tag{2.12}$$

where $\alpha_{1,2}$ are the corresponding gate lever arms. Using Eq. 2.10, 2.11 and 2.12, we can explicitly determine the total capacitances $C_{1,2}$ and mutual capacitance C_m.

All the above discussion was based on the assumption that a single energy level from each QD lies within the bias window. However for sufficiently large bias voltages, multiple discrete energy levels enter the bias window. In such a case, the excited states also contribute to the conductance along with the ground state. Such an excited state transition appears as a resonance parallel to the ground state resonance within the bias triangle, as illustrated by the red dashed lines in Fig. 2.8.

2.1.7. Pauli Spin Blockade

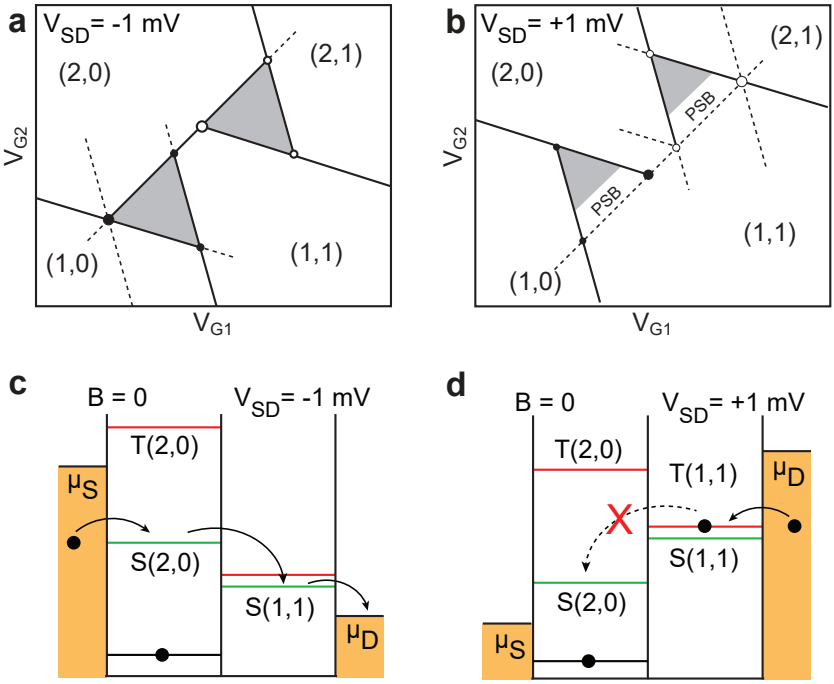

Figure 2.9. Pauli Spin Blockade. a,b Schematics of DQD charge stability diagram at **(a)** negative $V_{SD} = -1\,\text{mV}$ and **(b)** positive $V_{SD} = +1\,\text{mV}$ bias voltages. **c,d** Energy level diagram at $B = 0$ for the DQD charge transition $(1,1) \rightarrow (2,0)$ at **(c)** negative $V_{SD} = -1\,\text{mV}$ and **(d)** positive $V_{SD} = +1\,\text{mV}$ bias voltages. Electron transport is blocked when the T(1,1) state gets occupied in Fig. **d**, resulting in a current suppression at the base of the bias triangles as shown in Fig. **b**. Figure adapted from Ref. [87].

In a typical DQD system, the electron spin is conserved during tunneling events. The tunneling current is strongly suppressed when the initial and final spin states of the DQD system are orthogonal, thereby forbidding the electron transition. This phenomenon is known as *Pauli spin blockade* (PSB) [87] and has been observed in single QDs with strong electron-electron interactions [98] as well as DQD systems [99]. For a DQD in series with up to two electrons in each dot, PSB is observed at finite V_{SD}. We consider the charge transition with two electrons in the DQD as shown by the bias triangle in Fig. 2.9a, where

the left QD contains one electron. The ground state (GS) of the (2,0) charge configuration is the spin singlet (S) state $[|S\rangle = \frac{1}{2}(|\uparrow\downarrow\rangle - |\downarrow\uparrow\rangle)]$, while the (2,0) spin triplet (T) excited state (ES) are inaccessibly higher up in energy. On the other, the singlet and triplet states for the charge configuration (1,1) are almost degenerate due to negligible exchange interaction between the two electrons residing in different QDs. For a negative V_{SD}, the charge transfer cycle is $(1,0) \rightarrow (2,0) \rightarrow (1,1) \rightarrow (1,0)$. The interdot charge transition occurs through the $S(2,0) \rightarrow S(1,1)$ spin states, which conserves the spin of the tunneling electron and current flows unhindered, as shown by the energy level diagram in Fig. 2.9c. For the opposite polarity positive V_{SD}, the charge transfer cycle is $(1,0) \rightarrow (1,1) \rightarrow (2,0) \rightarrow (1,0)$. Since the S(1,1) and T(1,1) spin states are almost degenerate, an electron can enter the right QD to form either the S(1,1) or the T(1,1) state. For the S(1,1) state, the electron can tunnel through the DQD via the interdot transition $S(1,1) \rightarrow S(2,0)$. However when an electron enters the T(1,1) state, it gets trapped as the T(2,0) spin state is inaccessibly high in energy. The interdot transition $T(1,1) \rightarrow S(2,0)$ is forbidden due to violation of spin conservation (Fig. 2.9d) and the finite V_{SD} disallows tunneling back to the metal reservoirs. The trapped electron then prohibits further occupation of the right QD due to Coulomb blockade effect. This PSB phenomenon results in a suppression of the current in the bias triangle at positive V_{SD}, as depicted in Fig. 2.9b. PSB within the bias triangles can be lifted by spin-flip processes, mediated by spin-orbit interaction or hyperfine interaction.

2.2. Ferromagnetism

In general terms, ferromagnetism can be described as a physical phenomenon in which certain materials, such as iron (Fe), cobalt (Co) and nickel (Ni), are attracted to a magnetic field and form permanent magnets. Quantum mechanically, ferromagnetism is a quantum mechanical effect in which the magnetic moment of the electrons gets collectively ordered to produce a finite magnetization $\mathbf{M}$ in a permanent magnet. Such finite $\mathbf{M}$ occurs on macroscopic length scales and even at room temperatures if the Curie temperature T_{Cu}, i.e. the temperature above which ferromagnetic ordering gets destroyed, is sufficiently large as in Fe, Co and Ni.

For a ferromagnetic material, the magnetic moments retain their ordered alignment even in the absence of an external magnetic field B. This results in a non-zero magnetization at $B = 0$, which is known as the remanent magnetization M_r as shown in Fig. 2.10a. The magnetization gets reversed only when a sufficiently large B is applied in the opposite direction to overcome the ferromagnetic order. This field is termed as the coercive field $B_{\mathrm{C}} = \mu_0 H_{\mathrm{c}}$ as illustrated in Fig. 2.10a. Further increase to higher B aligns all the magnetic

moments along the direction of B and the ferromagnetic material reaches its saturation magnetization M_S. Therefore, the magnetization of a ferromagnet strongly depends on the B sweep history, resulting in a loop for the magnetization curve as a function of applied magnetic field B. This phenomena, known as *magnetic hysteresis*, is shown in Fig. 2.10a. The width of the hysteresis loop determines the coercivity of a material, i.e. the ability of the material to withstand external magnetic fields without losing its magnetization. Ferromagnets with small and large coercive fields H_C are categorized as soft and hard magnets, respectively.

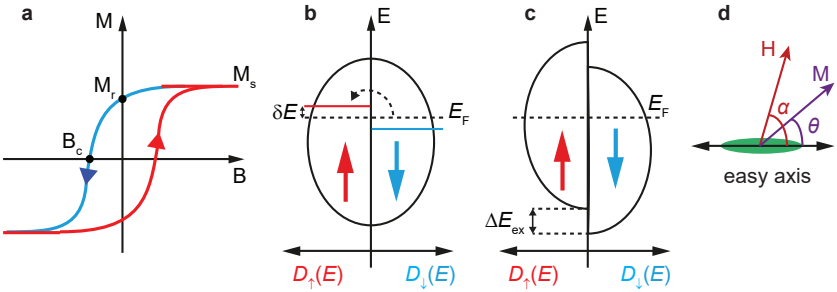

Figure 2.10. Basic characteristics of ferromagnetism. a. Magnetization curve M as a function of external magnetic field B for a ferromagnet with saturation magnetization M_S, remanent magnetization M_r and coercive field B_c. **b.** Schematic of the density of states (DOS) for the spin-up ($D^{\uparrow}(E)$) and spin-down ($D^{\downarrow}(E)$) electrons, where the dashed arrow describes spin-flip processes. **c.** Schematics of the spin-split bands shifted by the exchange splitting ΔE_{ex} in the Stoner model. A spontaneous magnetization $M \propto (n_{\uparrow} - n_{\downarrow})$ proportional to the difference between the number of spin-up and spin-down electrons arises. **d.** Schematics of an elliptical single-domain nanomagnet describing the angles between the easy axis, magnetization **M** and magnetic field **H** in the Stoner-Wolfarth model. Schematics adapted from Refs [67, 70].

2.2.1. Microscopic origin

In a classical description, the magnetic dipole moments energetically favor an anti-parallel orientation. However, ferromagnetic ordering favors parallel alignment of the electron's magnetic moments. In microscopic terms, such an ordering is the consequence of a purely quantum mechanical effect, known as *exchange interaction*, caused due to the Coulomb repulsion and indistinguishability of electrons [100, 101]. The fermionic statistics theorem states that the electron wavefunction has to be anti-symmetric under the exchange

of two particles, i.e. the amplitude for two identical electrons to occupy the same state is zero (Pauli exclusion principle). Therefore, the spatial distribution of the electron wavefunction depends on its spin configuration. In a ferromagnetic material, the reduced Coulomb repulsion energetically favors a parallel electron spin alignment if the thermal fluctuations do not dominate the exchange interaction.

Although the above exchange-interaction picture explains the origin of ferromagnetism in strongly localized systems, it fails to describe metallic ferromagnets, e.g. Fe, Co and Ni, in which the electrons responsible for ferromagnetism are itinerant [101]. Such systems are treated with the *Stoner model*, which assumes a spin-split band structure for the spin-up and spin-down electrons. The model evaluates the total energy change due to spontaneous magnetization in a ferromagnet [100, 101]. Such spontaneous magnetization arises when electrons are transferred from one spin band to other, creating an imbalance of the two spin species, as shown in Fig. 2.10b. This results in an increase in the total kinetic energy and a decrease in potential energy due to exchange interaction. The spontaneous ferromagnetic behavior occurs only when the system's energy reduction outweighs the kinetic energy increase, i.e. $E_{\text{tot}} < 0$, yielding the Stoner criteria

$$UD(E_{\text{F}}) \geq 1 \tag{2.13}$$

where U is the exchange interaction strength and $D(E_{\text{F}})$ is the density of states (DOS) at Fermi energy E_{F}.

To fulfill this criteria, we need a large exchange interaction strength and a large DOS at the Fermi energy. For the ferromagnetic metals Fe, Co and Ni, the Fermi energy lies within the narrow $3d$ bands leading to a large DOS $D(E_{\text{F}})$ [100]. The spin-split bands in these metals shift with respect to each other in order to maintain equal chemical potential at thermal equilibrium. This leads to the exchange splitting ΔE_{ex} between the spin-up and spin-down bands (Fig. 2.10c) and a spontaneous magnetization, $M \propto (n_{\uparrow} - n_{\downarrow})$ proportional to the difference between the number of spin-up and spin-down electrons, arises even without any external magnetic field.

2.2.2. Stoner-Wohlfahrt model

The Stoner model successfully describes the microscopic origin of ferromagnetism by considering the magnetization M homogeneous over the whole material. However, it fails to account for the local variations in $\mathbf{M}(\mathbf{r})$ and the various anisotropies observed in real bulk ferromagnets. This can be accounted for by minimizing the total free energy of a ferromagnet, i.e. $G = \int_V dV\, g_{\text{tot}}(\mathbf{M}(\mathbf{r}), \mathbf{H})$, which includes all the relevant energy terms and built-in magnetic anisotropies of the system [101, 102]. In summary, these anisotropies

align the magnetization $\mathbf{M}$ along a preferred orientation called the *easy axis*, for which the total free energy G of the system is minimal. The orientation with maximal energy is called the *hard axis*.

In this thesis, we provide a brief overview of the most relevant energy terms and magnetic anisotropies which contribute to the total energy density [101, 102] $g_{\text{tot}} = f_{\text{Z}} + f_{\text{ex}} + f_{\text{mc}} + f_{\text{d}}$ and determine the magnetic properties. The coupling between a ferromagnet and an external magnetic field B is given by: $f_{\text{Z}} = -\mathbf{BM} = -\mu_0\mathbf{HM}$, which gets minimized for parallel alignment of M with the external field. A short range exchange energy interaction term $f_{\text{ex}} \propto \nabla(\mathbf{M}(\mathbf{r}))^2$ explains the microscopic ferromagnetic ordering of magnetic moments, in which spins at adjacent sites prefer parallel alignment. The *magneto-crystalline anisotropy* f_{mc} term describes the favored alignment of magnetic moments along a crystallographic easy axis, determined by crystal field effects and spin-orbit interaction which couples the electron spins to the anisotropic orbitals in the crystal structure. It is described by the leading term in the expansion for uniaxial anisotropy: $f_{\text{mc}} = K\sin^2\theta + \mathcal{O}(\sin^4\theta)$, where θ is the angle between magnetization and the easy axis.

An important energy term is the dipolar energy density: $f_{\text{d}} = -\mu_0\mathbf{H}_d(\mathbf{r})\mathbf{M}(\mathbf{r})$, which describes the interaction of the magnetization with the dipolar field generated by the sample itself. The dipolar field generated by a ferromagnet is known as *demagnetizing field* (inside the sample) and *stray field* (outside the sample). Due to the non local nature of $\mathbf{B}_d$, this term determines the non-uniform magnetization configurations in samples with finite dimensions. The minimization of the stray field energies tends to reduce the surface magnetic charges of the magnet, i.e. align the magnetization parallel to the body edges. This effect, also known as *shape anisotropy*, leads to a preferred-in plane magnetization direction for soft magnetic materials such as Permalloy. We can engineer the magnetization direction by choosing an appropriate geometry, for example, an elongated strip tends to align its magnetization along the long axis. However for larger ferromagnetic samples, the stray fields can be reduced by *magnetic domains* - uniformly magnetized areas with parallel orientation of magnetic moments - separated from each other by *domain walls* over which the magnetic moments orientation continuously changes.

For the ferromagnets used in this thesis, the sample sizes are typically small (< 300 nm in width). In such samples, the energy cost to form domain walls is large compared to the reduction of dipolar energy. As a result, the exchange and anisotropy terms dominate leading to a single domain magnetization. Such single domain structures are well described by the *Stoner Wolfarth model* [103, 104] which considers only two energy terms: an ellipsoidal magnet of uniaxial anisotropy and constant magnetization $|\mathbf{M}|$ arising from magneto-crystalline or shape anisotropy, and the Zeeman energy of the magnet in an external magnetic field B. The expression is given by:

$$g_{\mathrm{sw}}(B) = f_{\mathrm{mc}} + f_{\mathrm{z}} = K \sin^2\theta - \mu_0 M_{\mathrm{S}H} \cos(\alpha - \theta) \tag{2.14}$$

where $\theta(\alpha)$ denotes the angle between easy axis and $\mathbf{M}(\mathbf{H})$ as shown in Fig. 2.10d. By minimizing the energy density in Eq. 2.14 with respect to θ, we can obtain the preferred orientations for magnetization $\mathbf{M}$, which is restricted to the plane containing $\mathbf{H}$ and the easy axis. For low $\mathbf{B} = \mu_0\mathbf{H}$, one gets two solutions as the minimal energy orientations for $\mathbf{M}$. As B is swept further, $\mathbf{M}$ displays either a smooth in-plane rotation or sudden sharp switching as only one of the solution becomes sustainable. For example, if B is applied parallel to the easy axis, i.e. $\alpha = 0$, the magnetization reverses abruptly at the switching or coercive field $H_{\mathrm{c}} = 2K/\mu_0 M_{\mathrm{S}}$ [103] forming a hysteresis loop. However for $\alpha = 90°$, we do not observe any hysteresis, but a continuous and smooth in-plane rotation of $\mathbf{M}$ towards the hard axis.

2.2.3. Spintronic devices and magnetoresistance effects

The field of spintronics refers to the control and manipulation of the electron's spin degree of freedom for various applications, such as information storage, logic and sensing [11, 13]. We briefly discuss the key concepts essential for such efficient spin control, for example spin injection, accumulation and detection. Furthermore, the relevant magnetoresistance effects observed in the spintronic devices - tunneling magnetoresistance (TMR) [105] and anisotropic magnetoresistance (AMR) [106]- are also discussed.

2.2.3.1. Spin polarization, injection and detection

The most important phenomena in the field of semiconducting spintronics in the generation of *spin polarized currents* [4]. The DOS $D_{\uparrow/\downarrow}(E_{\mathrm{F}})$ of the spin-up and spin-down electrons at the Fermi energy E_{F} of a ferromagnet is different due to the exchange-split spin bands. As a result, we can define the *spin polarization* of the ferromagnet by:

$$P = \frac{D_{\uparrow}(E_{\mathrm{F}}) - D_{\downarrow}(E_{\mathrm{F}})}{D_{\uparrow}(E_{\mathrm{F}}) + D_{\downarrow}(E_{\mathrm{F}})} \tag{2.15}$$

which can have absolute values from 0 (unpolarized, normal metals) to 1 (completely polarized) [107]. This spin polarization leads to a spin-polarized current in the ferromagnet. In the absence of any spin flip scattering, spin transport in a ferromagnet is by described the *two-current model* which assumes two independent spin channels j_σ, $\sigma \in \{\uparrow, \downarrow\}$ first proposed by Mott [108] and experimentally verified by Campbell and Fert [109]. The *current spin polarization* is then defined as the ratio of the difference between the two spin current $j_\uparrow - j_\downarrow$ to the total charge current $j_\uparrow + j_\downarrow$:

$$P_j = \frac{j_\uparrow - j_\downarrow}{j_\uparrow + j_\downarrow} \tag{2.16}$$

Typical current spin polarization for ferromagnetic metals such as Fe, Co, Ni are around $P_j \sim 0.4$ [110].

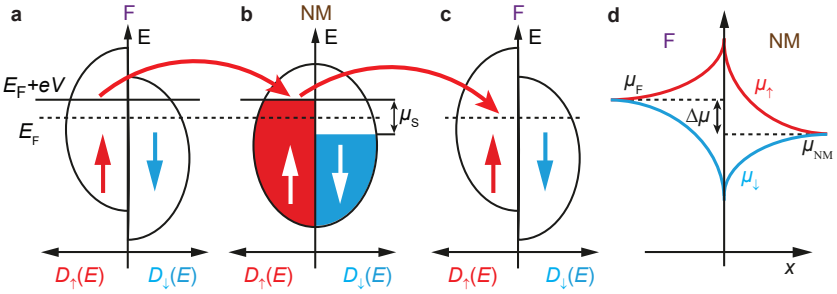

Figure 2.11. Spin Injection and spin accumulation in a non-magnetic material. a-c A spin polarized current is injected into a non-magnetic material (NM) from a ferromagnet F, resulting in a non-equilibrium spin accumulation $\mu_S = \mu_\uparrow - \mu_\downarrow$ in the NM near the F-NM interface. The spin polarized current can then be detected with a second ferromagnet. **d.** Schematics describing spin accumulation μ_S at the ferromagnet-non-magnetic material interface, where $\Delta\mu$ denotes the difference between the averaged electrochemical potentials μ_F and μ_{NM} across the interface. Adapted from Refs. [67, 70].

Therefore, ferromagnets can be fundamentally placed in contact with non-magnetic materials (NM), such as semiconductor (SC), superconductor (S) or normal metal (N) to inject a spin-polarized current across the interface. This process, known as *spin injection* [13], induces a non-equilibrium spin-band population in the non-magnetic material as illustrated in Fig. 2.11a,b. This induced difference in the electrochemical potential of spin-up and spin-down electrons is known as *spin accumulation* $\mu_S = \mu_\uparrow - \mu_\downarrow$ at the interface (Fig. 2.11b) [13]. Spin accumulation decays with increasing distance |x| from the interface into the NM due to spin-flip processes, resulting in a spin equilibrium $\mu_S = 0$ far away from the interface (Fig. 2.11d). For diffusive transport, the non-equilibrium spin accumulation μ_S decay is exponential, which can be obtained from the equation:

$$\frac{\delta^2 \mu_S}{\delta x^2} = \frac{\mu_S}{L_s^2} \tag{2.17}$$

where $L_s = \sqrt{\mathcal{D}\tau_s}$ is the characteristic length for spin flip processes or spin diffusion length, $\mathcal{D}$ is the spin-averaged diffusion constant and τ_s is the spin

relaxation time. The spin relaxation is mainly due to spin-orbit interaction, hyperfine interaction and magnetic impurities. The remaining spin-polarized current and spin accumulation can then be detected using a second ferromagnetic contact as shown in Fig. 2.11c, resulting in a typical *spin-valve structure* (F-NM-F) discussed in more details in section 2.2.3.2.

However, if the NM material in a typical spin valve device has large resistivity such as a semiconductor or graphene, spin injection is strongly suppressed due to *conductivity mismatch* at the interface [111]. This mismatch leads to lower values of current spin polarization in the ferromagnet as well as NM. The problem can be solved by using fully polarized ($P_N = 1$) half metallic ferromagnets or introducing a tunnel barrier between the ferromagnet-normal metal interface. The tunnel barrier provides a large interface resistance which shifts the decay of spin accumulation to the NM. In the case of InAs NWs, such tunnel barriers are typically created at the contact interfaces.

2.2.3.2. Magnetoresistance effects

As discussed in the previous section, ferromagnets serve as an useful tool to study spin transport phenomena. In mesoscopic devices, they are typically used as spin injectors and detectors to investigate magnetoresistance (MR) effects, i.e. change in resistance with magnetic field. We provide a brief description of the relevant MR effects for this thesis.

Tunneling Magnetoresistance

Spin valve structures have been extensively used for various applications, for example, as magnetoresistive random-access memory (MRAM) [23] and read/write heads of hard drives [22] for information storage. Typically, a spin valve consists of a non-magnetic (NM) material coupled/sandwiched between two ferromagnets (F), as shown in Fig. 2.12a [13]. The device resistance of such a structure can be controlled by the magnetization configuration of the ferromagnets. This is accomplished by placing two narrow F strips F_1 and F_2 with different width in contact with the NM such that they have different switching fields due to shape anisotropy. One can then obtain both parallel (P) and anti-parallel (AP) magnetization configuration by tuning the external magnetic field B. The P and AP configurations produce different conductances G_P/G_{AP}, resulting in a step-like conductance change at the switching field of the ferromagnets (Fig. 2.12b). This characteristic signal is defined as the *magnetoresistance* (MR) given by:

$$MR = \frac{G_P - G_{AP}}{G_P + G_{AP}} \tag{2.18}$$

Magnetoresistance can be classified into different categories based on its physical origin: If the NM material is conducting, the phenomenon is called

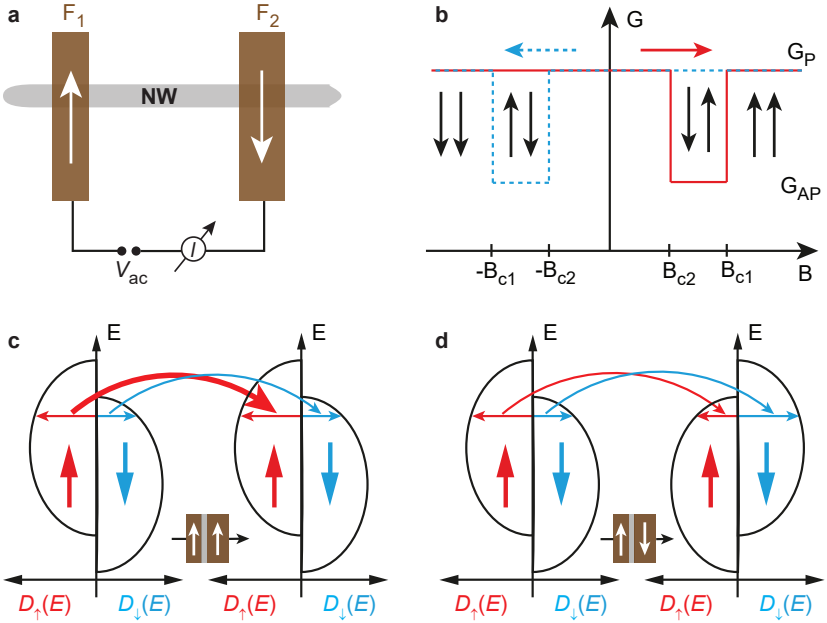

Figure 2.12. Tunneling Magnetoresistance (TMR) a. Schematics of a conventional spin-valve device consisting of two ferromagnets F_1,F_2 with different widths and a non-magnetic material (NM). **b.** Typical magnetoconductance (MC) curve for a spin-valve showing two different switching fields B_{c1} and $B_{c2}$for the two ferromagnets. The horizontal red and blue arrow denotes the up-sweep and down-sweep direction of the external magnetic field B, while the vertical arrows describe the magnetization configuration of the ferromagnets. **c,d** Schematics of the Jullière model for TMR. The conductance across the spin valve is determined by the DOS of two independent spin channels, such that higher conductance is observed for parallel magnetization configuration (**c**) than the anti-parallel magnetization configuration (**d**). Schematics adapted from Refs. [67, 70]

giant magnetoresistance (GMR). On the other hand, if the NM material is an insulator (I) forming a tunnel barrier F-I-F between the ferromagnets, the corresponding MR is called tunneling magnetoresistance (TMR). TMR can be well described by the Jullière model [112] which consists of two assumptions: (1) the electron spin is conserved during tunneling such that the two spin current channels are independent, and (2) the tunneling across the barrier is

energy independent resulting in a current given only by the product of the spin-dependent DOS $D_\sigma(E_\mathrm{F})$ at the Fermi energy. Hence, the conductance for P and AP magnetization states are given by:

$$G^{(ij)} = G_\uparrow^{(ij)} + G_\downarrow^{(ij)} \propto D_{1,\uparrow}^{(i)} D_{2,\uparrow}^{(j)} + D_{1,\downarrow}^{(i)} D_{2,\downarrow}^{(j)} \tag{2.19}$$

where $i, j \in \{+, -\}$ denotes the P and AP magnetization states. In the AP case, the majority (minority) spins have to tunnel into empty minority (majority) states resulting in a reduced conductance of the two spin channels as shown in Fig. 2.12d. However for the parallel magnetization case, the conductance is dominated by the majority spin current denoted by the larger arrow in Fig. 2.12c. Using the identity $D_\sigma^+(E_\mathrm{F}) = D_{-\sigma}^-(E_\mathrm{F})$ and Eq. 2.15, the TMR can be expressed as:

$$TMR = \frac{G_\mathrm{P} - G_\mathrm{AP}}{G_\mathrm{P} + G_\mathrm{AP}} = P_1 P_2 \tag{2.20}$$

where P_1 and P_2 are the spin polarization of the ferromagnets respectively. In Eq. 2.20, the TMR can have values between 0 (normal metal) and 1 (fully polarized ferromagnetic half-metals with $P_\mathrm{N} = 1$). Although, Jullière model provides a simple explanation for TMR, it neglects spin-flip processes during tunneling at the interface. It is also limited by the assumption that the tunneling matrix elements across the interface are energy independent, i.e. $T_\sigma(E) = T$.

Anisotropic Magnetoresistance

Anisotropic magnetoresistance (AMR) is defined as the change in the resistance of a ferromagnet based on the relative orientation of the magnetization **M** and current **j**. AMR arises due to spin-orbit interactions (SOI) and consequent anisotropic s-d spin-flip scattering processes. The conductivity of a ferromagnet is mostly determined by the unsplit 4s-band electrons due to their small effective mass. The main source of these s-electron scatterings are 4s-3d intraband transitions, where the resistivity (or scattering cross section) depends on the number of empty 3d states [113]. SOI allows spin-flip s-d scattering processes, which further increases the resistivity. Due to the built-in anisotropy of the d orbitals, the selection rules for such scattering processes depends on the relative orientation of the current and magnetization direction.

In general, only those s-electrons whose momentum direction **k** lies in the plane of d-orbitals can scatter into the empty 3d-states. If we now consider d-orbitals oriented in a plane perpendicular to **M**, we find that the scattering cross section, and hence the resistivity, is maximal for **j,k**||**M** and minimal for **j,k**⊥**M**. This dependence of the resistivity can be expressed as:

$$\rho(\phi) = \rho_\perp + (\rho_{||} - \rho_\perp) \cos^2 \phi \tag{2.21}$$

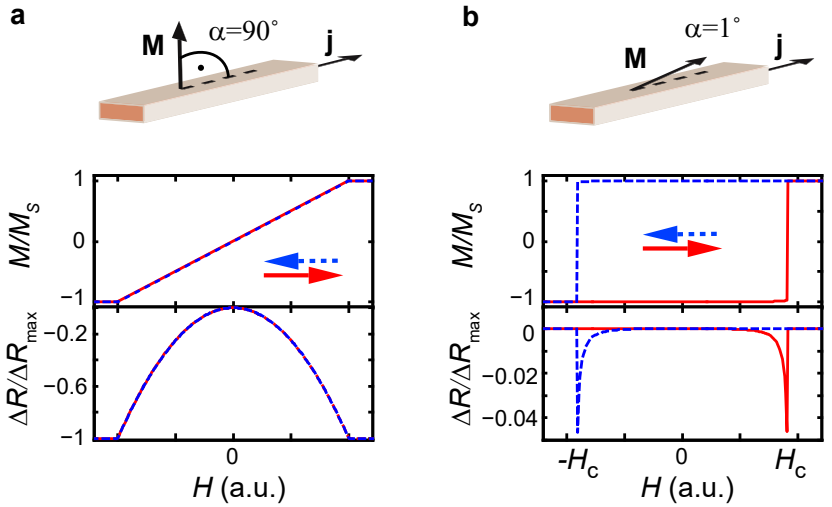

Figure 2.13. Anisotropic magnetoresistance (AMR) measurements. The normalized resistance change ($\Delta R/\Delta R_{\mathrm{max}}$) and the normalized magnetization M/M_{S} for a rectangular single-domain ferromagnetic strip as a function of external magnetic field H for angles (**a**) $\alpha = 90°$ and (**b**) $\alpha = 1°$ calculated from the Stoner-Wolfarth model. The red and blue arrows denote the up-sweep and down-sweep direction of H respectively. A continuous rotation of the magnetization M and a continuous decrease in the resistance is observed for $\alpha = 90°$, while M exhibits a sudden switching for $\alpha = 1°$ at the coercive field H_{c}. Adapted from Refs. [67, 70]

where ϕ is the angle between $\mathbf{j}$ and $\mathbf{M}$ and $\rho_{||}(\rho_{\perp})$ are the resistivities for $\mathbf{j}||\mathbf{M}$ ($\mathbf{j}\perp\mathbf{M}$). However, we note that a exactly accurate description of AMR requires a microscopic treatment of the scattering matrix elements and the spin-orbit interaction.

In practice, AMR measurements are used to determine the switching (coercive) field of single domain ferromagnets [106]. The magnetization $\mathbf{M}$ direction can be tuned with an external magnetic field B such that at higher B fields, $\mathbf{M}$ aligns in a parallel orientation with B. By applying a fixed current direction $\mathbf{j}$ along the easy axis of the ferromagnet, we can obtain the sample resistivity as a function of B by determining $\phi(B)$ from Eq. 2.14 of the Stoner-Wohlfahrt model. For $B \perp \mathbf{j}$, $\mathbf{M}$ continuously rotates towards the hard axis and the resistivity reduces parabolically to its saturation value $\rho_{\perp}$ as shown in Fig. 2.13a. For $B||\mathbf{j}$, the magnetization sharply switches its orientation at the coercive

field H_c. However, we do not observe as resistivity change in AMR as $\mathbf{j}||\mathbf{M}$ always. However, a small misalignment $\alpha = 1^\circ$ of B with $\mathbf{j}$ causes the magnetization to briefly rotate towards the hard axis before switching its orientation. This results in a characteristic resistance dip followed by a sudden jump at the switching fields as illustrated in Fig. 2.13b, allowing us to characterize the switching fields of single domain ferromagnetic strips as well as investigate multiple domain ferromagnetic configurations [114].

2.3. Superconductivity

Superconductivity is a physical phenomenon in which certain materials such as aluminum, mercury, lead or niobium show a vanishing electrical resistance when the temperature drops below a critical value T_c. Another key feature of superconductivity is the perfect diamagnetism in the superconducting state or the so-called Meissner-Ochsenfed effect [115], i.e. magnetic fields are expelled from inside the superconductor due to induced dissipation less surface currents. This leads to the existence of a critical magnetic field $B_c = \mu_0 H_c$, above which a thermodynamic phase transition to the normal state occurs due to the increased energy cost to keep the magnetic field out of the superconductor. In general, the external magnetic field leads to an increase of the Gibbs energy of the superconductor according to $dG_S = -VMdB$, where V is the volume of the superconductor, $M = -B/\mu_0$ is the magnetization of a perfect diamagnet and dB is the magnetic field change. This behavior of superconductors is frequently used to perform control experiments in the normal state. Although, superconductivity is phenomenologically described by the *Ginzburg-Landau* (GL) theory [116] and the *London equations*, the microscopic theory was presented by Bardeen, Cooper and Schrieffer in the BCS theory of superconductivity [51].

2.3.1. Cooper pairs and superconducting gap

The fundamental pillar of BCS theory is that in the presence of the 'Fermi sea', any net attraction between two electrons can bind them together into so-called *Cooper pairs* which obey bosonic statistics [51]. The binding energy of the electron pair is a function of the total momentum $\mathrm{K} = \mathrm{k_1} + \mathrm{k_1}$, where $\mathrm{k_1}$ and $\mathrm{k_2}$ are the wavevectors of the two electrons. The binding energy is maximum for $\mathrm{K} = 0$, i.e. the two electrons of a Cooper pair have opposite momenta, $\mathrm{k_1} = -\mathrm{k_2}$. This result can be intuitively understood by considering the physical origin of such attraction, which is mediated by the ion lattice. In a classical picture, an electron moving across a solid attracts the positively charged ion cores and deforms the ion lattice. This drags a cloud of positive polarization behind its path, which in turn attracts another electron. Quantum mechanically, this attraction is described as the exchange of virtual phonons.

Exchanging a virtual phonon with wavevector $\mathbf{q}$ results in the two new electron wavevectors $\mathrm{k}_{\mathbf{1}}^{'} = \mathrm{k}_{\mathbf{1}} + \mathrm{q}$ and $\mathrm{k}_{\mathbf{2}}^{'} = \mathrm{k}_{\mathbf{2}} - \mathrm{q}$, thereby conserving the total momentum $\mathrm{K} = \mathrm{k}_{\mathbf{1}} + \mathrm{k}_{\mathbf{2}} = \mathrm{k}_{\mathbf{1}}^{'} + \mathrm{k}_{\mathbf{2}}^{'}$. This exchange is limited by the available phonon energies, which is cut-off at the Debye frequency ω_{D}. The phonon mediated interactions are then limited to the narrow energy window of E_{F} to $E_{\mathrm{F}} + \hbar\omega_{\mathrm{D}}$, assuming all electron states below the Fermi energy are occupied. This corresponds to a narrow shell of thickness $\delta k = m\omega_{\mathrm{D}}/\hbar k_{\mathrm{F}}$ around the Fermi sphere in the reciprocal lattice, as illustrated in Fig. 2.14a. It can be clearly seen that the probability of phonon exchange is maximum for electrons with the condition $\mathrm{K} = 0$ as the whole δk shell is accessible (Fig. 2.14b), while if $\mathrm{K} \neq 0$ only the scattering states in the small area where both shells intersect are accessible.

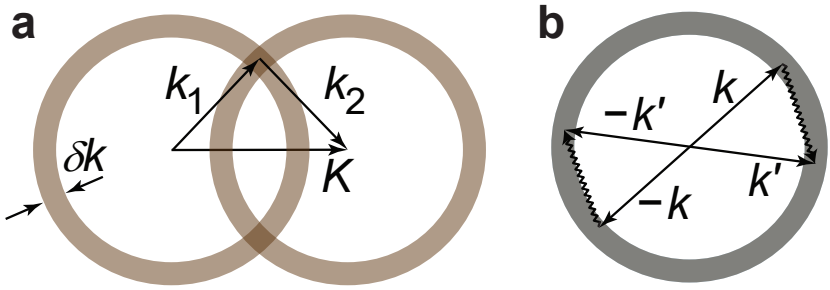

Figure 2.14. Schematics illustrating momentum conservation during the exchange of a virtual phonon. The blue circle denotes the allowed magnitude of the initial and final wavevectors of the electrons ranging between k_{F} and $k_{\mathrm{F}} + \delta k$. **a.** For $\mathbf{K} \neq 0$, only the small intersection area of the two circles fulfill momentum conservation. **b.** However for $\mathbf{K} = 0$, the two circles coincide, which maximizes the number of scattering events that fulfill momentum conservation and thereby maximizes the probability of phonon exchange. Schematics adapted from Refs. [67, 69]

In general for simple metals, the Cooper pair wavefunction comprises of two parts dependent on the spatial coordinates and the spin coordinates respectively. Since the two electrons have opposite momenta ($\mathbf{k}$,-$\mathbf{k}$), the orbital (spatial) wavefunction is the product of two plane waves given by:

$$\psi(\mathbf{r_1}, \mathbf{r_2}) = \sum_{k=k_{\mathrm{F}}}^{k_{\mathrm{F}}+\delta k} g_{\mathbf{k}} e^{\iota \mathbf{k}.\mathbf{r_1}} e^{-\iota \mathbf{k}.\mathbf{r_2}} = \sum_{k=k_{\mathrm{F}}}^{k_{\mathrm{F}}+\delta k} g_{\mathbf{k}} e^{\iota \mathbf{k}.(\mathbf{r_1}-\mathbf{r_2})} \tag{2.22}$$

In inversion-symmetric crystal, an interchange of two electrons should be indistinguishable from the original state such that the probability distribution

of the electrons remain unchanged. This means that the Cooper pair wavefunction can only pick up a phase factor during the interchange. However, a further second interchange must give back the original state, which limits the phase factor to either +1 or -1. Therefore, the orbital part of the Cooper pair wavefunction can either be symmetric or anti-symmetric. In contrast, the total Cooper pair wavefunction must be anti-symmetric under the interchange of two electrons due to the Pauli exclusion principle of fermions. Thus, the spin part of the wavefunction must have opposite symmetry to the orbital part. In metals such as aluminum, the orbital wavefunction is symmetric, which results in an anti-symmetric spin wavefunction known as the conventional 'spin singlet state': $|\mathrm{S}\rangle = \frac{1}{\sqrt{2}}(|\uparrow\downarrow\rangle - |\downarrow\uparrow\rangle)$. On the other hand, in liquid ^{3}He, the orbital wavefunction is anti-symmetric, which makes the spin wavefunction symmetric resulting in an unconventional 'spin triplet state'. For the aluminum superconductor used in this thesis, the Cooper pairs can thus be denoted by the notation $(k\uparrow, -k\downarrow)$. The spins of the two electrons are in a superposition state: the two individual spins of a Cooper pair are maximally entangled, while the total spin is zero.

The electrons keep condensing into Cooper pairs due to the attractive interactions until an equilibrium state has been reached where further pairing does not lower the energy anymore. This new ground state is known as the *BCS ground state*, which completely differs from the Fermi sea. Although a rigorous derivation of the BCS theory is omitted here, the most important findings of the BCS theory can be categorized into two effects: First, Cooper pairs obey bosonic statistics and can be described by a coherent macroscopic wavefunction. Second, the single particle energy spectrum in the superconducting state is gaped, i.e. excitations from the ground state requires a minimum energy of 2Δ, where Δ is the *superconducting energy gap*. The factor 2 is due to the breaking of one pair into two unpaired charge carriers. Since these coherent excitations are strongly different from free electron excitations in a Fermi gas, the new unpaired electrons are called *quasiparticles* or *Bogoliubons* in order to distinguish them. The dispersion relation of these quasiparticles can be written as:

$$E(\mathbf{k}) = \sqrt{\epsilon(\mathbf{k})^2 + \Delta^2} \tag{2.23}$$

where $\epsilon(\mathbf{k}) = \hbar^2 k^2/2m - E_\mathrm{F}$ is the kinetic energy of a free electron with respect to the Fermi energy. This dispersion relation has hole-like ($\epsilon < 0$) and electron-like ($\epsilon > 0$) branches, as depicted in Fig. 2.15a. The quasiparticles behave as free electrons (free holes) only for large kinetic energies $\epsilon \gg \Delta$ ($\epsilon \ll \Delta$), while at small kinetic energies the behavior is strongly deviated from free electrons due to the energy gap. Although the energy gap separates the Cooper pair condensate from the quasiparticle excitations, no states are lost in the phase transition from normal to superconducting state, i.e. $D_\mathrm{N}(\epsilon)d\epsilon =$

$D_S(E)dE$. One can then derive the density of states (DOS) $D_S(E)$ for the quasi-particle spectrum:

$$D_S(E) = D_N(\epsilon)\frac{d\epsilon}{dE} = \begin{cases} \frac{|E|}{\sqrt{E^2-\Delta^2}}, & |E| > \Delta \\ 0 & |E| < \Delta \end{cases} \tag{2.24}$$

where the normal state DOS $D_N(\epsilon)$ is assumed to be constant for energies close to the Fermi energy E_F, i.e. $D_N(\epsilon) \approx D_N(0)$. This normalized quasiparticle DOS is plotted in Fig. 2.15b where the normal state DOS is recovered for $|E| \gg \Delta$, the quasiparticle DOS diverges for $|E| \to \Delta$ and no quasiparticle states exist for $|E| < \Delta$ with the Cooper pair condensate located at E_F.

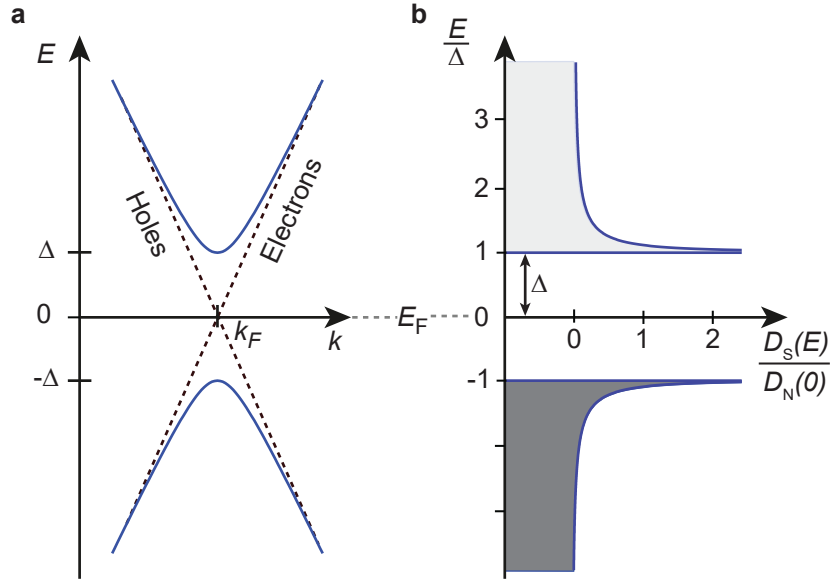

Figure 2.15. Dispersion Relation a. Quasiparticle dispersion relation in the superconducting state (solid blue lines) as compared to the normal state (dashed black lines) close to the Fermi energy E_F. **b.** Quasiparticle density-of-states (DOS) $D_S(E)/D_N(0)$ in the superconducting state for positive (electron-like excitations) and negative (hole-like excitations) energies in a band diagram formalism. Schematics adapted from Refs. [67, 69]

The vanishing electrical resistance below T_c and the perfect diamagnetism below B_c can now be explained by the gaped superconducting energy spectrum and BCS ground state. In a superconductor, the common motion of Cooper

pairs with a center of mass momentum $\mathbf{K}$ results in an electrical current. The scattering events which contribute to resistance are suppressed due to the gap Δ. This is because any change in the current carrying ground state due to inelastic scattering can occur only by breaking the Cooper pairs which requires a minimum energy cost of 2Δ. The Cooper pairs can be broken up and the superconductor driven to a normal state only when the energy associated with the supercurrent and the total center of mass momentum $\mathbf{K}$ of the Cooper pairs becomes 2Δ. The existence of such critical current results in a critical magnetic field B_c, where the induced supercurrents expelling the magnetic field from the superconductor reaches the described critical current value.

For finite temperatures $T > 0$, quasiparticles get thermally excited and occupy otherwise empty states. These states cannot be accessed by Cooper pairs anymore and hence, the superconducting order parameter or gap Δ decreases. The temperature evolution of the gap is approximated by:

$$\Delta(T) \approx \Delta(0)(1 - \frac{T}{T_c})^{1/2} \tag{2.25}$$

where $\Delta_0 = \Delta(T = 0) \approx 1.764\, kT_c$ is the gap at zero temperature for BCS superconductors with weak electron-phonon coupling. Another important quantity related to the superconducting gap is the BCS coherence length given by:

$$\xi_0 = \frac{\hbar v_F}{\pi \Delta} \tag{2.26}$$

Apart from the factor of π, Eq. 2.26 can be intuitively interpreted as the position uncertainty $\delta x \sim \hbar/\delta p \sim \hbar p_F/m\delta E \sim \hbar V_F/\Delta$ due to an energy uncertainty $\sim \Delta$. Thus, the coherence length can be described as the spatial extent of a Cooper pair, which has typical values from few ten to few hundred nanometers. Therefore, the Cooper pairs strongly overlap in the condensate.

2.3.2. Transport in superconductor - normal metal structures

Superconductors (S) coupled to a normal metal (N) provides a promising platform to study charge transport across the interface where current is carried by free electrons on the N side while Cooper pairs are responsible on the S side. This charge transport results in interesting effects in such N-S structures and we discuss the most relevant transport mechanisms in this section.

2.3.2.1. Andreev reflection and proximity effect

When an electron from N impinges on a completely transparent N-S interface at a subgap energy $|E| < \Delta$, transport across the interface is prohibited as there are no quasiparticle states available at this energy. At the same time, the

electron cannot be normally reflected back because a normal reflection inverts the momentum perpendicular to the interface, i.e. $p_F \rightarrow p_F$. This requires a net momentum transfer of $2p_F$ for normal reflection.

This requirement is satisfied by a simple second order process known as *Andreev reflection* (AR) [117], as depicted in Fig. 2.16b. The impinging electron with energy E and $|\mathbf{k}, \uparrow\rangle$ pairs up with another electron at energy $-E$ and $|-\mathbf{k}, \downarrow\rangle$ to form a Cooper pair such that a total charge of $2e$ is transferred across the interface. This results in the retro-reflection of a positively charged hole, i.e. the reflected hole travels backward on the path of the incident electron in N due to momentum conservation.

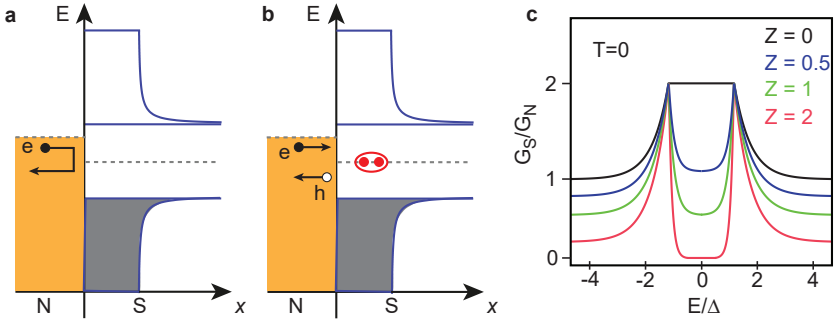

Figure 2.16. Andreev Reflection in a N-S interface. Illustrations of energy-real space diagrams for **(a)** normal reflection and **(b)** Andreev reflection of an electron incident at the N-S interface at $x = 0$. **c.** Normalized differential conductance G_S/G_{N0} for a N-S junction at $T = 0$ for different barrier strengths Z according to the BTK model, where G_{N0} is the conductance for the normal state at $Z = 0$. Figures adapted from Refs. [67, 69, 86]

This transport process can be described by the BTK model [118], where the scattering at the N-S interface is described by a delta function potential $V(x) = Z\hbar v_F \delta(x)$ with a dimensional barrier strength Z, which accounts for elastic scattering. For $Z = 0$, only Andreev reflection takes place resulting in a conductance $G_S = 2G_N$ for electrons with energy $|E| < \Delta$, as depicted in Fig. 2.16c. However, $Z \neq 0$ in real samples due to Fermi velocity mismatch in different materials. Thus, the subgap conductance G_S decreases for increasing Z due to an increase in the probability of normal reflections. As a result, a 'soft gap' begins to appear. Further increase of Z to $Z \gg 1$, Andreev reflection is strongly suppressed for $|E| < \Delta$ and we start to observe quasiparticle DOS in S for $|E| > \Delta$. This limit represents tunneling spectroscopy through a N-insulator-S junction.

Due to time-reversal symmetry, an incident hole is retro-reflected as an

electron resulting in a removal of a Cooper pair from the condensate. The incident hole and retro-reflected electron stays phase coherent in N for some time and distance resulting in a non-zero probability of finding a Cooper pair in N. Therefore, the Cooper pair density does not suddenly drop to zero at the N-S interface, but decays continuously on the scale of the BCS coherence length ξ in N. This is known as the proximity effect, which is due to the phase coherence of AR in N such that Cooper pairs 'leak' into normal metal materials in contact with S. Macroscopically, the proximity effect can be described by the framework of Ginzburg-Landau theory [116]. In addition, the *inverse proximity effect* also occurs where electrons and holes can enter S without being converted into Cooper pairs on the length scale of $\sim \xi$.

2.3.2.2. Crossed Andreev reflection

Since the Cooper pairs have a spatial extent on the length scale of ξ, an incident electron (hole) can be retro-reflected as a hole (electron) at a different position with distance $d < \xi$ apart. In a typical multi-terminal device where two N contacts are attached to S as shown in Fig. 2.17a, one can obtain cross-conductance channels between the two N contacts. This non-local Andreev reflection is known as *crossed Andreev reflection* (CAR) [118]. As shown in Fig. 2.17a-b, an incident hole from N_1 is reflected as an electron in N_2, which corresponds to splitting of a Cooper pair into two separate N contacts. Therefore, CAR is a suitable process for separating spin-entangled electrons. Although, CAR was observed in metallic N-S-N structure [119], its signature is hindered by the competing process of 'non-local normal reflection' where the incoming electron can propagate between N_1 and N_2 via a virtual quasiparticle state in S, as shown in Fig. 2.17c-d. This process is called *elastic cotunneling* (EC), analogous to the co-tunneling in QDs. Both EC and CAR has a similar probability amplitude that decays on the scale of ξ and masks the signature of CAR in metallic systems [120].

2.3.3. Cooper pair splitting

Cooper pair splitting (CPS) is described as the process in which the two electrons of a Cooper pair are split into separate terminals. Although CAR was shown to provide pairs of spatially separated spin entangled electrons in metallic S-N-S systems, it is often hidden by the competing local and elastic co-tunneling processes. Therefore, *Recher et al.* [121] proposed to use the electron-electron interactions in a tunable QD inserted between the S and N to suppress the competing processes and enforce CPS. A typical *Cooper pair splitter* (CPS) device and the corresponding energy level diagram at zero bias $V_{SD} = 0$ is shown in Fig. 2.18a and Fig. 2.18b respectively, where the notations used to describe the two QDs (QD1 and QD2), the two normal leads (N_1 and

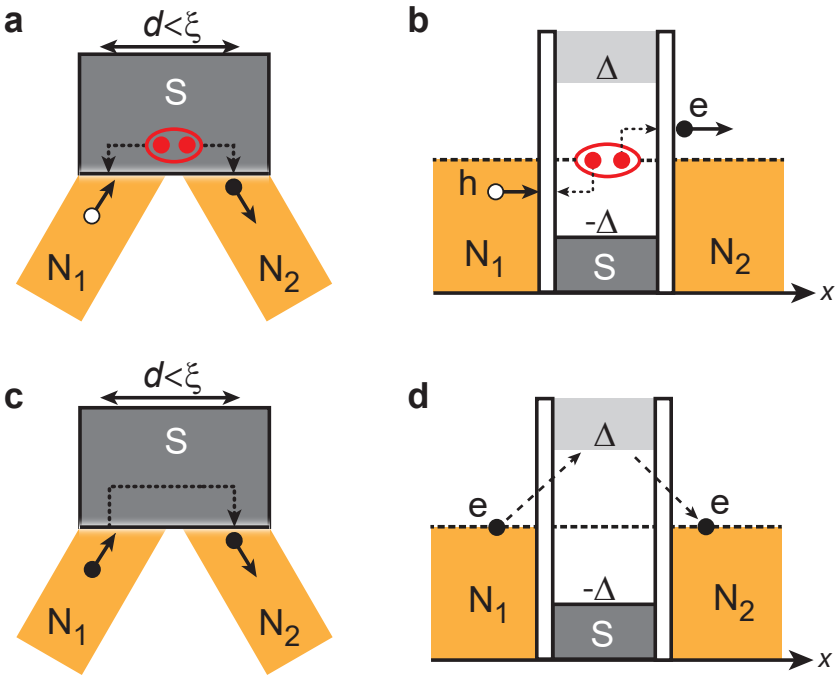

Figure 2.17. Crossed Andreev Reflection. Schematics of crossed Andreev reflection for a three terminal N-S-N device in **(a)** real space, and **(b)** energy space diagrams. **(c,d)** Elastic co-tunneling via a virtual quasiparticle state in S shown in **(c)** real space, and **(d)** energy space diagrams. Figures adapted from Refs. [67, 69].

N_2) and the superconductor are as introduced earlier. In addition, δr is the spatial separation between tunneling points of the two electrons in a Cooper pair and Γ_{12} is the inter-dot tunnel coupling strength.

2.3.3.1. Cooper pair splitter with quantum dots

The main concept in the above CPS device scheme is to enhance the CAR process by the combination of two main effects: the Coulomb interaction or charging energy $E_{c1} = E_{c2} = E_c$ on each QD and the pairing interaction Δ in S. These effects contribute in suppressing the local pair tunneling (LPT) of Cooper pairs into the same arm of the CPS device [121]. The two primary mechanisms for LPT are shown in Fig. 2.19. The Cooper pair electrons can

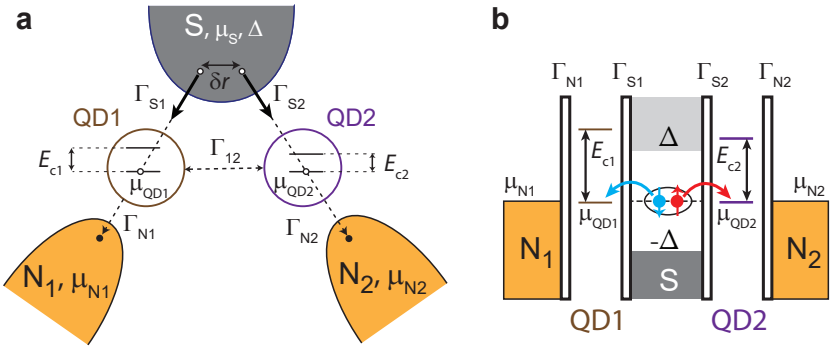

Figure 2.18. Cooper Pair Splitter. a. Schematics of a Cooper pair splitter (CPS) device illustrated with the characteristic energy scales and parameters. δr denotes the spatial separation between the tunneling points of the two electrons in a Cooper pair. **b.** Energy level diagram showing Cooper pair splitting at zero bias $V_{SD} = 0$, where $\mu_S = \mu_{QD1} = \mu_{QD2} = \mu_D$. Adapted from Refs. Figures adapted from Refs. [67, 69].

simultaneously occupy the same QD at an energy cost of E_c and tunnel to the respective N (Fig. 2.19a). The double occupancy of a QD in such a process is suppressed by the Coulomb interaction $\sim 1/E_c$, which can be controlled by the size of the QD. Alternatively, the two electrons can sequentially tunnel through a QD into the same lead (Fig. 2.19b). This is observed when one electron of a split Cooper pair tunnels onto a QD, while the other electron occupies a virtual quasiparticle state at energy $> \Delta$ in S. The first electron then tunnels into the lead followed by the second electron. Such a process is suppressed by $\sim 1/\Delta$ due to the virtual excitation of a quasiparticle. In contrast, E_c and Δ does not affect the CPS process, and hence the ratio I_{CPS}/I_{LPT} can be tuned to large values by increasing E_c and Δ.

In addition, the applied bias $|eV_{SD}|$ and the temperature k_BT has to be smaller than E_c and Δ for effective Cooper pair splitting. Another important parameter is the lifetime broadening $\Gamma_{1,2} = \Gamma_{S1,S2} + \Gamma_{N1,N2}$ of each QD. When the broadening $\Gamma = \Gamma_1 = \Gamma_2$ becomes comparable to Δ or E_c, the lifetime of the QD states $\tau \sim \hbar/\Gamma$ corresponds to an energy uncertainty that is compatible with LPT processes rendering the CPS process ineffective. Therefore, $\Gamma \ll \Delta, E_c$ is one of the ideal working condition for a CPS device. Another important condition is to operate the device in asymmetric coupling regime with $\Gamma_N \gg \Gamma_S$. Such asymmetric coupling ensures that the QDs have vanishing occupation probabilities as electrons leave the QDs much faster to N than being replaced from S. This prevents any blockage of subsequent CPS

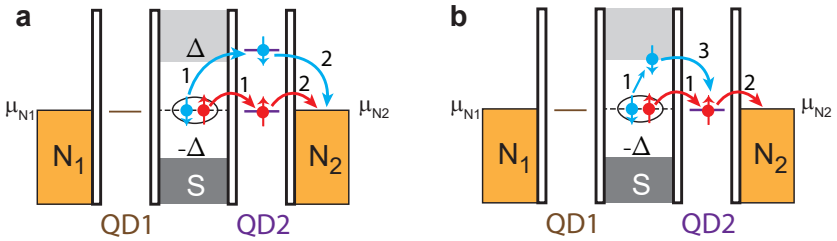

Figure 2.19. Local Pair Tunneling (LPT). a. Competing LPT process where the two electrons of a Cooper pair simultaneously tunnel into one arm (QD2) of a CPS device. This process is suppressed by the Coulomb interaction $\sim 1/E_c$. b. LPT process where the two Cooper pair electrons tunnel sequentially via a virtual quasiparticle state in S into QD2. Such processes are suppressed by $\sim 1/\Delta$ due to the superconducting gap. Figures adapted from Refs. [67, 69].

processes due to electrons occupying a QD for too long. Another coupling constant to consider is the inter-dot tunnel coupling Γ_{12}, which mainly arises due to direct tunnel coupling between QD1 and QD2 or elastic co-tunneling in S via a virtual intermediate state. When $\Gamma_N \gg \Gamma_{12}$, the electrons tunnel out to N before they could tunnel between QD1 and QD2. In contrast if $\Gamma_N \ll \Gamma_{12}$, the device acts as a Cooper pair beam splitter because the electrons can tunnel out to N_1 or N_2 at random. For $\Gamma_{N1} = \Gamma_{N2}$, the device behaves as a 50/50 beam splitter, resulting in an upper bound of 50% splitting efficiency. In order to achieve higher efficiencies beyond 50%, interactions play a crucial role in enforcing the splitting [121].

However, the spin-entanglement in a CPS device can be destroyed by spin-dephasing mechanisms, which swaps an entangled electron with another random spin electron. To suppress such dephasing processes, the level spacing δE of the QDs should be large: $\delta E \gg \Gamma, |eV_{SD}|, k_B T$. Otherwise, the QD might behave as a capacitive island, where an electron irrespective of its spin orientation can leave to N after the entangled electron enters the island. Furthermore, QDs exhibiting clear shell-filling patterns are desired to avoid unwanted correlation effects. Finally, electrons hopping from the Fermi leads, i.e. electron-hole pair excitations, can also occupy the QDs levels and potentially replace the entangled electron. Such excitations are more probable with strong coupling to the N leads. In order to suppress such processes, a sufficiently large bias $|eV_{SD}| > \Gamma$ should be typically applied to position the electrochemical potential of the normal lead well below the QD resonance, while keeping S resonant with both the QDs i.e. $\mu_S = \mu_{QDi}$.

In summary, the ideal working conditions of a CPS device with large splitting

efficiencies is given by:

$$E_{\mathrm{C}}, \Delta, \delta E \gg |eV_{\mathrm{SD}}| > \Gamma, k_{\mathrm{B}}T \qquad \Gamma_{\mathrm{N}} \gg \Gamma_{\mathrm{S}}, \Gamma_{12} \tag{2.27}$$

Quantitatively, the CPS current is given by:

$$I_{\mathrm{CPS}} = \frac{e\Gamma_{\mathrm{S}}^2\Gamma}{(\mu_{\mathrm{QD1}} + \mu_{\mathrm{QD2}})^2 + (\Gamma/2)^2} F(\delta r) \tag{2.28}$$

where μ_{QD1} (μ_{QD2}) is the electrochemical potential of QD1 (QD2), $\Gamma_{\mathrm{S}} = \Gamma_{\mathrm{S1}} = \Gamma_{\mathrm{S2}}$, $\Gamma = \Gamma_{\mathrm{N1}} + \Gamma_{\mathrm{N2}}$ and $F(\delta r)$ is a geometrical factor that depends on the separation of the tunneling points as discussed in detail below. When $\mu_{\mathrm{QD1}} = -\mu_{\mathrm{QD2}}$ ($\mu_{\mathrm{S}} = 0$), I_{CPS} has a maximum value of $I_{\mathrm{CPS}} = \frac{4e\Gamma_{\mathrm{S}}^2}{\Gamma} F(\delta r)$. Similarly, the LPT current is given by [121]:

$$I_{\mathrm{LPT}} = 2e\Gamma_{\mathrm{S}}^2\Gamma_{\mathrm{N}}\left(\frac{1}{\pi\Delta} + \frac{1}{E_{\mathrm{C}}}\right)^2 \tag{2.29}$$

where $\Gamma_N = \Gamma_{N1} = \Gamma_{N2}$. From Eq. 2.28 and Eq. 2.29, we can clearly see that I_{LPT} is suppressed by increasing E_{c} and Δ, while I_{CPS} is not affected. In Eq. 2.28, the CPS current is suppressed by a geometry dependent factor $F(\delta r)$ where δr is the spatial separation of the two tunneling points in S (Fig. 2.18). Intuitively, $F(\delta r)$ should decay rapidly when δr exceeds the BCS coherence length ξ. Although this term is heavily debated [121], the plausible term of $F(\delta r) \sim exp(-\delta r/\xi)$ captures the spatial extent of a Cooper pair. Therefore, the width $\omega \sim \delta r$ of S in a CPS device should be smaller than the BCS coherence length.

3 Experimental Methods

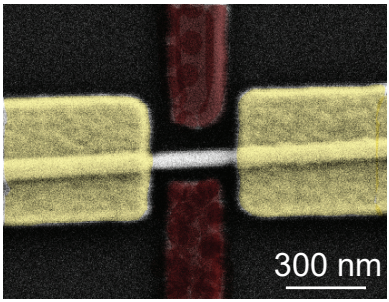

This chapter is dedicated to the description of the important experimental methods used in this thesis. The key fabrication techniques for different types of devices are introduced, with the exact fabrication parameters discussed in Appendix A. In addition, the basic principles and measurement setup for low temperature transport measurements are briefly described.

3.1. Sample fabrication

The fabrication of a suitable sample is the first essential step towards every project in this thesis. Obtaining clean InAs nanowire (NW) structures with good contacts is a prerequisite for all the presented measurements in this thesis. In this section, we introduce the most important techniques required to fabricate clean InAs NW structures. First, the fabrication of base structures with predefined markers and contact pads is discussed. Then a short description of depositing and cleaning the NWs on a substrate is presented, followed by the technique of contacting these deposited NWs. Standard nanofabrication procedures, such as electron-beam lithography (EBL), metallization with thermal or e-beam evaporation and standard wet etch methods are used to completely fabricate devices, but not discussed in details here. All the exact fabrication recipes are described in Appendix A.

Base structure fabrication

For all devices, we first need to create a grid of predefined markers and contact pads called *base structures* to deposit the NWs and consequently locate them with high precision. The base structures are fabricated on a highly p-doped silicon wafer, which acts as a global backgate (BG), with a 400 nm thick silicon oxide (SiO_2) as the top insulating layer. After cleaving the substrate into a 2 cm x 2 cm rectangular piece, the substrate surface is cleaned by ultrasonication in a beaker of acetone for 20 minutes, followed by 2-propanol (IPA) sonication for the same duration. The remaining solvents are finally blow dried using compressed nitrogen (N_2) gas.

We then fabricate the base structures on the clean substrate using standard EBL, followed by evaporation of a 5 nm/45 nm titanium/gold (Ti/Au) layer and subsequent lift-off using acetone at 50°C. Each base structure has a 2 mm x 2 mm area consisting of alignment markers, outer contact leads and bonding pads as shown in Fig. 3.2a. The central region contains a 500 μm x 500 μm square grid of unique fine reference markers separated from each other by 20 μm (Fig. 3.2b).

Nanowire deposition and readout

The next step is to deposit the NWs in the central region of the fabricated base structures. This requires the transfer of the NWs from the growth substrate to the sample substrate, which is done by using the sharp tip of a cut cleanroom tissue. By slightly touching the densely-packed growth substrate with the tissue tip, several NWs break off and stick to the tip of the tissue. The NWs are then placed on the sample substrate by gently pressing the tissue tip on the already fabricated base structures. The procedure is checked under the

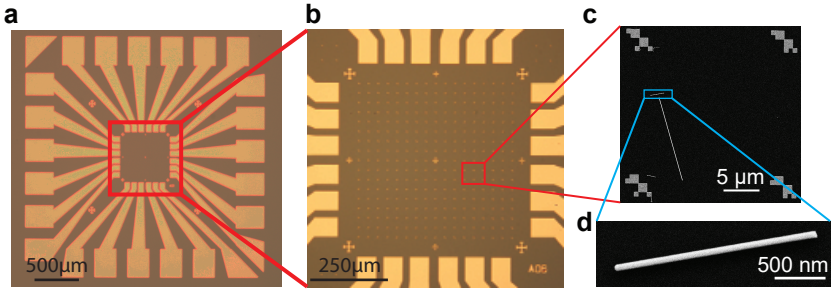

Figure 3.2. Base structure and nanowire (NW) imaging. Optical microscope image of **a)** a base structure and **b)** predefined markers for precise NW deposition and location. **c,d** Scanning electron microscope (SEM) image of a deposited NW near the predefined markers. Figure adapted from Ref. [86].

optical microscope and repeated until a desired number of NWs are placed on the sample substrate. The substrate is then cleaned again using acetone and IPA *without* ultrasonication and blow dried using N_2 to remove any dirt or unwanted particles from deposition.

We then image the NWs using a scanning electron microscope (SEM) to precisely locate the individual NWs with respect to the unique fine reference markers on the base structure, as shown in Fig. 3.2c,d . The NW position is then read out using a Python program developed by co-worker O. Faist, and the electrical contacts and gates specific for each NW are finally designed.

Nanowire metallization

The designed contacts are then patterned in a standard EBL process using 300 nm thick PMMA as the resist layer [114]. However in order to electrically contact the NWs, we have to remove the $2-3$ nm thick native oxide enclosing the InAs NW before metallization. This is done using a wet etch process known as sulfur passivation [122](exact recipe in Appendix A). Sulfur passivation is a self-terminating process which removes the native oxide of the NW and deposits a protective monolayer of S atoms on the NW. This layer prevents immediate reoxidation of the NW as well as locally dopes the contact area. The doping helps to achieve good ohmic contacts in wurtzite (WZ) crystal phase InAs NWs as the Fermi energy is shifted further up in the conduction band. The NW is then contacted using 5 nm/45 nm Ti/Au for normal contacts and 5 nm/70 nm titanium/aluminum (Ti/Al) for the superconducting contacts. A schematics of the standard fabrication process for typical InAs devices is shown

in Fig. 3.3.

In order to fabricate normal metal top/side gate electrodes, we evaporate 5 nm/45 nm Ti/Au *without* sulfur passivation. However for the ferromagnetic side gates (FSGs) made of Permalloy (Py), we use an optimized ZEP resist EBL process instead of PMMA, optimized in the Ref. [67] with the detailed parameters mentioned in Appendix A.

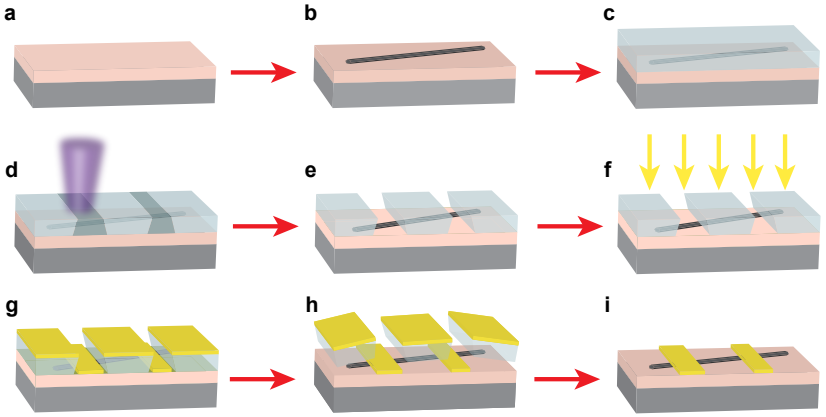

Figure 3.3. Standard fabrication process of an InAs NW device. a. Cleaned silicon (Si) substrate (grey) with 400 nm SiO_2 (pink) as insulating layer. **b.** NW deposition on the sample substrate. **c.** Spin coating of electron-beam resist with desired thickness. **d.** Patterned irradiation of the device design using electron-beam lithography (EBL). **e.** Development of exposed resist, followed by sulfur passivation. **f,g.** Metal evaporation onto the patterned substrate. **h.** Lift-off of the unexposed resists. **i.** Finished fabricated device. Figure adapted from Ref. [70].

Bonding to chip carrier

In the last step of fabrication, the sample substrate with the metallized NWs is glued to a commercially available non-magnetic chip carrier with conductive silver paste as shown in Fig. 3.4a. The silver paste provides an electrical connection to the highly p-doped silicon layer, which can then be used as a global back gate to tune the NW. Finally, the bond pads are connected to the chip carrier via standard wire bonding techniques by using a gold wire. The chip carrier is then built into a cryogenic measurement set-up, which is briefly described in the following section.

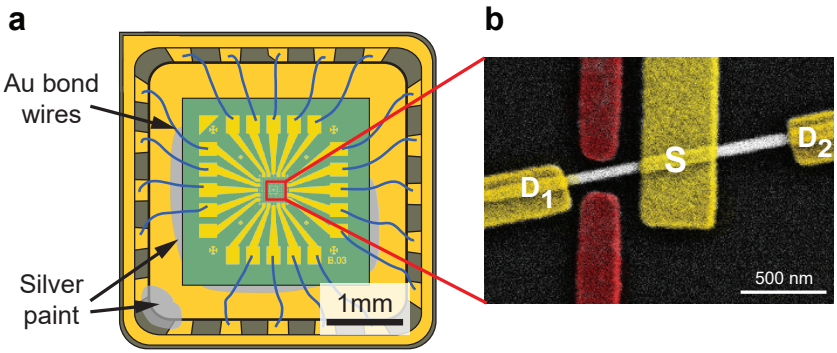

Figure 3.4. Wire Bonding. a. Schematics of a chip carrier where the sample substrate is glued with conductive silver paste and connected to the bond pads using gold (Au) bond wires. **b.** SEM image of a fabricated NW device with Ti/Au contacts and Permalloy side gates. Figure adapted from Ref. [70].

3.2. Cryogenic measurement set-up

Low sub-Kelvin electron temperatures are essential for resolving quantum mechanical phenomena, where the energy scales involved are in the order of meVs. For a typical QD, the thermal energy of the electrons should be ideally lower than the charging energy E_C and level spacing δE. In addition, devices with superconducting elements needs electron temperatures lower than the superconducting gap Δ and critical temperature of the material. This requires temperatures of $\leq$ 50 mK which is achieved in the lab using commercially available dilution refrigerators.

The sample can be quickly cooled down to 4.2 K by inserting it in liquid ^{4}He. The temperature can be further lowered to 1.4 K by pumping on the surface of liquid ^{4}He as it removes the latent heat. However to obtain temperatures two orders of magnitude lower, we use the technique of dilution refrigeration [124], where a mixture of ^{3}He-^{4}He spontaneously separates into ^{3}He-poor and ^{3}He-rich phases. An osmotic pressure difference is created between the two phases by pumping on the still. This results in an endothermic transfer of ^{3}He from ^{3}He-rich to ^{3}He-poor phase across the phase boundary, which in turn cools the mixing chamber. The phase transition is continuously driven using a circulation pump and 1K pot recondensation. The sample is simultaneously cooled by bringing it in good thermal contact with the mixing chamber using a cold finger, a metallic sample stage with high thermal conductivity usually made from copper.

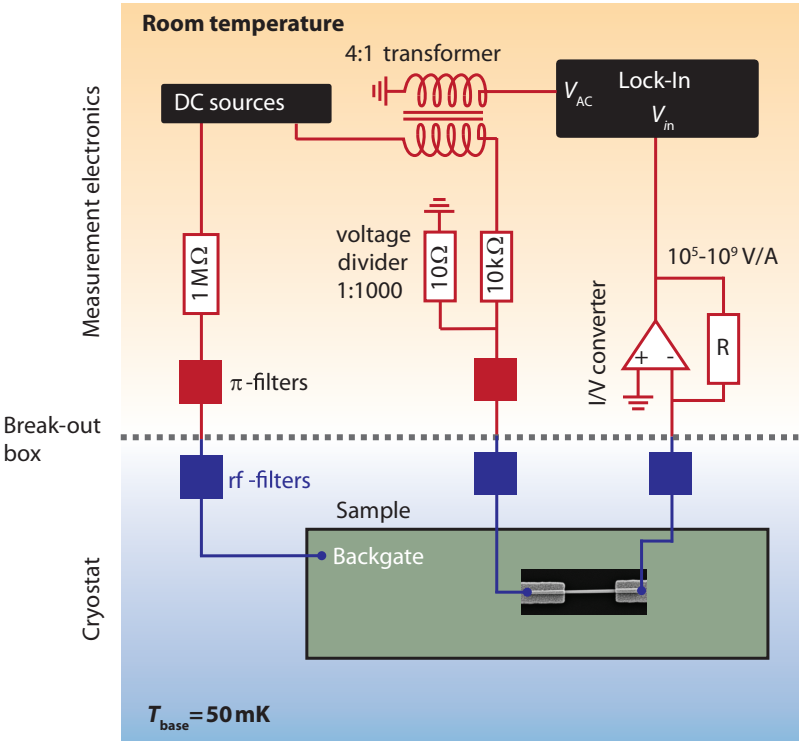

Figure 3.5. Schematics of a standard cryogenic measurement set-up. Typical measurement set-up for voltage biased differential conductance measurements of an InAs NW device at low temperatures (blue region) of $T = 50\,\text{mK}$. Figure adapted from Ref. [67, 68, 70, 86, 123].

The chip carrier is typically mounted on the cold finger using a corresponding chip socket. This chip socket is shielded from outside radiation by a Faraday cage and pumped to very low pressures in the inner vacuum chamber (IVC). It is connected to a room-temperature breakout box using twisted pairs to cancel out electromagnetic interference from external sources and cross-talk between the lines. The home-made breakout box acts as an interface between the cryostat wiring leads and the BNC cables of the room temperature measurement instruments. This enables us to individually address and ground each lead. Several filters are mounted in the cryostat wiring to suppress high frequency radiation and make the electron temperature go as low as possible. A home-built tapeworm filter with a cut-off frequency of 10 MHz is mounted

at the cold finger for this purpose. In addition, the breakout box is equipped with filters that have a cut-off frequency of around 1 MHz.

For differential conductance measurement, we employ standard low-frequency lock-in techniques, as shown in Fig. 3.5. In a typical two terminal measurement, we apply a AC bias to the source (S) contact using a SR830 (Stanford Research Systems) lock-in amplifier. The AC excitation signal is fed through a 4:1 step-down transformer and transposed with a DC bias signal supplied from a Yokogawa YK7651 DC voltage source. The combined signal is further reduced by a 1:1000 voltage divider to achieve $V_{\mathrm{ac}} \sim 10\,\mu\mathrm{V}$ excitation on the S contact. The resulting current is amplified using a low-noise I-V converter and the output voltage of the amplifier is measured in the lock-in to get the differential conductance $G = dI/dV$. The DC gate voltages were applied using a high resolution 8-channel DAC (digital-to-analog) converter, built by the electronics workshop, University of Basel. All the measurement instruments were controlled using the python-based data acquisition program QCodes.

4 Material Platform: Indium Arsenide Nanowires

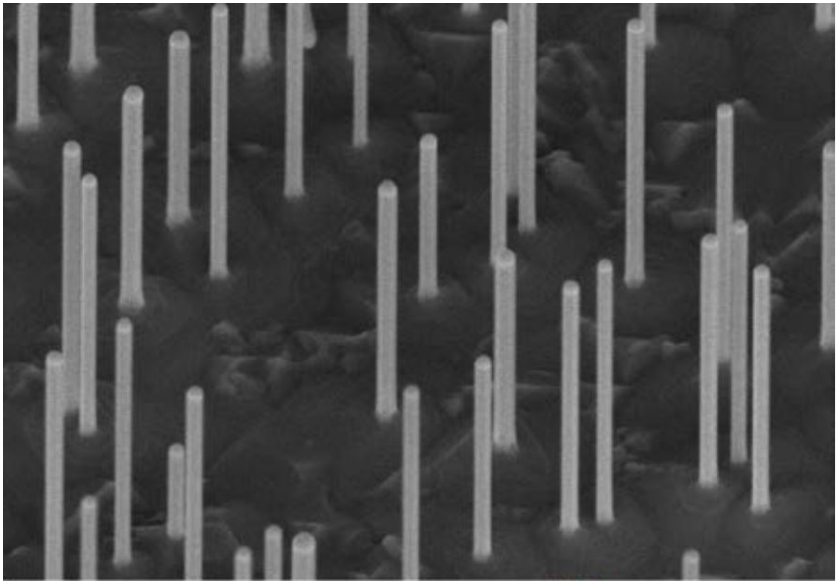

This chapter presents a brief description on the growth and electronic properties of the indium arsenide (InAs) nanowires (NWs) used in this thesis. In addition, a brief summary of various magnetotransport experiments previously performed with InAs NWs is described.[1]

[1] The above SEM image has been provided by Dr. Valentina Zannier, Pisa, Italy

Semiconducting indium arsenide (InAs) nanowires (NW) were chosen as the ideal material platform suitable for carrying out all the projects in this thesis. In general, semiconducting nanowires are crystalline one-dimensional nanostructures with small diameters up to few tens of nanometers and lengths in the range of few microns. NWs are typically synthesized from Group IV materials (Si, Ge), Group III-V alloys (Al, Ga, P, As, Sb), Group II-VI alloys (Cd, Zn-Se, O) and tertiary compounds, such as AlGaAs.

Semiconducting InAs NWs proved to be a versatile platform for various applications due to their low effective mass [125], high mobility [126–128], small band gap [129], tunable large g-factor [65, 130] and strong spin-orbit interaction [131, 132]. Therefore, they are extensively used to investigate fundamental physics on the nanometer scale, for example, as possible hosts of Majorana fermions [71, 133–136] for topological quantum computation [137–139], entanglement and correlation measurements [64, 140] using superconducting elements, as well as in the field of field of spintronics [11, 13, 14], magnetotransport [105, 141, 142], and thermoelectrics [143].

In this chapter, we present a brief introduction to the most important features of InAs nanowires: the growth mechanism and the electronic properties that affect electron transport. We also provide a short summary on previous magnetotransport experiments with InAs NWs.

4.1. Nanowire growth

Semiconducting NWs are generally grown in a bottom-up approach based on vapor-liquid-solid (VLS) methods [144]. As suggested by the name, it refers to the formation of solid crystals from vaporized precursors facilitated by liquid catalysts. This includes various techniques with the same principle such as chemical vapor deposition (CVD) [145], molecular beam epitaxy (MBE) [146], chemical beam epitaxy (CBE) [147, 148] and metal-organic vapor phase epitaxy (MOVPE) [149, 150].

In the VLS method, metal catalyst particles are first randomly formed on a substrate by one of the various processes, for example, direct deposition [151], aerosol techniques [152], metal evaporation followed by subsequent annealing [153] or by pre-patterning arrays using EBL and subsequently evaporating the metal [154]. Typically, gold is considered the best metal choice for the catalyst due to its great alloying capability and inertness to oxygen. The precursors from the vapor phase then strike the gold catalyst forming an alloy and supersaturating the catalyst (Fig. 4.2a), such that no further material can be accumulated. This results in the initiation of nucleation at the liquid-solid interface. A solid crystalline pillar of the precursor materials grow axially beneath the gold droplet, while the radial growth is suppressed as shown in Fig. 4.2b. The growth process is stopped by removing the vapor precursors.

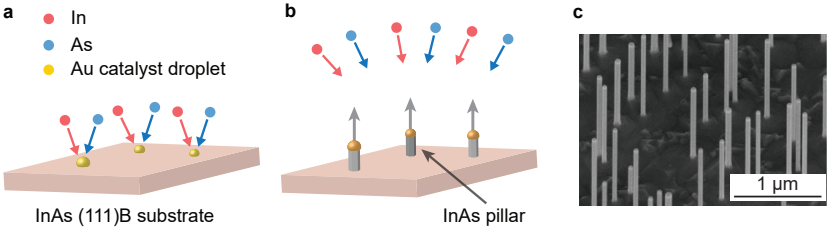

Figure 4.2. Illustration of the InAs NW growth process. a. Gold (Au) catalyst particles on an InAs (111)B substrate are fed with In (red) and As (blue) vapor precursors to supersaturate the Au particle and initiate nucleation at the solid-vapor interface. **b.** Growth of an InAs pillar in the axial direction beneath the Au particle. **c.** Scanning electron microscope (SEM) image of an InAs NW 'forest' on the InAs (111)B substrate. SEM image from the group of Prof. Lucia Sorba, Pisa. Figure adapted from Refs. [70, 86]

The different parameters such as diameter, crystal phase, growth rate and length of the NWs can be well-controlled during the growth process . The flux of the vapor precursors determine the growth rate, while the length of the NW depends on the growth time. The diameter of the NW is typically controlled by the size of the gold catalyst. However, by lowering the growth temperature, the catalyst can be deactivated allowing one to quench the axial growth and enable radial growth. Although the crystal phase of bulk InAs is zincblende (ZB) (Fig. 4.3a), defect free wurtzite (WZ) crystal phase InAs NWs (Fig. 4.3b) can also be grown under the right growth conditions with advanced growth techniques [72, 155, 156].

The InAs NWs used for all the devices in this thesis are grown in the group of Prof. Lucia Sorba (NEST Pisa) using VLS technique in a chemical beam epitaxy (CBE) environment [153]. A thin gold film is evaporated onto an InAs (111)B substrate, followed by thermal annealing inside the growth chamber to form randomly distributed gold nanoparticles with a diameter of 40 to 50 nm. The vapor precursors trimethylindium (TMIn) and tert-butylarsine (TBAs) are introduced in the system to start the NW growth. These precursors supersaturate the Au particle and a pillar of InAs start to grow beneath the Au nanoparticle. This procedure produces a "forest" of defect-free crystalline wurtzite InAs NWs in the growth chip as shown in Fig. 4.2c.

With recent technical advances, significant progress has been made in engineering various NW heterostructures. Complex geometries involving multiple NWs such as networks and crosses [157–160] using shadow evaporation techniques have become feasible. In-situ grown epitaxial superconducting half and full shell [161–163] around the NW has enabled a defect free interface for

superconducting hybrid devices [71]. Furthermore, different types of NW heterostructures have been achieved to form precisely located QDs in the NW. For example, in InAs/InP heterostructure NWs, two short InP segments are grown in-situ into the InAs NWs to form well-defined tunnel barriers [164, 165]. Similarly, a atomically precise controlled switching of the crystal phase between ZB and WZ has been achieved, where the WZ segments acts as tunnel barriers [72, 166].

4.2. Electronic properties

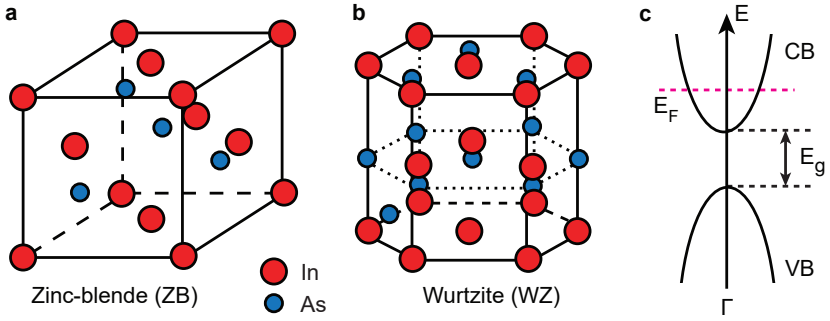

Figure 4.3. Crystal structure of InAs NWs. Crystal structure of **a)** face-centered cubic (fcc) zinc blende (ZB) InAs NW and **b)** hexagonal close-packed (hcp) wurtzite (WZ) InAs NW. **c.** Schematics of the electronic band structure around the Γ point of InAs, with a band gap of $E_g = 530\,\text{meV}$ [72]. Figures adapted from [86, 167]

The InAs NWs used in this thesis are n-type III-V semiconductors comprising of a hexagonal close-packed wurtzite crystal structure with a lattice constant of 4.25 Å, where the In and As are covalently bonded [168] (Fig. 4.3b). Although the semiconducting energy gap for bulk InAs with ZB crystal phase (Fig. 4.3a) is around $E_{\text{ZB}} = 0.47\,\text{eV}$, the WZ crystal phase has a larger conduction band (CB) and valence band (VB) separation of $E_{\text{WZ}} = 0.52{-}0.54\,\text{eV}$ [72]. The conduction band around the Γ point (Fig. 4.3c) yields a parabolic dispersion relation: $E_n(k_x) = E_n + \frac{h^2 k_x^2}{2m^*}$ with an effective mass of $m^* = 0.04\,m_e$ for the wurtzite InAs crystal phase [125], where m_e is the free electron mass and E_n is the minimum energy of a quantized subband. The resulting current $I = \frac{2e^2}{h}N$ depends on the number of subbands N and shows a step-wise increase in the ballistic quantized conductance when a new subband gets occupied, as demonstrated in the reference [169]. Furthermore, InAs NWs have

been shown to exhibit large g-factors of around $g = -14.9$ and strong SOI strength of 250 μeV [170].

In addition, the electrons are accumulated at the surface of InAs NWs resulting in electron transport predominantly through the surface. This pins the Fermi level at an energy of 200 meV above the conduction band minimum [171]. Therefore, it is easy to electrically contact InAs NWs [172], although they are susceptible to any surface treatment and electrostatic gating effects[173]. Due to the radial confinement and small diameters, the electron wavefunction in InAs NWs form quantized transverse modes. Such well-controlled growth techniques and suitable electronic properties of InAs NWs make them an ideal candidate for investigation of magnetotransport phenomena, as discussed in the following section.

4.3. Magnetotransport experiments in nanowires

The vast majority of the magnetotransport experiments extensively focused on the study of spin-orbit interaction using the phenomenon of weak antilocalization [142, 174]. These studies showed experimental evidence of strong spin-orbit coupling, with typical spin-orbit lengths and phase coherence lengths in the range of 60-250 nm and 100-800 nm respectively. Electrical tunability of the SOI lengths was also demonstrated using devices with top gate [175], side gate as well as liquid gates [174]. The spin-orbit energy has also been measured from avoided singlet-triplet crossing in excited state spectroscopy of single QDs [176] and hybridization induced by orbital Kondo effects in strongly coupled devices [177]. The spin-orbit energy was found to be anisotropic and tunable by externally applied electric fields. The SOI was also investigated by determining the leakage current in spin blockade in DQD systems [97]. These measurements reported Rashba type SOI in semiconducting NWs. Such evidence of strong SOI strengths is suitable for studying the induced 'helical' gap, whose first signatures have been recently reported [178].

The strong SOI results in a large g-factor for both bulk InAs as well as InAs NWs [65]. The anisotropy and tunability of g-factor has been extensively studied [65], making InAs NWs an ideal candidate to selectively address individual qubits. Various experiments with InAs NWs have demonstrated electron dipole spin resonance (EDSR) and demonstrated various types of qubits such as spin-orbit qubits [132], spin qubits [179] and charge qubits [180] in the presence of stray field from micromagnets. These studies revealed Rabi oscillations and demonstrated long T_1 coherence times for spin qubits [8, 9].

In the superconducting domain, InAs NW DQDs have been used to demonstrate Andreev molecules [181] and study their magnetic field evolution. They have gained a lot of interest as potential platform for topological quantum computation [137–139]. Topological states, such as Majaorna fermions [71, 133–

136], were demonstrated in these NWs under the application of a magnetic field parallel to the NW. More recently, they were demonstrated in zero external magnetic field utilizing the proximity induced exchange coupling from a ferromagnetic insulator in an epitaxially grown semiconductor-superconductor-ferromagnet NW [182].

In the field of spintronics, InAs NWs constitute an integral platform for spin valve devices both at low temperatures as well as room temperature. They are extensively used for studies aimed at increasing the efficiency of spin injection into semiconducting nanostructures as well as efficient spin detection [105]. However, they are mainly achieved using ferromagnetic contacts which are limited by their low spin polarization and low tunability. In contrast, we require a highly efficient and tunable spin injectors and detectors to detect small spin correlation signals in a purely electronic system, such as Cooper pair splitters [52, 59]. Therefore, we investigate a new approach using local stray magnetic fields from ferromagnetic nanomagnets in Chapter 5, which is then implemented in Chapter 6 to demonstrate efficient spin injection and detection as well as perform spin readout measurements in close proximity to a superconductor in Chapter 7.

5 Investigation of building blocks: Ferromagnetic Side Gates with InAs Nanowire Single Quantum Dot

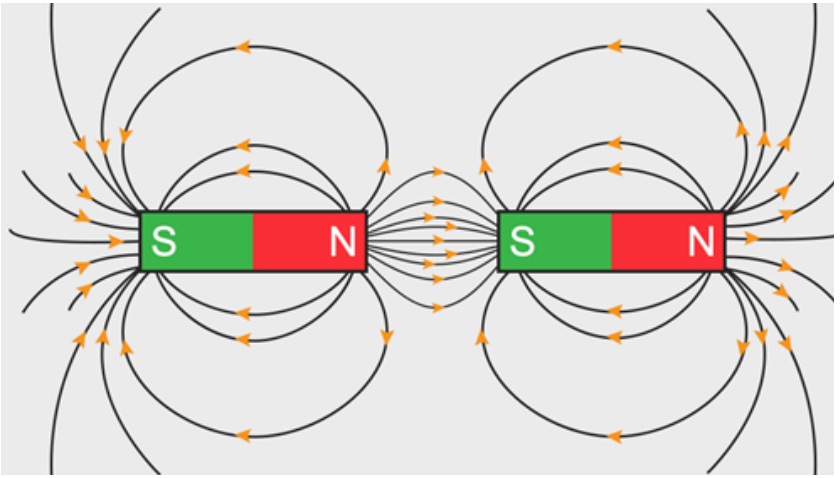

In this chapter, we investigate magnetoconductance (MC) experiments for a single quantum dot (QD) with ferromagnetic split gates (FSGs). We determine the generated stray field and switching (coercive) field of the FSG from the hysteretic MC of Coulomb blockade resonances. In addition, we present a control experiment to determine the stray magnetic field far away from the FSG in the same device. We also present MC measurements using Cobalt (Co) as the ferromagnetic material.[1] [2]

[1] Parts of this chapter has been published in a similar form in [105].
[2] The above image has been adapted from sciencestruck.com.

5.1. Introduction

Recent proposals, such as Majorana fermion detection by selective equal spin Andreev reflections [183], generation of fractional fermions [184–189] through synthetic spin orbit coupling [190] and spin entanglement/correlation measurement schemes [62, 140] in Cooper pair splitters [52, 59] have attracted a lot of attention in topological quantum computing with superconductors. One of the key requirements in these experiments is to obtain a non-zero local Zeeman splitting in close proximity to superconductors for spin filtering and read-out. This prohibits the use of global external magnetic field, which completely suppresses superconductivity. The conventional approach of spin read-out using ferromagnetic contacts is problematic [140, 191] due to significant obstacles like low spin polarization (20%-40%) [110], conductivity mismatch at the metallic ferromagnet-semiconductor interface [111]. An alternative approach is to achieve such splitting using the localized switchable stray magnetic fields [192] from tailored ferromagnetic nanomagnets [179, 180, 193, 194]. The generated stray fields from such nanomagnets need to be large enough to produce an appreciable Zeeman splitting. Therefore, InAs nanowires constitute the ideal platform for implementation of such experimental schemes due to its large g-factor of $g^* = -14.9$ in bulk as well as quantum dots (QDs) [65, 66].

In this chapter, we discuss the approach of using stray magnetic fields generated from nanomagnets to control electron spins in a QD. We present proof-of-principle magnetoconductance (MC) experiments for a single QD using a pair of Permalloy (Py) split-nanomagnets, which we term as ferromagnetic split gates (FSGs). We deduce the generated stray field and switching (coercive) field of the FSG from the hysteretic MC of Coulomb blockade resonances. As a control experiment, we determine the stray magnetic field far away from the FSG in the same device. This demonstrates the suitability of implementing our approach in hybrid semiconductor-superconductor devices. We further present MC measurements using Cobalt (Co) as the ferromagnetic material, which is expected to generate a larger stray field than Py due to its higher saturation magnetization.

5.2. Permalloy FSG properties

Permalloy is a soft ferromagnetic material that has been extensively used for many applications due to its properties such as high magnetic permeability, low coercivity and single domain magnetization [196]. Due to its dominant shape anisotropy, the magnetization reversal in long Py strip can be easily measured in near parallel anisotropic magnetoresistance (AMR) measurements [106]. The magnetization switching fields can thus be engineered by varying the geometrical width of the Py strip.

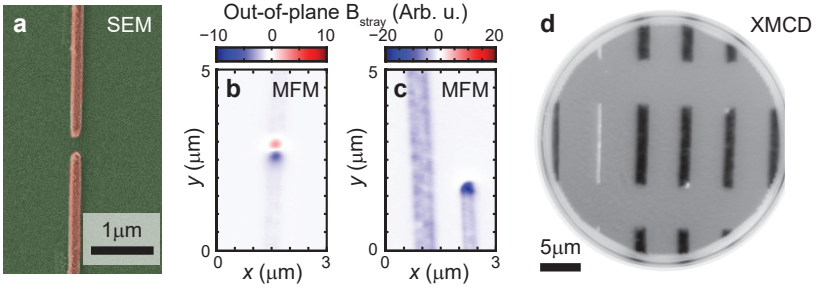

Figure 5.2. Stray field imaging of Permalloy FSG strips. a Scanning electron microscope (SEM) image of a permalloy FSG. **b,c** Magnetic force microscopy of stray magnetic fields generated by a FSG and a single Py strip. **d** Domain structure of Py strips measured by X-ray magnetic circular dichroism (XMCD). All the characterizations were carried out by Dr. Gabor Fabian, Dr. Andreas Baumgartner, Dr. Simon Zihlmann and Dr. Peter Makk in the Hug lab at EMPA, Switzerland (MFM) and the SIM beamline at Paul Scherrer Institut, Switzerland (XMCD) [70, 195].

For the FSGs fabricated in our device, the end domains i.e. the domain structures at the tip of the FSG, plays an important role in determining the strength of the stray fields. The magnetic properties of such Py FSG strips were examined using magnetic force microscopy (MFM) and X-ray magnetic circular dichroism (XMCD). The above characterizations were carried by Dr. Gabor Fabian, Dr. Andreas Baumgartner, Dr. Simon Zihlmann and Dr. Peter Makk in the Hug lab at EMPA, Switzerland (MFM) and the SIM beamline at Paul Scherrer Institut, Switzerland (XMCD) [70, 195].

MFM probes the spatial distribution of the out-of-plane component of B_{str} near the FSG gap by measuring the force on a magnetic AFM tip. The imaged stray fields, shown in Fig. 5.2b,c, reveals an out-of-plane component strongly confined to the FSG gap. The two tips of the FSGs show opposite polarity signifying that the stray field lines originate from one FSG tip and terminates at the other tip. This results confirm that the stray field is predominantly confined to the FSG gap and parallel to the magnetization strips. In contrast, the tip of a single FSG strip showed stray fields with only one polarity, signifying field lines originating from the tip and terminating elsewhere. The FSG bulk displayed minimal stray magnetic fields, which is consistent with the formation of single domains along the Py strip [70, 106, 196].

The domain structures for the Py strips with different widths were characterized using the XMCD technique. Single domain structure was observed for most of the Py strips, as illustrated by the homogeneous response in the

XMCD data in Fig. 5.2d. However, for strips with width $\sim 1\,\mu$m, small spots at the corners of the strips were observed, which might indicate the formation of closure domains [67, 70]. Similarly, multiple domains are observed for FSGs with width $\sim 100\,$nm. Such effects could be mainly due to imperfect edges during EBL or contaminants during fabrication, which pins the domains at the FSG ends. However, we observe complete single domain magnetization for FSG strips with width of $120 - 200\,$nm, which makes them suitable for use in our device.

5.3. Device and Characterization

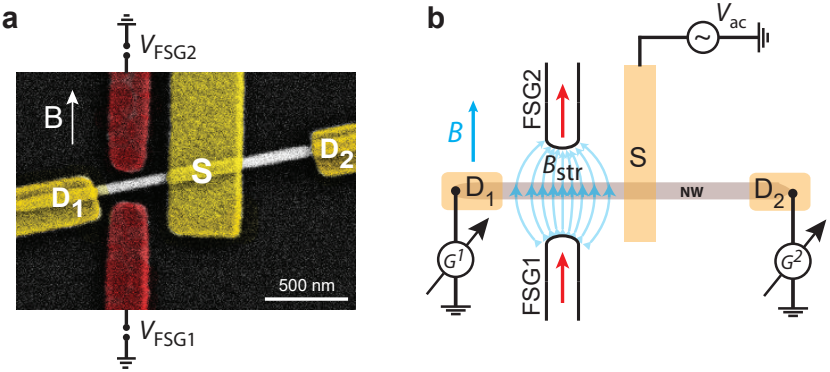

Figure 5.3. Single QD-FSG Device. **a** False color SEM image and **b** schematics of the investigated 3-terminal NW device. The FSG is located at a distance of 35 nm from the NW.

The primary aim of our device is to generate and measure a large stray magnetic field localized in the FSG gap. A false color SEM image and schematic diagram of the investigated device is shown in Fig. 5.3. The device is 3-terminal InAs NW contacted with titanium/gold (Ti/Au) normal metal contacts S, D_1 and D_2. In both the NW segment S-D_1 and S-D_2, a QD (QD1 and QD2) is formed between the two normal metal contacts respectively. However, a pair of Permalloy (Py) FSGs is fabricated in the NW segment S-D_1 such that QD1 experiences a local stray magnetic field. In contrast, we use the NW segment S-D_2 without any FSGs as a control experiment to determine the stray magnetic field away from the FSGs [192]. For our device, the tips of the FSGs are relevant in contrast to the bulk properties of ferromagnetic (F) contacts in conventional spin valves. The tips of the FSGs are prone to formation of closure domains, which decreases the effective stray field in the FSG gap. Such

closure domains can be reduced by minimizing the FSG gap such that the magnetization of the two nanomagnets gets coupled due to their close proximity. This also results in a homogeneous stray field in the FSG gap, and sharp decay outside. Furthermore, the magnetization orientation of the FSGs can be reversed by sweeping an external magnetic field through the coercive field of the FSG strip. The switching field of such a long FSG strip is determined by the width of the FSGs due to its shape anisotropy. In general, our technique without any ferromagnetic contacts avoids the potential issues associated with ferromagnet-semiconductor interfaces.

In our device, the InAs NW has a diameter of around 40-45 nm and the two NW segments S-D_1 and S-D_2 have similar lengths of $L \sim 400\,\text{nm}$. The FSG is 170 nm wide and made up of 30 nm thick Py. The tip of the FSGs are at a distance of 35 nm from the NW and the electrical contacts to the NW are made of 5 nm/45 nm titanium/gold (Ti/Au). We apply a dc (V_{SD}) and ac bias to the source S contact and simultaneously measure the differential conductance $G^{(1,2)} = \frac{dI_{1,2}}{dV}$ at contacts D_1 and D_2 using standard lock-in techniques at a base temperature $T = 50\,\text{mK}$.

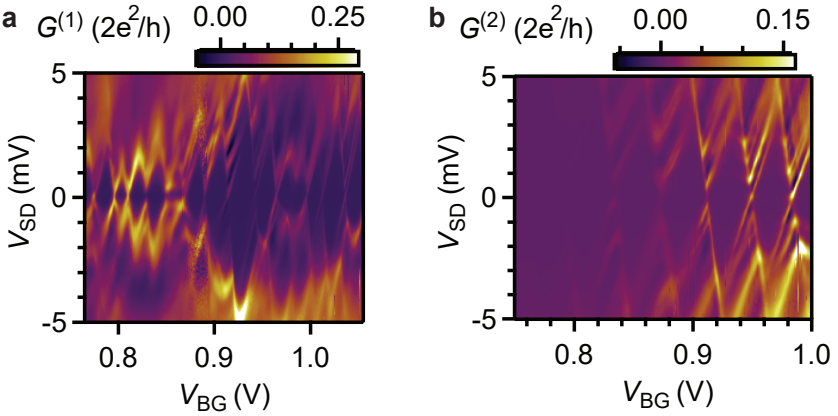

Figure 5.4. Device Characterization. Differential conductance **a** $G^{(1)}$ and **b** $G^{(2)}$ as a function of dc bias V_{SD} and back gate voltage V_{BG} showing Coulomb blockade diamonds for the NW segment **a** $S - D_1$ and **b** $S - D_2$ respectively.

We first investigate the electronic transport properties of the device at zero external magnetic field, i.e. $B = 0$. Both the NW segments are simultaneously tuned using the global backgate (BG). In addition, the NW segment S-D_1 is further tuned using V_{G2}, while V_{G1} is kept at a constant potential of $V_{\text{G1}} = 0$. Fig. 5.4a and Fig. 5.4b shows the colorscale plots of $G^{(1)}$ and $G^{(2)}$ as a function

of the applied V_{SD} and backgate voltage V_{BG}. We observe a regular pattern of Coulomb Blockade (CB) diamonds, suggesting the formation of a single QD in both NW segments. From the size of the Coulomb diamonds, we can deduce an addition energy of $E_{add,1} \approx 2\,\text{meV}$ for QD1 and $E_{add,2} \approx 3.8\,\text{meV}$ for QD2 in the NW segments S-D_1 and S-D_2 respectively.

5.4. Magnetotransport Measurements

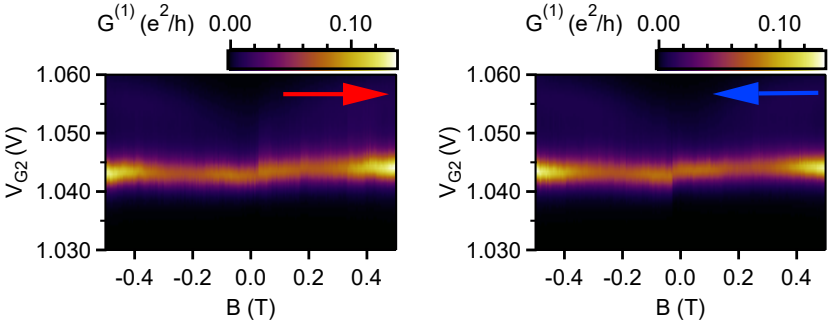

Figure 5.5. Magnetoconductance measurements. $G^{(1)}$ as a function of external magnetic field B and gate voltage V_{G2} for the **a** up (red) and **b** down (blue) sweep of a QD resonance, with $V_{SD} = 0$, in the NW segment $S - D_1$.

We now measure the magnetoconductance $G^{(1)}$ as a function of V_{G2} at a series of external magnetic field B for multiple QD1 resonances. The backgate is kept constant at $V_{BG} = 1.2\,\text{V}$. We apply B along the FSG long axes such that the FSG domains align along the long axis. Such a colormap for a particular QD1 resonance is shown in Fig. 5.5 for increasing and decreasing magnetic fields, as indicated by the red (up sweep) and blue (down sweep) arrow respectively. The magnetic fields are first swept to $B = -1\,\text{T}$ ($B = 1\,\text{T}$) for the up (down) sweep to ensure the formation of a single magnetic domain in the FSGs. The maps are clearly hysteretic with strong dependence on B and the sweep direction. In order to study this behavior more explicitly, we extract the postion, width and maximum conductance $G^{(1)}_{max}$ at each B value. This is achieved by taking individual gate cross sections at each B in Fig. 5.5 and then fitting them with a Lorentzian to obtain the peak height, peak position and full width at half maximum (FWHM). $G^{(1)}_{max}$ extracted from Fig. 5.5 is shown in Fig. 5.6a for increasing (red) and decreasing B (blue), along with the peak position in V_{G2} (Fig. 5.6b) and FWHM (Fig. 5.6c). The same parameters for two other QD1 resonances are shown in Fig. 5.6d-i.

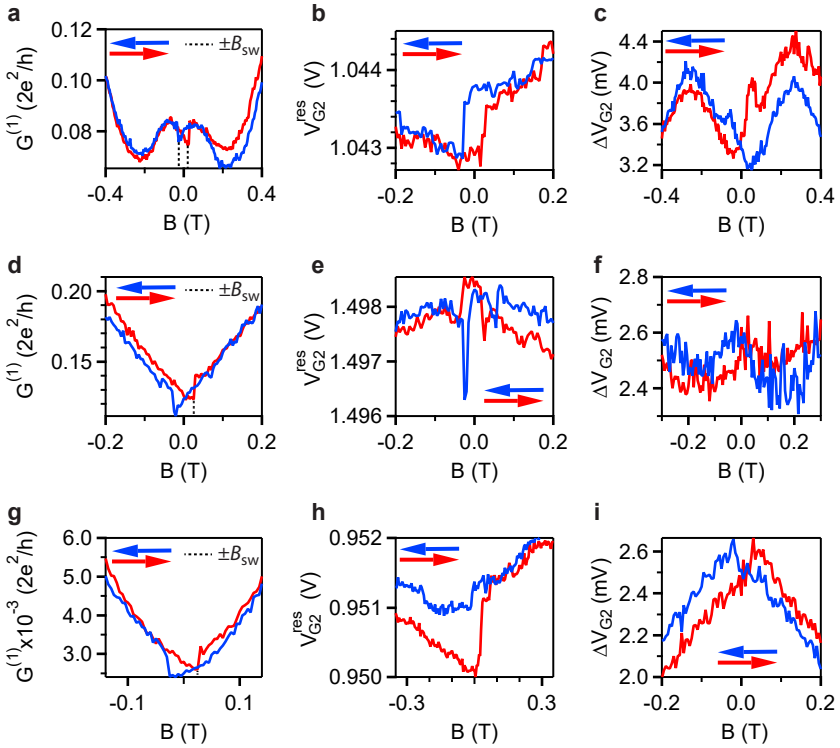

Figure 5.6. Overview of magnetoconductance features. a,d,g Maximum amplitude, **b,e,h** resonance position in V_{G2}, and **c,f,i** resonance width as a function of B for three different QD resonances for the up (red) and down (blue) sweep with $V_{SD} = 0$ in the NW segment $S - D_1$.

The maximum conductance $G^{(1)}_{max}$ for all three resonances (Fig. 5.6a,d,g) are clearly hysteretic for the up (red) and down (blue) sweeps and mirror symmetric around $B = 0$. For Fig. 5.6a, the hysteresis can be qualitatively understood as a smooth non-monotonous magnetoconductance (MC) of the single QD, which changes abruptly with the reorientation of the FSG magnetization. As we sweep the external magnetic field, the orientation of the stray magnetic field changes at the switching (coercive) field of the FSG strips. This leads to a discontinuity in the smooth MC of QD1, which is visible at $B_{sw} = +25\,\mathrm{mT}$ for the up sweep and $B_{sw} = -25\,\mathrm{mT}$ for the down sweep, respectively. The $G^{(1)}_{max}$ curves in Fig. 5.6d and Fig. 5.6g also exhibit similar characteristics. We

note that we only observe a single switching feature, suggesting that the magnetization reversal of the two parts of the FSG are in unison. This further supports the fact that the magnetic domains in both the FSG strips form a single unfiorm domain structure. In contrast, the resonance positions and resonance widths do not show any sharp switching in both sweep directions together except Fig. 5.6b, although the resonance widths (Fig. 5.6c,f,i) show clear hysteresis around $B = 0$. Since, only the maximum conductance exhibits sharp switching features for all three QD resonances, we therefore use $G^{(1)}_{\max}$ vs B curves to determine the stray field in the FSG gap.

5.5. Stray Field in the FSG Gap

Although a direct measurement of B_{str} in the FSG gap is not possible in the present device, we can indirectly determine B_{str} from the hysteretic $G^{(1)}_{\max}$. This can be done by two methods: (1) the method of *shifting curves*, and (2) the method of *interpolation*. For the sake of conciseness, we describe the two methods for the resonance shown in Fig. 5.6a. However, B_{str} for the other resonances in Fig. 5.6d,g can be determined in a similar manner.

Method of shifting curves

Quantitatively, for a two terminal device with $B_{\mathrm{str}} = 0$, the magnetoconductance $G_0(B)$ can be necessarily described as an even function in the external magnetic field B:

$$G_0(-B) = G_0(+B) \tag{5.1}$$

This relation allows us to determine the stray field of the FSGs assuming $\vec{B}_{\mathrm{str}} || \vec{B}$. For a given $G_0(B)$, we can define the hysteretic $B_{\mathrm{str}} \neq 0$ curves as the result of a constant stray field offset along the B axis, i.e. $G_-(B) = G_0(B - B_{\mathrm{str}})$ for the up sweep up to $B \leq +B_{\mathrm{sw}}$ and $G_+(B) = G_0(B + B_{\mathrm{str}})$ for the down sweep down to $B \geq -B_{\mathrm{sw}}$. From equation 5.1, we can then find:

$$G_+(B) = G_-(-B) \qquad G_+(B) = G_-(B + 2B_{\mathrm{str}}) \tag{5.2}$$

Eq. 5.2 describes that the up ($G_-(B)$) and down sweep ($G_+(B)$) are symmetric around $B = 0$. In addition, the down sweep curve can be obtained from the up sweep by a shift of $+2B_{\mathrm{str}}$ along the B axis and vice-versa. Assuming a particular B_{str} value, we compare the down sweep curve obtained by shifting the up sweep with the measured down sweep and iterate the process with different B_{str} values until they match. We determine $B_{\mathrm{str}} \approx 85\,\mathrm{mT}$ for the resonance in Fig. 5.6a using this method, as shown in Fig. 5.7a. In addition, we can also obtain the zero magnetization $B_{\mathrm{str}} = 0$ curve $G_0(B)$ by shifting the up sweep by $+B_{\mathrm{str}}$ (Fig. 5.7b).

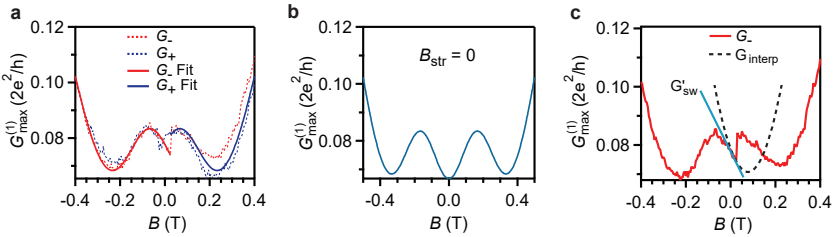

Figure 5.7. Determination of the stray field in FSG gap. a,b $G^{(1)}_{\max}$ vs B showing **a** the up (G_ Fit) and down (G$_+$ Fit) shifted curves, and **b** zero magnetization $B_{\rm str} = 0$ curve, obtained by the method of shifting curves. **c** $G^{(1)}_{\max}$ vs B for the up sweep showing the slope ($G'_{\rm sw}$) at $B = B_{\rm sw}$ and the interpolated parabola ($G_{\rm interp}$), resulting in $B_{\rm str} \approx 80$ mT.

However, this method of shifting curves is limited in its accuracy for two reasons. Firstly, the determined $B_{\rm str}$ is a lower bound estimate as we do not have any information of the MC curve after the switching fields. For the up sweep at $+B_{\rm sw}$, the stray field changes sign from $-B_{\rm str}$ to $+B_{\rm str}$ and the smooth MC abruptly jumps from $G_-(B) = G_0(B - B_{\rm str})$ to $G_+(B) = G_0(B + B_{\rm str})$. This forbids us from determining the B dependence of $G_-(B)$ beyond $+B_{\rm sw}$. The $G_-(B)$ MC curve might have multiple extremums between $+B_{\rm sw} < B < B_{\rm str}$. Secondly, we cannot quantify the goodness of the fit between the measured and the shifted down sweep. This leads to an inevitable systematic error in the determination of $B_{\rm str}$. Therefore, we implement the method of interpolation that might circumvent some of these limitations.

Method of interpolation

In this method, we use a polynomial, or any other suitable function, to interpolate the data of $G_-(B)$ up to $+B_{\rm sw}$ and use the same function to extrapolate to the next extremum, where $\frac{dG_-(B)}{dB}|_{B=B_{str}} = 0$ by symmetry. This allows us to directly read off $B_{\rm str}$ instead of relying on the goodness of a fit. For a simple analytical estimate of $B_{\rm str}$, we use the lowest order even polynomial $G_{\rm interp} = a(B - B_{\rm str})^2 + b$. The curvature a is fixed to the maximum observed value in the experiment. Using the slope at $B = B_{\rm sw}$ obtained from the experiment, one finds $G'_{\rm sw} = \frac{dG_-}{dB}|_{B=B_{\rm sw}} = 2a(B_{\rm sw} - B_{\rm str})$, assuming $B_{\rm str} > B_{\rm sw}$. This results in $B_{\rm str} = B_{\rm sw} - \frac{G'_{\rm sw}}{2a}$. The parameter b is not used here, but can be obtained by matching G_- and G_{interp} at $B = B_{\rm sw}$. The method is illustrated in figure 5.7c. A similar analysis also holds for the down sweep $G_+(B)$. With this method, we find a lower bound for $B_{\rm str} \approx 80$ mT. We note that although we can directly determine $B_{\rm str}$ in this method, the limitation of not knowing

the MC beyond B_{sw} still persists. Therefore, the calculated B_{str} is still a lower bound estimate. More direct measurements are necessary to exactly determine B_{str} as discussed in section 5.8.

5.6. Control Experiment

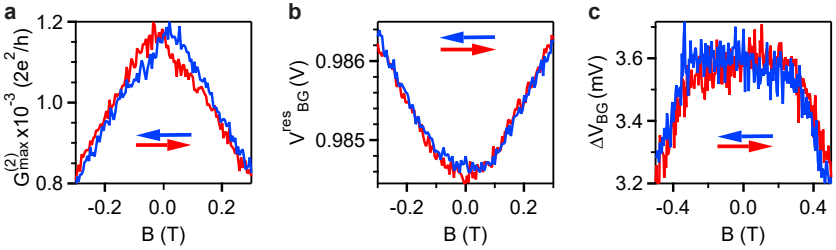

Figure 5.8. Control Experiment. **a** $G^{(2)}_{max}$, **b** resonance position, and **c** resonance width as a function of B for the up (red) and down (blue) sweep of a QD resonance, at $V_{SD} = 0$, in the NW segment $S - D_2$.

As a control experiment, we measure the magnetoconductance $G^{(2)}$ as a function of V_{BG} at a series of external magnetic field B for a resonance in QD2. We expect negligible hysteresis as QD2 is located far away from the FSGs. To illustrate this, we extract the maximum conductance $G^{(2)}_{max}$, peak position and FWHM of the resonance at each B value in Fig. 5.8, similar to section 5.4. The extracted $G^{(2)}_{max}$ shows a small hysteresis and no abrupt switching in both the up and down sweep. The peak position and FWHM also exhibit similar behavior. We further note that we do not observe any hysteresis in the magnetoconductance for QD devices without any FSGs nearby. The study of such a device is not presented in this thesis. A similar analysis using the method of interpolation for this QD2 resonance results in $B_{str} \leq 5\,\text{mT}$. This value is consistent with the much larger distance $\sim 800\,\text{nm}$ of QD2 from the FSGs.

5.7. Cobalt ferromagnetic Sidegates

Although we obtain $B_{str} \sim 80\,\text{mT}$ with permalloy FSGs, a stronger stray magnetic field is ideal for larger Zeeman splitting of the QD resonances. One of the approaches for improving the stray field is to use different ferromagnetic materials such as cobalt (Co). In general, cobalt has a higher saturation magnetization than permalloy and is a harder magnet making it less susceptible to changes in the geometry of the magnet. Therefore, we expect a larger B_{str}

and B_{sw} for Co than Py. However, the magnetocrystalline anisotropy in Co is large due to which the magnetization has a built-in preferred orientation at zero external magnetic field. The domain structures and stray field can be observed in the X-ray magnetic circular dichroism (XMCD) and magnetic force microscopy (MFM) measurements as shown in Fig. 5.9 [70, 195].

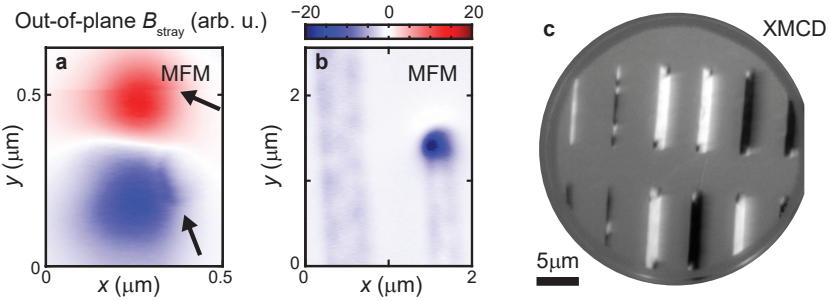

Figure 5.9. Stray field imaging of cobalt (Co) FSG strips. a,b Magnetic force microscopy of stray magnetic fields generated by a Co FSG and a single Co strip. **c** Domain structure of Co strips measured by X-ray magnetic circular dichroism (XMCD). All the characterizations were carried out by Dr. Gabor Fabian, Dr. Andreas Baumgartner, Dr. Simon Zihlmann and Dr. Peter Makk in the Hug lab at EMPA, Switzerland (MFM) and the SIM beamline at Paul Scherrer Institut, Switzerland (XMCD) [70, 195].

Similar to permalloy, we find a stray field pattern where the tips of the two FSGs have opposite polarity and the bulk displays minimal stray field strength in MFM measurements. However, the magnetization distribution along the FSG axes displayed some discrepancies in the XMCD measurements. The domain structures at the FSG tips showed more pronounced non-uniform magnetization compared to similar permalloy strips indicating the formation of closure domains, as shown in Fig. 5.9c.

We then fabricate samples with cobalt ferromagnetic split-gates as shown in Fig. 5.10a. The differential conductance G as a function of gate V_{G1} is measured at a series of external magnetic field B for a QD resonance, as shown in Fig. 5.10b. The backgate is kept at a constant voltage of $V_{BG} = 0.66\,\text{mV}$ and $V_{G2} = 0$. Similar to the Py device, we find that the colormaps are clearly hysteretic for the increasing (red arrow) and decreasing (blue arrow) field sweep directions and display a strong dependence on B. The extracted maximum conductance G_{max} from Fig. 5.10b is shown in Fig. 5.10c. G_{max} is hysteretic and mirror symmetric around $B = 0$. Similar to the permalloy device, we expect a smooth non-monotonous magnetoconductance with a abrupt con-

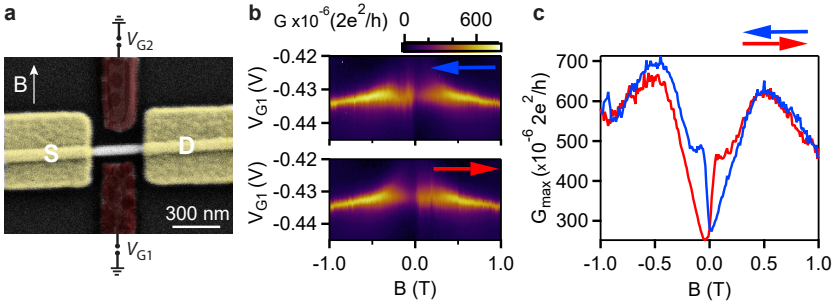

Figure 5.10. Cobalt device and magnetoconductance experiments. a False color SEM image of the investigated Co FSG device. **b** $G^{(2}$ as a function of external magnetic field B and gate voltage V_{G2} for the up (red) and down (blue) sweep of a QD resonance, with $V_{SD} = 0$, in the NW segment $S - D_2$. **c** $G^{(2)}_{max}$ vs B for the up and down sweep extracted from **b**.

ductance change at the switching field B_{sw}. However, the extracted G_{max} displays a smooth change rather than a sharp switching. For the up sweep (red arrow), G_{max} first increases linearly with increasing B, followed by a peak at around $B = -500\,\text{mT}$ and a decrease till roughly $B \approx 0$. As B changes sign at 0 T, G_{max} smoothly increases till $\sim 80\,\text{mT}$ and subsequently converges with the curve measured in the opposite direction at higher B values.

The smooth change of G_{max} on a large field scale around $B = 0$ can be attributed to the magnetocrystalline anisotropy of the Co strips. As observed in the XMCD measurements, the domains at the tip of the Co strips displayed non-uniform magnetization at $B = 0$. As we sweep B towards zero in our measurements, these domains align along the preferred built-in direction to minimize the total free energy. The crystalline anisotropy dominates over the shape anisotropy in such Co strips resulting in a smooth rotation of the domains rather than a sudden reversal in the magnetization orientation. This is reflected as a smooth change in the MC around $B = 0$. These results demonstrate that although we observe clear hysteresis with Co FSGs on a larger field scale, the less controlled domain structure of the Co FSG tips makes it harder to observe the desired MC features compared to permalloy. Therefore, we use permalloy as the suitable material for FSG fabrication in all the subsequent devices in this thesis.

5.8. Discussion and Outlook

One of the main disadvantages in this experiment is the inability to directly determine B_{str}. Although the stray field from a nearby micromagnet has been measured in a DQD system [197, 198], the most straightforward way in our experiment is to perform electron spin resonance (ESR) measurements [199]. For a single QD with FSG device, we apply a varying magnetic field to drive the electron spins using a strip line with an ac current. At the ferromagnetic resonance condition, we should observe a dip in the reflected signal strength, examined by a readout resonator coupled to the QD-FSG device.

In addition, larger B_{str} is ideal for larger Zeeman splitting of the QD states. This can be optimized by reducing the FSG gap with optimized fabrication procedures or smaller diameter NWs. In addition, precise location of the QD, using either in-situ grown InP tunnel barriers [83, 86] or crystal-phase engineered tunnel barriers [72, 166] in an InAs NW, is desired to ensure optimized and homogeneous local stray magnetic fields.

In conclusion, we presented proof-of-principle magnetoconductance (MC) experiments for a single quantum dot (QD) with ferromagnetic split gates (FSGs). We characterized the switching (coercive) field of the FSG and determined a stray magnetic field of $\sim 80\,\mathrm{mT}$ in the FSG gap from the hysteretic MC of the QD resonances. In addition, we estimated a negligible stray field far away from the FSGs. Our technique demonstrates a new approach towards controlling electron spin in QDs in close proximity to superconducting elements.

6 A Double Quantum Dot Spin Valve

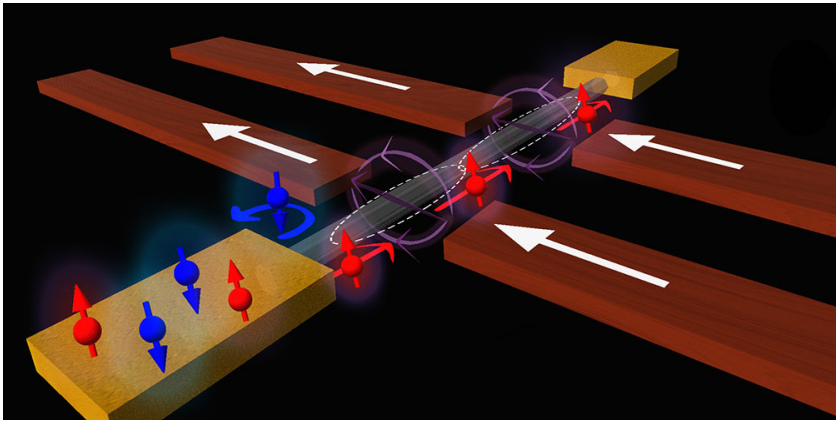

In this chapter, we investigate electron transport through two Zeeman-split QDs in series, spin polarized by stray magnetic fields from local FSGs, in a double quantum dot spin valve device. We determine the switching field of the two FSGs and demonstrate the accessibility of two parallel and two antiparallel magnetization states at zero external magnetic field in our device. In tunneling magnetoresistance (TMR) experiments, we find a large TMR signal electrically tunable from +80% to −90%, which also results in a large gate tunable QD spin polarizations up to ±80%. Such versatile QD-FSG spin filters offer an alternative route for spin injection and detection in semiconducting nanostructures.[1]

[1] This chapter has been published in a similar form in [105].

6.1. Introduction

Spin injection and detection are two of the most fundamental processes in semiconductor spintronics,[11–13, 200–202] for example for quantum spintronic devices and spin-based information processing,[27, 203, 204] or to determine and control spin states in quantum physics.[205–207] Significant efforts are dedicated to improve the efficiencies of these processes in a variety of material platforms and physical phenomena.[24, 208–211] However, a reliable and versatile technique to measure the spin degree of freedom remains elusive, especially for superconductor hybrid devices, where spin phenomena are crucial, for example in entanglement generation in solids,[52, 59] or demonstrating topological superconductivity in Majorana type devices.[183] Such experiments require highly efficient and gate-tunable spin injectors and detectors in-situ of an active device. Most of these concepts rely on electrical contacts to ferromagnetic reservoirs,[13] or on magnetic tunnel barriers,[212] with significant obstacles[213] like a low polarization ($20 - 40\%$),[110] the magneto-Coulomb effect,[96, 214] the conductivity mismatch at the metallic ferromagnet-semiconductor interface[111] or large global external magnetic fields,[203, 215] suppressing the superconductivity and changing significantly the bandstructure. All these effects are particularly challenging in sub-micrometer scaled electronic devices.

6.2. Device Concept and Characterization

Here we provide an alternative route for spin injection and detection in semiconductor devices, compatible with superconductors in close proximity, using quantum dots (QDs) *without* ferromagnetic contacts. As illustrated in figure 6.2a, the spin degeneracy of a QD state can be lifted by a magnetic field, resulting in a spin polarization at the Fermi energy E_F of

$$P = \frac{D_\uparrow(E_\mathrm{F}) - D_\downarrow(E_\mathrm{F})}{D_\uparrow(E_\mathrm{F}) + D_\downarrow(E_\mathrm{F})}, \tag{6.1}$$

with D_σ the QD transmission density of states (t-DoS) for spin state $\sigma \in \{\uparrow, \downarrow\}$ at E_F. This spin-dependent transmission directly results in a spin-polarized current through the QD. In practice, a single QD can be spin polarized individually by placing it in the narrow gap in a long strip of a ferromagnetic material, which we term ferromagnetic split-gate (FSG). The FSG generates a stray field B_str at the QD position in the direction given by its magnetization, either parallel or antiparallel to its long axis[192] and can also be used for electrical gating. The FSG magnetization, and with it B_str, can be inverted at a characteristic external switching field B_sw, determined by the FSG width in the device design.[106, 114]

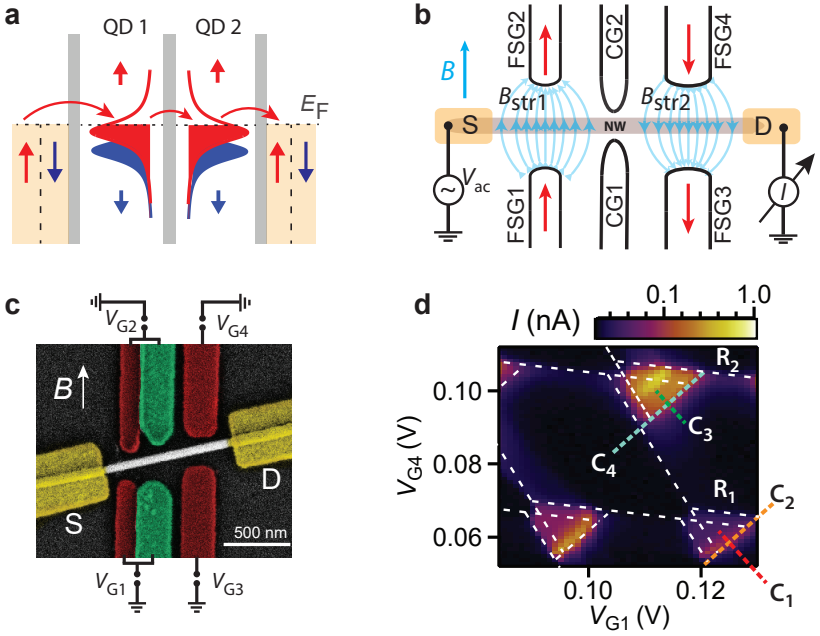

Figure 6.2. Double quantum dot spin valve concept and device. a,b, Energy diagram (**a**) and schematic (**b**) of a DQD spin valve. **c,** False color SEM image of the investigated InAs NW device. **d,** Current I as a function of gate voltages V_{G1} and V_{G4}, at $V_{SD} = +1$ mV, showing bias triangles characteristic for weakly coupled DQDs.

Similar to conventional spin valves with two ferromagnetic contacts with Stoner split bands, we combine two QD-FSG elements with Zeeman split QD states in series to form a double QD-spin valve (DQD-SV). In the first QD-FSG unit (spin-injector), a spin polarized tunnel current is generated, which is then detected at a different position by a second QD-FSG unit (spin detector). This concept is illustrated in figure 6.2a: electrons in state σ from the *unpolarized* electrical contacts tunnel sequentially through the two QDs with a probability that depends on the FSG states of *both* QDs, to first order resulting in the respective current $I_\sigma \propto D_\sigma^{(1)} D_\sigma^{(2)}$. Following typical tunneling magnetoresistance (TMR) experiments,[13] we show that in such nano structures both mutually parallel (p) and both anti-parallel (ap) magnetization states of the two FSGs can be accessed at zero external magnetic field, $B = 0$, and reoriented by cycling B. The individual QD polarizations and TMR signals

can be continuously electrically tuned up to values close to the theoretical limits. In contrast to previously employed very large polarizing external magnetic fields,[215–217] the stray and external magnetic fields required for such optimizations are small enough and decay over short enough length scales, to be compatible with various spin injection and detection experiments, for example with superconducting components in Cooper pair splitters[52, 59] for electron spin correlation measurements,[140] or to demonstrate equal spin Andreev reflection[183] at Majorana type superconducting bound states.[71, 218, 219]

A schematic of a DQD-SV and a scanning electron microscopy (SEM) image of the investigated InAs nanowire (NW) device are shown in figures 6.2b and 6.2c, respectively. The FSGs are long Permalloy (Py) strips fabricated by electron beam lithography with a narrow gap at the NW position, forming the split-gate geometry. The strip widths are 120 nm and 230 nm, respectively, determining the corresponding switching and stray fields, which can be extracted from independent experiments as demonstrated in Appendix B.1 and Chapter 5, respectively. The electrical contacts at the NW ends are made of titanium/gold with a split central gate (CG) to electrically form the two QDs fabricated in the same step. One part of the narrower FSG and the CG gate are electrically connected accidentally and are tuned in unison, which we refer to as "gate 1" (G1) and "gate 2" (G2), while the other FSGs are labeled individually (see figure 6.2c). The DC current I resulting from a bias voltage V_{SD} and the differential conductance $G = \mathrm{d}I/\mathrm{d}V_{\mathrm{SD}}$, were measured simultaneously using standard DC and lock-in techniques ($V_{\mathrm{ac}} = 10\,\mu\mathrm{V}$), at a base temperature of $\sim 50\,\mathrm{mK}$.

In figure 6.2d, we plot I flowing through the DQD-SV at $V_{\mathrm{SD}} = 1\,\mathrm{mV}$, as a function of V_{G1} and V_{G4}. This map shows several bias triangles characteristic for a weakly coupled DQD. These triangles originate from one resonance of each QD aligning in energy within the bias transport window.[97] This allows us to independently extract most of the single QD parameters used for modelling later, e.g. the lever arms of each gate to each QD (see Appendix B.2). We now discuss various types of TMR experiments for two resonances, in figures 6.3 and 6.4, respectively, while data for a third resonance are discussed in Appendix B.5.

6.3. Tunneling Magnetoresistance at $B = 0$

We first demonstrate the principle of a TMR experiment and show that all FSG magnetization states can be accessed at $B = 0$. Figure 6.3a shows a high resolution bias triangle of a resonance (not shown in figure 6.2d) at $V_{\mathrm{SD}} = 500\,\mu\mathrm{V}$. Our typical TMR experiment consists of first choosing a specific trace for the two gate voltages, here by sweeping V_{G1} and keeping V_{G4} constant, as indicated by the red arrow, such that no excited states are involved in the transport

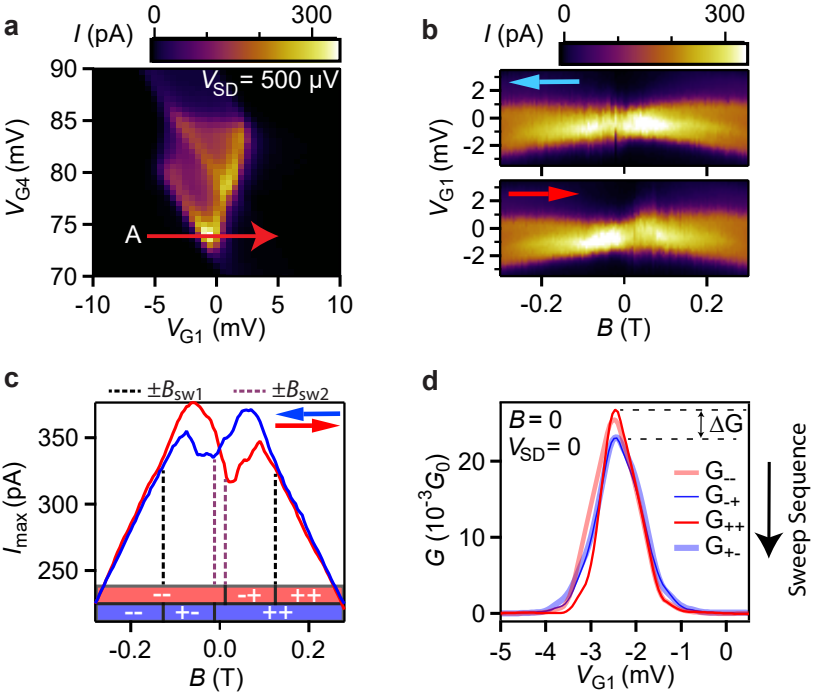

Figure 6.3. FSG magnetization states and TMR at $B = 0$. a, Bias triangles at $V_{SD} = 500\,\mu V$. The red arrow specifies the cross-section A investigated in **b**. **b,** Up (red arrow) and down sweep (blue arrow) maps of I as a function of B and V_{G1}, measured along cross section A in figure 6.3a. **c,** Current maximum I_{max} vs B, extracted from figure 6.3b, for the up (red) and down (blue) sweep. The magnetization configurations are indicated by $i, j \in \{+, -\}$ **d,** G as a function of V_{G1} for all four magnetization states at $B = 0$ and $V_{SD} = 0$, showing a supression ΔG for the anti-parallel states relative to the parallel magnetization configurations. The arrow indicates the sequence of the experiments.

process. We then measure I as a function of V_{G1} at a series of external magnetic fields, B, applied in parallel to the FSG axes, which results in relatively abrupt switchings of the FSG magnetizations (details in Appendix B.1). Such a map for the trace in figure 6.3a is shown in figure 6.3b for decreasing and increasing magnetic fields, as indicated by the blue and red arrows, respectively, each starting at fields much higher (+0.5 T), or lower (−0.5 T) than

shown, to ensure the formation of only a single magnetic domain along the FSG axes. These maps show a clear hysteresis with a strong dependence on B and the sweep direction. To demonstrate this more explicitly, we extract the position, width (both discussed in Appendix B.3) and the maximum current $I_{\max}$ at each B value. $I_{\max}$ extracted from figure 6.3b is plotted in figure 6.3c for decreasing (blue) and increasing B (red).

In the up-sweep, $I_{\max}$ first increases roughly linearly with increasing B, followed by a maximum at $B \approx -55\,\mathrm{mT}$ and a decrease around $B = 0$. At small positive B, $I_{\max}$ becomes flatter, followed by a small maximum at $B \approx 85\,\mathrm{mT}$, and a roughly linear decrease towards more positive B. The down-sweep can be described similarly as the up-sweep, but mirrored at $B \approx 0$ leading to a clear hysteresis. This hysteresis can be understood qualitatively by considering a smooth non-monotonous MR of the DQD that changes abruptly with the reorientation of the FSG magnetizations. In the up-sweep, at $B > B_{\mathrm{sw2}} \approx 5\,\mathrm{mT}$ the wider FSG is reoriented parallel to the now positive B, and the two FSG magnetizations become anti-parallel (ap). The FSGs become magnetized in parallel again for $B > B_{\mathrm{sw1}} \approx 140\,\mathrm{mT}$, when the narrower FSG is also inverted (details are given in Appendix B.1). These configurations are shown schematically at the bottom of figure 6.3c for the down (blue) and the up-sweep (red).

As a first quantitative measure for the TMR effect, we use the maximum current values at $B = -55\,\mathrm{mT}$, using the maximum value of $I_{\max}$ in the p state, and the value in the opposite sweep direction at the same field in the ap state. We define TMR as

$$\mathrm{TMR} = \frac{I_{\mathrm{p}} - I_{\mathrm{ap}}}{I_{\mathrm{p}} + I_{\mathrm{ap}}} \tag{6.2}$$

which results in TMR $\approx 6\%$ at $V_{\mathrm{SD}} = 500\,\mu\mathrm{V}$ and $B = -55\,\mathrm{mT}$.

To explicitly demonstrate that all four magnetization states (two p and two ap) are accessible at $B = 0$, we measure the differential conductance G at $V_{\mathrm{SD}} = 0$ as a function of V_{G1} for each FSG magnetization state. The direction of the stray fields B_{str1} and B_{str2} can be reversed individually by sweeping B beyond the characteristic FSG switching fields. The exact sequence of B sweeps for each measurement at $B = 0$ are as follow:

1. (-,-): Sweep the external magnetic field to $B = -500\,\mathrm{mT} << -B_{\mathrm{sw1}}$ in order to form a single magnetic domain along the FSG axis, followed by a sweep back to $B = 0$ to obtain the magnetization state $(-,-)$.

2. (-,+): Continue sweeping to $B = +40\,\mathrm{mT} > B_{\mathrm{sw2}}$ (but $< B_{\mathrm{sw1}}$) followed by a sweep back to $B = 0$ to obtain the magnetization state $(-,+)$.

3. (+,+): Sweep to $B = +500\,\mathrm{mT} >> B_{\mathrm{sw1}}$ to get a single magnetic domain along the $+B$ direction, followed by a sweep back to $B = 0$ to obtain $(+,+)$.

4. (+,-): Continue sweeping to $B = -40\,\mathrm{mT} < -B_{\mathrm{sw2}}$ (but $> -B_{\mathrm{sw1}}$) followed by a sweep back to $B = 0$ to obtain $(+,-)$.

We note that in the used sequence, p is followed by ap and vice versa. The gate sweeps for the four magnetization states at $B = 0$ are plotted in figure 6.3d. All curves show a maximum at the same gate voltage, which corresponds to a weakly spin split energy level of each QD ($\Gamma > g\mu_B B$) being aligned with the Fermi energy. The conductance is gradually reduced to zero if the QD levels are detuned by V_{G1}. We find very similar maximum conductances for the same relative magnetization orientations and a clear suppression in G for both ap states with respect to the two p states, yielding $\mathrm{TMR} = \frac{\Delta G}{G_{\mathrm{P}}+G_{\mathrm{AP}}} \approx 7\%$, similar to the value obtained at a larger bias and a small finite B.

The DQD-SV experiment can be reproduced quantitatively using a very simple model, which also allows us to estimate the QD polarizations: we assume that the current is given by elastic tunneling in two independent spin channels,[112] which yields for a constant weak inter-dot coupling T_{12} and the magnetization orientations $i, j \in \{+,-\}$ along the FSG axes,

$$I^{(ij)} = I_{\uparrow}^{(ij)} + I_{\downarrow}^{(ij)} = \frac{e}{h} \sum_{\sigma} \int_{-\infty}^{\infty} T_{12} D_{1\sigma}^{(i)}(E) D_{2\sigma}^{(j)}(E) \\ [f(E-\mu_{\mathrm{S}}) - f(E-\mu_{\mathrm{D}})]dE, \tag{6.3}$$

where $D_{\beta\sigma}(E)$ denotes the spin dependent t-DoS in dot $\beta \in \{1,2\}$ and $\sigma \in \{\uparrow, \downarrow\}$ the spin orientation; $f(E) = 1/(1+e^{E/(k_B T)})$ is the Fermi-Dirac distribution function and $\mu_{\mathrm{S,D}}$ the electrochemical potential in the source and drain contacts, respectively. To start with, we assume a small bias (linear regime) to obtain the conductance, as in the experiments. Since the Zeeman shift is opposite, but of the same magnitude for opposite spins, the t-DoS of each QD obeys the identity $D_{\sigma}^{-}(-B, E_{\mathrm{F}}) = D_{-\sigma}^{+}(+B, E_{\mathrm{F}})$ due to time-reversal symmetry. At $B = 0$, this reduces to $D_{\sigma}^{-}(E_{\mathrm{F}}) = D_{-\sigma}^{+}(E_{\mathrm{F}})$, which yields, using the definition of the QD polarizations in equation (1),

$$\mathrm{TMR} = \frac{I_{\mathrm{p}} - I_{\mathrm{ap}}}{I_{\mathrm{p}} + I_{\mathrm{ap}}} = P_1 P_2 \approx P^2. \tag{6.4}$$

In the last step we assume that both QD polarizations are identical, which results in $P \approx 27\%$ on resonance at $B = 0$. We stress that this expression for the TMR signal only holds at $B = 0$ because of the non-constant QD t-DoS, in contrast to devices with ferromagnetic contacts, for which it holds also at finite external fields, limited only by the correlation energy of the band structure.

6.4. Tunneling Magnetoresistance at finite B

The non-constant t-DoS of the QDs allows us to go beyond the standard experiments, enabling us to optimize and tune the TMR signals magnetically as well as electrically. To demonstrate this, we investigate cross section C_1 pointed out in figure 6.2d, for which we again plot I as a function of B and V_{G1} at $V_{SD} = 10\mu V$. Figure 6.4a shows the up and down sweeps, which again show a clear hysteresis, prominently visible in figure 6.4b, where we plot I_{max} as a function of B for the up and down sweeps (width and position are discussed in Appendix B.3). These curves show qualitatively similar characteristics as discussed for figure 6.3c. From the current maximum, we find a TMR signal of $\sim 29\%$ at $B = 0$ and estimate the individual QD spin polarizations as $P \approx 53\%$ using equation (4). These values are larger than for the previously discussed resonance, mostly due to a smaller resonance width.

We now exploit the non-constant t-DOS to optmize the TMR signal. First, we apply a small homogenous external field of $\pm 40\,\mathrm{mT}$, which is small enough to still access all four FSG magnetization states ($B < B_{sw1}$) and compatible with a wide variety of applications, for example with many superconducting circuit elements. We measure I along cross section C_2 indicated in figure 6.2d, which is chosen on the resonance maximum along the base of the bias triangle (see Appendix B.4) so that a shift in the resonance energies is negligible.

Figure 6.4c shows the four $I(V_{G1})$ curves along C_2 for the four FSG magnetization states (i, j) (V_{G4} is the same for each chosen B). The curve for the parallel $(-,-)$ [blue] and the anti-parallel configuration $(+,-)$ [grey] were measured at $B = -40\,\mathrm{mT}$, while the ones for $(+,+)$ [purple] and (-,+) [black] were measured at $B = +40$ mT. The exact sequence of B sweeps for the measurements at $B = \pm 40\,\mathrm{mT}$ are as follow:

1. (-,-): Sweep the external magnetic field to $B = -500\,\mathrm{mT}$ in order to form a single magnetic domain along the FSG axis, followed by a sweep back to $B = -40\,\mathrm{mT}$ to obtain the magnetization state $(-,-)$ at $B = -40\,\mathrm{mT}$.

2. (-,+): Sweep to $B = +40\,\mathrm{mT}$ to obtain the magnetization state $(-,+)$ at $B = +40\,\mathrm{mT}$.

3. (+,+): Continue sweeping to $B = +500\,\mathrm{mT}$ to get a single magnetic domain along the $+B$ direction, followed by a sweep back to $B = +40\,\mathrm{mT}$ to obtain the $(+,+)$ at $B = +40\,\mathrm{mT}$.

4. (+,-): Continue sweeping to $B = -40\,\mathrm{mT}$ to obtain $(+,-)$ at $B = -40\,\mathrm{mT}$.

We find that the maximum current and lineshape for both anti-parallel configurations are almost identical, while the two parallel ones slightly differ.

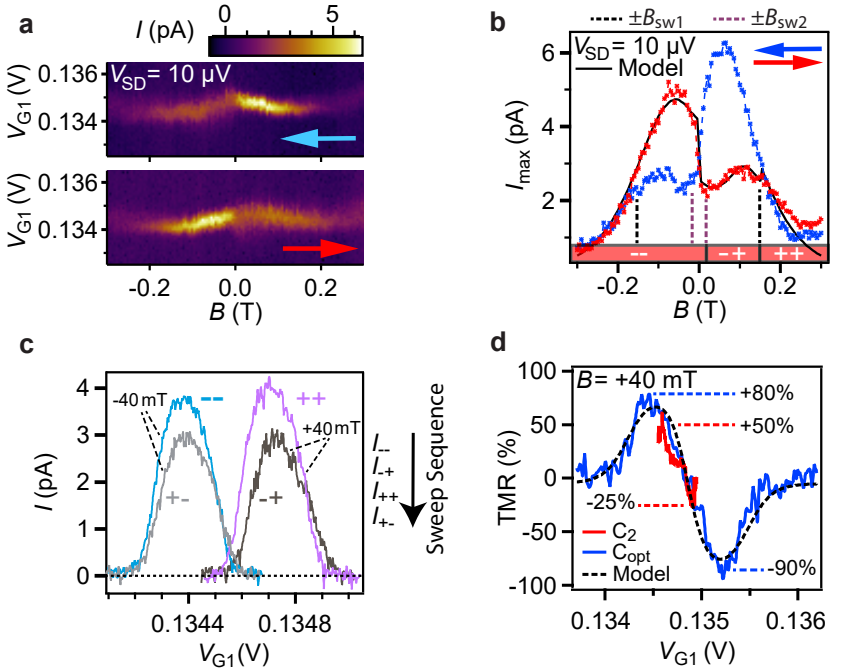

Figure 6.4. Optimized TMR at $B = \pm 40$ mT. a, Maps of I as a function of B and V_{G1} for the up (red arrow) and down sweep (blue arrow), for the cross section C_1 (see figure 6.3d) at $V_{SD} = 10\,\mu$V. **b,** Maximum current I_{max} as a function of B for the up (red) and down sweep (blue) extracted from figure 6.4a. **c,** I along cross section C_1 (see figure 6.2d) paramterized by V_{G1} for all four magnetization states, with the $(-,-)$ and $(+,-)$ configurations measured at $B = -40$ mT, and the $(+,+)$ and $(-,+)$ configurations at $B = +40$ mT. **d,** TMR for magnetization states $(+,+)$ and $(-,+)$ at $B = +40$ mT for cross sections C_2 (red) and C_{opt} in figure 6.5a (blue). The black dashed line shows the TMR extracted from the model for cross section C_{opt} (shown in figure 6.5a), with the parameters obtained from fits to the data in figure 6.4b.

Most importantly, the anti-parallel curves are reduced in amplitude by $\sim 25\%$ with respect to the parallel ones. We note that for this cross section, the maximum occurs at the same V_{G1} value for both pairs of curves in figure 6.4c.

For any given V_{G1} and B, we now calculate the TMR signal using equation 6.2. As an example, this is plotted for the states $(+,+)$ and $(-,+)$ in figure 6.4d (red curve), which shows that the TMR signal is continuously gate

tunable roughly between +50% and −25%. This TMR signal can be improved significantly by exploiting the small, field-induced shifts in the resonance positions. To achieve this, we plot TMR $= (I_{++} - I_{-+})/(I_{++} + I_{-+})$ at $B = 40\,\mathrm{mT}$ as a function of V_{G1} and V_{G4} in figure 6.5a and find the optimal cross section labelled C_{opt}. In figure 6.4d, we plot TMR along C_{opt} which shows a continously gate tunable TMR with a well separated pronounced maximum and minimum TMR of +80% and −90%, respectively. These values are significantly larger than in most other systems.

6.5. Spin Polarization

We expect that the QD polarizations are also gate tunable to large values, but since an external field is applied, the above symmetry argument cannot be used for a simple estimate. We therefore resort to numerically evaluating the model introduced above. To do so, we define the total magnetic fields $B_{tot}^{(\beta)} = B + B_{str}^{(\beta)}$ at the two QD positions $\beta \in \{1, 2\}$, and use as the energy-dependent t-DoS of the QDs at energy E the Lorentzian $\mathcal{L}(E - E_{\beta\sigma}) = (\Gamma_\beta/2)^2/[(E - E_{\beta\sigma})^2 + (\Gamma_\beta/2)^2]$, centered at

$$E_{\beta\sigma} = E_\beta^{(0)} - e\alpha_\beta V_{g\beta} + \frac{1}{2}\sigma g_\beta \mu_B B_{tot}^{(\beta)}, \tag{6.5}$$

with $E_\beta^{(0)}$ an energy offset for states in dot β at zero gate voltages, g_β the corresponding electron g-factors and Γ_1 and Γ_2 the broadening parameters. The lever arms α_β are extracted independently from the bias triangles[2] and $V_{g\beta}$ are the applied gate voltages. The total current is then calculated using equation (6.3).

This model reproduces very well the experiments using a single set of parameters for a given resonance, all in the typical range found in literature. For example, we obtain I_{max} as a function of B, as plotted by the black curve in figure 6.4b for the up sweep, using $B_{str1} = 61(\pm 4)$ mT, $B_{str2} = 27(\pm 5)$ mT (estimated independently, see chapter 6) and the adjustable parameters $g_1 = 5.6$, $g_2 = 6.3$, $\Gamma_1 = 25\,\mu$eV and $\Gamma_2 = 15\,\mu$eV, $E_1^{(0)} \equiv 0$, $E_2^{(0)} = 8.1(\pm 0.3)\,\mu$eV, and an inter-dot tunnel coupling $T_{12} = 0.12$ adjusted to obtain the correct amplitude. The errors given in brackets indicate the range for a parameter that still gives satisfactory model curves. The same parameters also reproduce the TMR results, shown as an inset in figure 6.5a and the optimized TMR cross section C_5 shown in figure 6.4d (black dashed line). The same parameters also reproduce the width (Appendix B.3) and figure 6.4c. To reproduce the other investigated resonances, we use slightly different parameters, as summarized in Appendix B.5.

[2] we also include cross lever arms in the model without stating this explicitly for simplicity

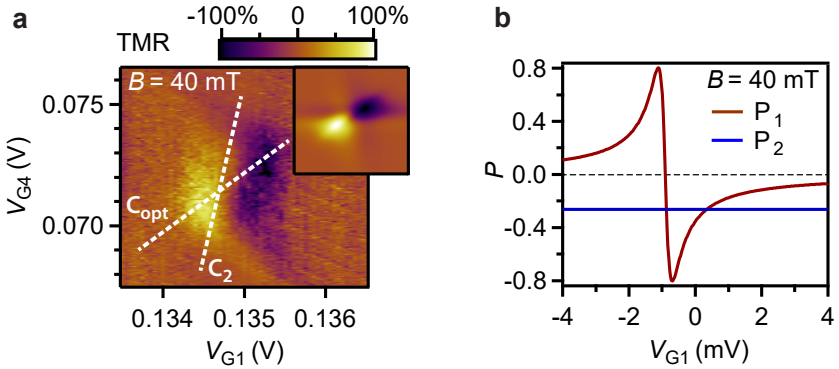

Figure 6.5. From TMR to spin polarization. a, Measured TMR as a function of V_{G1} and V_{G4} for the magnetization states $(+,+)$ and $(-,+)$ at $B = 40\,\mathrm{mT}$. The cross sections C_2 and C_{opt} are indicated by dashed lines. Inset: TMR from the model calculations with the parameters extracted from figure 6.4b . **b,** Spin polarization of QD1 (P_1) and QD2 (P_2) as a function of V_{G1} and constant V_{G4} from the model at $B = 40\,\mathrm{mT}$, showing a large gate tunability of P_1 from -0.8 to $+0.8$.

In the model it is straight forward to extract the spin polarizations, e.g. P_1 for QD1 as a function of V_{G1} at $B = 40\,\mathrm{mT}$, which is plotted in figure 6.5b, with $P_2 \approx 27\%$ for QD2, being independent of V_{G1}. P_1 can be gate tuned over a large range, with a maximum absolute value of $P_1 \approx 80\%$, and a zero-field value of $\approx 59\%$. This analysis demonstrates that the DQD-SV is a highly tunable spin valve with one QD acting as a gate-tunable spin injector and the other as a detector, such that transport through the DQD can be electrically tuned from predominantly spin down electrons to spin up electrons, depending on the orientation of B_{str} and B. The large gate-tunability of the QD spin polarizations originates from the resonance widths being of similar magnitude as the Zeeman splitting, $\Gamma_1 + \Gamma_2 \sim g\mu B_{tot}$. Increasing the QD life time in the model by only a factor of two, keeping all other parameters the same, we find even stronger polarizations, up to 91%, thus almost reaching unity. Such sharper line shapes can be obtained with in situ grown InP tunnel barrier[83, 220, 221] or by crystal phase engineered barriers in InAs NWs.[72, 166] In addition, the QD polarization can be enhanced by stronger B_{str}, either by reducing the FSG gap, e.g. using smaller diameter NWs, or by using other ferromagnetic materials.

6.6. Discussion and Conclusion

In conclusion, we have demonstrated a DQD spin valve in an InAs NW with ferromagnetic split gates that results in a tunneling magnetoresistance electrically tunable between +80% and −90%. Using a simple resonant tunneling model, we extract gate and B field tunable QD spin polarizations up to $\sim \pm 80\%$, with the possibility of even larger values, up to unity. This large benchmark value and the spatially localized stray fields are promising for efficient spin injection, detection and correlation experiments in a large variety of devices. We note that our concept is very general and can be applied to any device region with a non-constant transmission $T(E)$ and a finite g-factor. Especially the small external fields resulting in such large efficiences are compatible with many superconducting contacts in close proximity,[3] so that the QD-FSG units are ideally suited as spin injectors and detectors in nanoelectronic devices, for example to investigate spin orbit interactions [222], to perform spin correlation measurements and electronic Bell tests in a Cooper pair splitter,[140] or to demonstrate equal spin Andreev reflection at Majorana zero modes.[183] In addition, a single QD-FSG unit could also prove useful for the initialization and read-out of spin qubits,[179, 223] while arrays of FSG units are expected to result in a variety of novel phenomena, such as magnetic superlattices,[224] magnetic periodic potentials and in synthetic and externally controllable spin orbit interaction.[190, 225–227]

[3] see Chapter 5 for an experimental estimate of B_{str} away from the FSGs.

7 Spin readout in a Cooper pair splitter

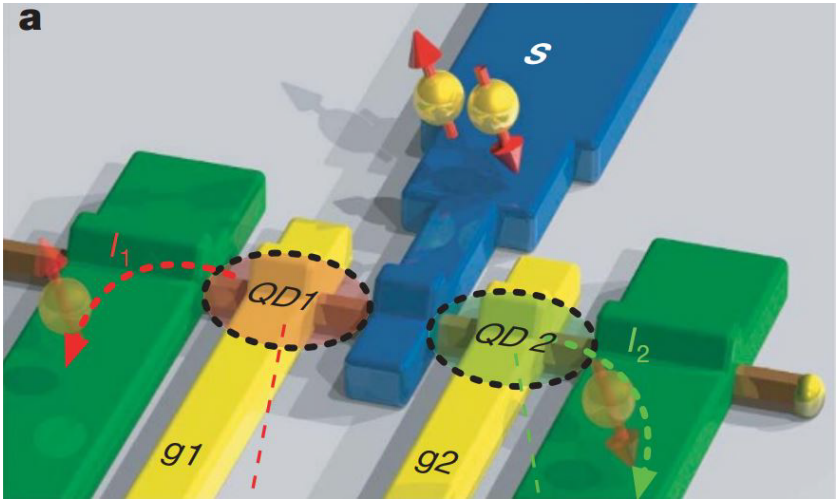

In this chapter, we perform spin readout measurements in a Cooper pair splitter device using the efficient spin detection technique in chapter 6 to investigate correlations between the spin currents in the CPS device. We demonstrate the coexistence of superconductivity and stray magnetic fields at close proximity in our device. In addition, the non-local CPS conductance for the four FSG magnetization states showed suppressed conductance for parallel magnetization states with respect to antiparallel states, consistent with the interpretation and calculation of spin cross anti-correlation for the spin singlet CPS ground state.[1]

[1] The image showing a Cooper pair splitter device was adapted from Ref. [52].

7.1. Introduction

Non-local correlations between two distant quantum systems is an important fundamental property in quantum mechanics [228]. Although experimental investigation of such non-local correlations have been demonstrated with entangled photons long back [229], it had proven quite difficult to investigate such phenomenon with spin-1/2 electrons in a well-controlled manner. Recently, Cooper pair splitter (CPS) devices were demonstrated as an on-chip source of entangled electrons, where the spin-singlet Cooper pairs were split into two different quantum dots (QDs) via crossed Andreev reflection (CAR) [118]. This phenomenon, known as Cooper pair splitting (CPS), has been successfully demonstrated in various systems, such as InAs NWs [52–57], carbon nanotubes (CNTS) [58, 59] and graphene [60, 61], by investigating the non local correlations in current [52, 59] as well as charge noise [56]. In such devices, the conductance cross correlation $corr_G = \langle dG_1 * dG_2 \rangle$, where $dG_{1,2}$ is the increase in conductance due to CPS, is expected to be positive, i.e. both arms show a simultaneous increase in conductance, while the spin cross correlation $corr_S = \langle \sigma_{z1} * \sigma_{z2} \rangle$ is expected to be negative due to the electrons in a Cooper pair being spin singlet.

However, a proof of spin correlation is still missing. We expect a strong spin correlation between the electrons ejected into the two arms of a CPS device [62–64]. Such spin sensitive measurements require an efficient spin filtering and readout technique of the split electrons. One approach to achieve a spin filter is to Zeeman split the QD states of a CPS device using an external magnetic field. However, such an approach is limited by the maximum applicable external magnetic field in close proximity to a superconductor as well as the need of highly efficient spin detectors to detect small correlation signals. Such problems can be circumvented by the highly efficient spin detection technique demonstrated in chapter 6 using local stray magnetic fields.

In this chapter, we demonstrate a first experiment towards spin correlation measurements of Cooper pair electrons by combining ferromagnetic split gates (FSGs) with a CPS device. Electrons in a Cooper pair are spin singlets, for which we expect full negative correlation (or anti-correlation) between the spin signals of the two QDs. We use non-ideal partially polarized quantum dots as spin detectors to investigate CPS conductances for the four magnetization states given by the FSGs. As the main result of this chapter, we then demonstrate CPS in this device, with amplitudes that depend on the orientation of both FSG magnetizations, demonstrating non-locality not only in the charge current, but also in the spin signal. In addition, we determine the superconducting gap by bias spectroscopy and demonstrate the simultaneous coexistence of superconductivity and B_{str} at each QD in our device.

7.2. Device and Characterization

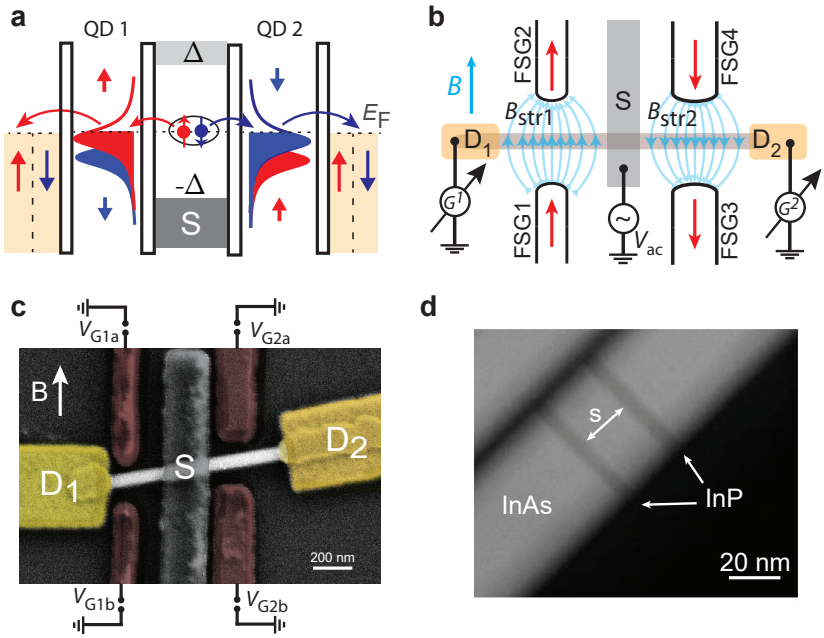

Figure 7.2. CPS-FSG concept and device a,b Energy diagram (**a**) and schematics (**b**) of a Cooper pair splitter with ferromagnetic split gates (CPS-FSG). **c** False color scanning electron microscope (SEM) image of the investigated InAs NW device. **d** Transmission electron microscope (TEM) image of an InAs/InP heterostructure NW, where two in-situ grown InP barriers of length $l_{1,2} \approx 5.5\,\text{nm}$ are separated by $s = 19\,\text{nm}$ of InAs. TEM image provided by Dr. Valentina Zannier, Pisa, Italy.

The spin selective CPS (SS-CPS) device is based on the tunneling of spin correlated electrons originating from CPS through the individual QDs, as illustrated in Fig. 7.2a. Similar to a typical Cooper pair splitter device discussed in section 2.3.3, we couple a superconductor to two individually electrically tunable QDs, each coupled further to a normal metal reservoir. In contrast to conventional CPS devices, we employ FSGs instead of normal metal side gates (NSGs) to tune the electrochemical potential of the QDs independently and, most importantly, to individually spin polarize the QD states. As discussed in chapter 6, this is obtained by the stray field B_{str} of the FSGs at the two

QD positions along the direction of its magnetization (Fig. 7.2b). This leads to a spin dependent transmission at the Fermi energy (similar to chapter 6) as B_{str} lifts the spin degeneracy of the QD states, which we describe by defining a spin polarization at the Fermi energy E_{F} given by:

$$P = \frac{D_{\uparrow}(E_{\mathrm{F}}) - D_{\downarrow}(E_{\mathrm{F}})}{D_{\uparrow}(E_{\mathrm{F}}) + D_{\downarrow}(E_{\mathrm{F}})}, \tag{7.1}$$

where D_{σ} is the QD transmission density of states (t-DoS) for spin state $\sigma \in \{\uparrow, \downarrow\}$ at E_{F}. Therefore, a split Cooper pair electron in spin state σ will tunnel through the QD with a probability that depends on the FSG magnetization state of the respective dot. The width of the FSGs for each QD is different, such that the FSG magnetization and the corresponding B_{str} can be independently reversed at the characteristic switching fields B_{sw} (see chapter 6 abd chapter 5).

A false color SEM image of the investigated CPS-FSG device is shown in Fig. 7.2c. An InAs NW of ∼40-45 nm diameter is contacted in the middle by a 200 nm wide titanium/aluminum (5 nm Ti/ 65 nm Al thick) superconducting contact (S). Two titanium/gold (5 nm Ti/ 45 nm Au thick) normal metal contacts (D_1 and D_2) are placed on opposite sides of S, such that they define a QD (QD1 and QD2) on each arm of the device. Both the QDs are electrically tuned using a global backgate (BG) and individually addressed by a pair of 30 nm thick Permalloy FSGs, which at the same time generate a stray magnetic field B_{str1} and B_{str2} at the respective QD positions. The width of the FSG pairs at QD1 and QD2 are $\sim 100\,\mathrm{nm}$ and $\sim 180\,\mathrm{nm}$ respectively, such that they reverse their magnetization at different switching fields B_{sw1} and B_{sw2} respectively. We apply a dc (V_{SD}) and an ac bias ($V_{\mathrm{ac}} = 10\,\mu\mathrm{V}$) to the S contact and simultaneously measure the differential conductance $G^{(1,2)} = \frac{dI_{1,2}}{dV}$ at the normal contacts D_1 and D_2 using standard lock-in techniques at a base temperature $T = 50\,\mathrm{mK}$.

The InAs NW used in this experiment contain two short indium phosphide (InP) segments directly beneath the 200 nm wide S contact with the purpose of reducing direct single electron tunneling through the NW. Such InP segments grown in-situ during the NW growth process serve as deterministic tunnel barriers in the InAs NW [153]. A transmission electron microscope (TEM) image of such an InAs/InP NW heterostructure is shown in Fig. 7.2d. The two InP segments have a width of $l_1, l_2 \approx 5.5\,\mathrm{nm}$, a separation of $s \approx 19\,\mathrm{nm}$ and are located at a distance of 440 nm from the Au catalyst particle.

We first determine transport characteristics of the individual elements by performing bias spectroscopy to determine the electronic transport properties of the device at zero external magnetic field, i.e. $B = 0$. Fig. 7.3a and Fig. 7.3b show colorscale plots of $G^{(1)}$ and $G^{(2)}$ respectively as a function of the applied bias voltage V_{SD} and gate voltages V_{G1a} and V_{G2a} respectively, from which we extract an addition energy of $E_{\mathrm{add},1} \approx 1.6\,\mathrm{meV}$ and $E_{\mathrm{add},2} \approx 2.5\,\mathrm{meV}$ for QD1

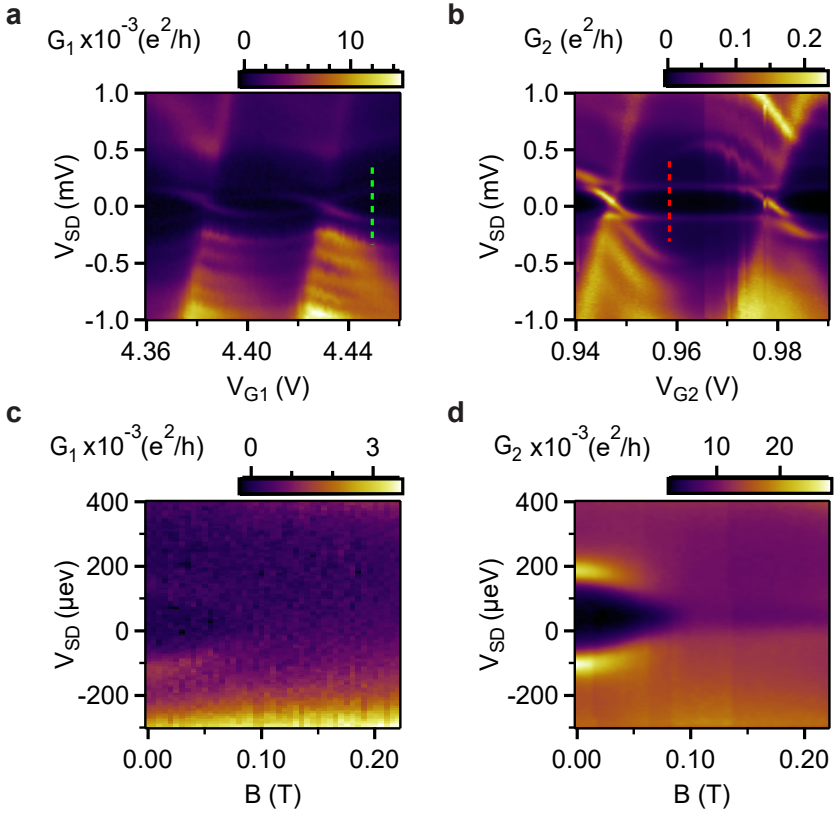

Figure 7.3. Bias spectroscopy. Differential conductance **(a)** $G^{(1)}$ and **(b)** $G^{(2)}$ as a function of bias voltage V_{SD} and gate voltages **(a)** V_{G1a} and **(b)** V_{G2a} for QD1 and QD2 respectively. **(c)** $G^{(1)}$ and **(d)** $G^{(2)}$ as a function of V_{SD} and the external magnetic field B for cross sections marked by green and red dashed line in **(a)** and **(b)** respectively, both consistently suggesting a critical magnetic field of $B_{\mathrm{c}} \sim 90\,\mathrm{mT}$ for the S-contact.

and QD2 respectively and a superconducting gap of $\Delta \sim 110\,\mu\mathrm{eV}$. The cross lever arms across the the S contact are one order of magnitude lower compared to the lever arm of a direct local FSG gate, which enables one to tune the QDs almost independently.

To characterize the superconductor, we now apply an external magnetic field B in-plane parallel to the FSG long axes. $G^{(1)}$ and $G^{(2)}$ as a function of

the applied V_{SD} and B, along the cross sections marked by the green dashed line in Fig. 7.3a and red dashed line in Fig. 7.3b, is plotted in Fig. 7.3c and Fig. 7.3d respectively. We observe that the superconducting gap is suppressed at a critical magnetic field of $B_c \sim 90\,\mathrm{mT}$. Therefore, B_{str1} and B_{str2} cannot be larger than B_c at the S position.

7.3. Magnetoconductance Measurements

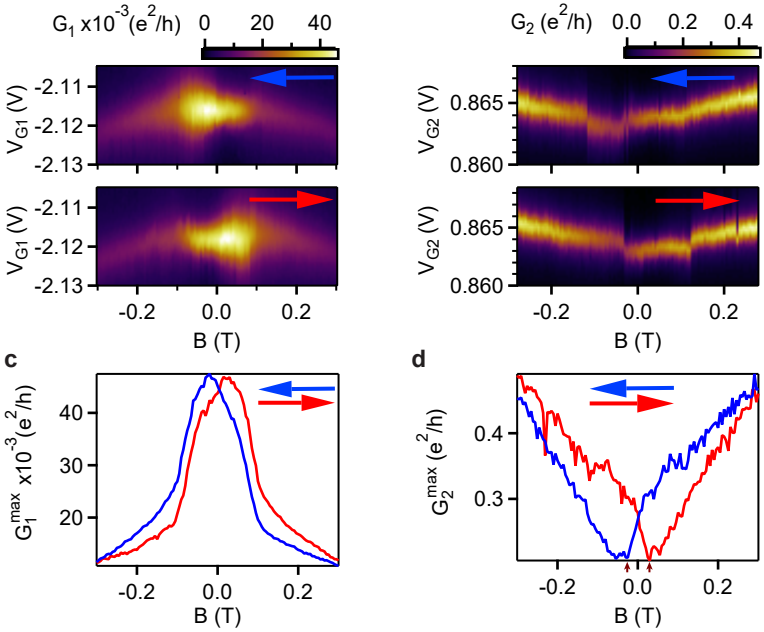

Figure 7.4. Magnetoconductance (MC) measurements. Up-(red arrow) and down-sweep (blue arrow) maps of **(a)** $G^{(1)}$ and **(b)** $G^{(2)}$ as a function of B and gate voltage **(a)** V_{G1a} and **(b)** V_{G2a} for a QD1 and QD2 resonance respectively. Conductance maximum **(c)** $G^{(1)}_{max}$ and **(d)** $G^{(2)}_{max}$ vs B extracted from figure **(a)** and **(b)** for the up (red) abd down (blue) sweep.

To demonstrate the presence of a non-zero B_{str} and determine the switching fields of the FSGs, we measure $G^{(1)}$ ($G^{(2)}$) as a function of V_{G1a} (V_{G2a}) for a QD1 (QD2) Coulomb resonance at a series of external magnetic fields B applied parallel to the FSG axes, similar to chapter 6. Such maps of $G^{(1)}$

and $G^{(2)}$ are shown in Fig. 7.4a and Fig. 7.4b for increasing and decreasing magnetic field directions, as indicated by the red and blue arrows respectively. We note that B is first swept to large values, i.e. $+0.5\,\mathrm{T}$ or $-0.5\,\mathrm{T}$, to ensure the formation of a single domain along the FSG axes. Both $G^{(1)}$ and $G^{(2)}$ maps show a clear hysteresis with strong dependence on the sweep direction of B, suggesting the presence of a finite B_{str} on both QDs. To explicitly demonstrate this, we extract the maximum conductance G_{max} for both QDs. $G^{(1)}_{\mathrm{max}}$ and $G^{(2)}_{\mathrm{max}}$ for QD1 and QD2 is plotted in Fig. 7.4c and Fig. 7.4d respectively for increasing (red) and decreasing (blue) B.

In the up sweep (red curve) of Fig. 7.4d, we observe that $G^{(2)}_{\mathrm{max}}$ decreases roughly linearly with increasing B followed by a relatively sharp decrease around $B = 0$. At $B \approx 25\,\mathrm{mT}$, $G^{(2)}_{\mathrm{max}}$ achieves it minimum value, and starts to increase with more positive B. The down sweep can be described in a similar manner, but mirror symmetric at $B \approx 0$ due to a clear hysteresis. Qualitatively, $G^{(2)}_{\mathrm{max}}$ can be understood as a smooth magnetoconductance (MC) of QD2, which changes relatively abruptly when the corresponding FSG2 reverses its magnetization direction. From the up sweep, we find that the FSG2 gets reoriented to positive B direction for $B > B_{\mathrm{sw2}} \approx 25\,\mathrm{mT}$, as indicated by the brown arrows in Fig. 7.4d (see chapter 5 for more details).

Similar to $G^{(2)}_{\mathrm{max}}$, $G^{(1)}_{\mathrm{max}}$ also exhibits a clear hysteresis around $B = 0$ as shown in Fig. 7.4c. In the up-sweep, $G^{(1)}_{\mathrm{max}}$ increases roughly linearly with increasing B till $B = -110\,\mathrm{mT}$, followed by a steep increase with a maximum at $B = 20\,\mathrm{mT}$ and a steep decrease until $B \approx 100 - 105\,\mathrm{mT}$. For $B > 100 - 105\,\mathrm{mT}$, $G^{(1)}_{\mathrm{max}}$ shows a roughly linear decrease with more positive B. The down sweep is mirror-symmetric with respect to $B = 0$. However, we do not observe sharp abrupt change in $G^{(1)}_{\mathrm{max}}$ nor in $G^{(2)}_{\mathrm{max}}$ compared to the ones found for single QD FSG devices in chapter 5. The abrupt change in slope of $G^{(1)}_{\mathrm{max}}$ at $B \approx 105\,\mathrm{mT}$ might be a signature of FSG1 reversing its magnetization direction. Although this is consistent with $B_{\mathrm{sw1}} > B_{\mathrm{sw2}}$ due to narrower width of FSG1, the exact determination of B_{sw1} still remains elusive.

To determine the antiparallel FSG magnetization states, we operate the device in a spin-valve configuration, i.e. standard two-terminal lock-in measurements with the two QDs in series with S kept floating, and measure the differential conductance G^{sv} as a function of B and V_{G1a} for increasing (red) and decreasing (blue) B as shown in Fig. 7.5a. Similar to $G^{(1)}_{\mathrm{max}}$ and $G^{(2)}_{\mathrm{max}}$, we extract G^{sv}_{max} from Fig. 7.5a, as plotted in Fig. 7.5b. In the up sweep (red curve), G^{sv}_{max} first increases with increasing B, followed by a maximum at $B \approx -130\,\mathrm{mT}$ and a subsequent decrease with a minimum at $B \approx -20\,\mathrm{mT}$. Around $B \approx 0$, G^{sv}_{max} increases again with small positive B, followed by another maximum at $B \approx 95\,\mathrm{mT}$, and a further decrease towards more positive B. We note here that G^{sv}_{max} decreases at negative B, which might be a consequence of Cooper pair splitting in our device. The down sweep (blue curve) is mirror

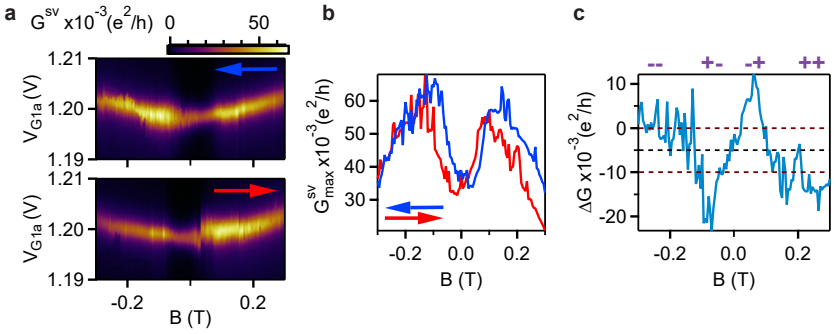

Figure 7.5. Spin Valve measurement a Up-(red arrow) and down-sweep (blue arrow) maps of $G^{(sv)}$ as a function of B and gate voltage V_{G1a} when the device is measured in a spin valve configuration. **b** Conductance maximum $G^{(sv)}_{\mathrm{max}}$ vs B extracted from figure **(a)** for the up (red) abd down (blue) sweep. **c** $\Delta G = G^{\mathrm{sv,up}}_{\mathrm{max}} - G^{\mathrm{sv,down}}_{\mathrm{max}}$ as a function of B from figure **(b)**.

symmetric to the up sweep at $B = 0$. To determine the antiparallel FSG magnetizations, we plot $\Delta G = G^{\mathrm{sv,up}}_{\mathrm{max}} - G^{\mathrm{sv,down}}_{\mathrm{max}}$ as a function of B in Fig. 7.5c, where $G^{\mathrm{sv,up}}_{\mathrm{max}}$ and $G^{\mathrm{sv,down}}_{\mathrm{max}}$ refer to the up and down sweep in Fig. 7.5b. We assign an average zero level of the measured data, as indicated by the black dashed line and define a lower and upper conductance limit for significant deviation of ΔG from the average zero. We use the B values at which the upper horizontal line meets ΔG as the two switching fields, $B_{\mathrm{sw1}} \approx 100\,\mathrm{mT}$ and $B_{\mathrm{sw2}} \approx 25\,\mathrm{mT}$, respectively. We use a similar analysis for the lower horizontal line also. Therefore, for magnetic field values between $B_{\mathrm{sw1}} > B > B_{\mathrm{sw2}}$, the FSGs can be oriented antiparallel to each other for later experiments. Therefore, this determination of the FSG switching fields along with the presence of a finite B_{str} demonstrates the coexistence of superconductivity and B_{str} in our device.

7.4. Cooper Pair Splitting

We now demonstrate the phenomenon of Cooper pair splitting in our CPS-FSG device in the presence of B_{str} which we will then analyze in different magnetization configurations in section 7.5 below. Fig. 7.6a and Fig. 7.6b show the simultaneously measured differential conductances $G^{(1)}$ and $G^{(2)}$ as a function of gate voltages V_{G1a} and V_{G2a} respectively at $B = 0$ and $V_{\mathrm{SD}} = 0$. When V_{G1a} is varied, QD1 is tuned through two resonances resulting in conductance maxima in $G^{(1)}$ as shown in Fig. 7.6a. We note that the amplitudes and res-

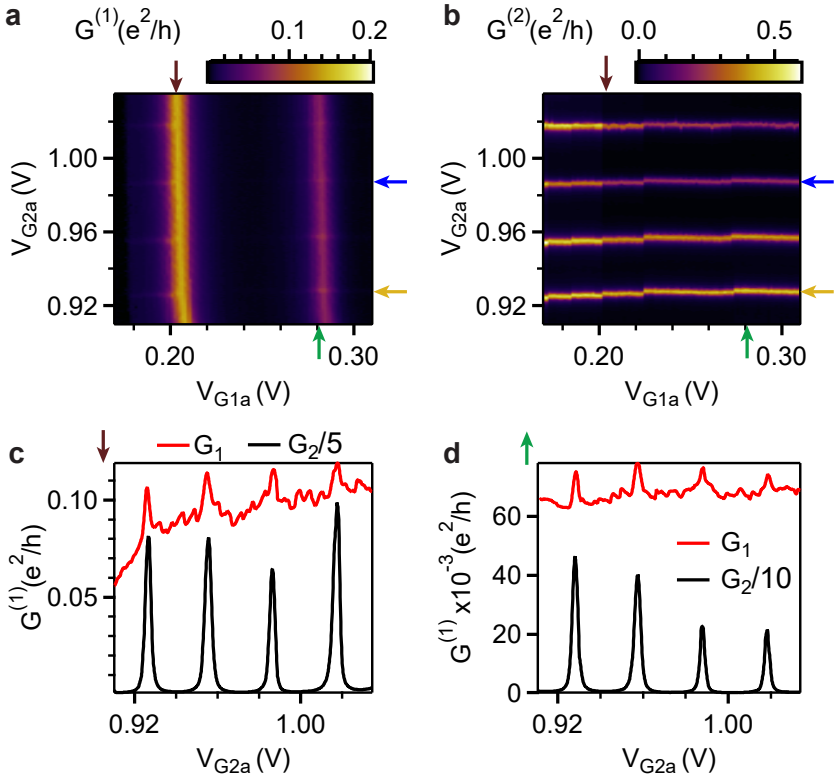

Figure 7.6. Cooper pair splitting (CPS). Maps of **(a)** $G^{(1)}$ and **(b)** $G^{(2)}$ as a function of gate voltages V_{G1a} and V_{G2a} respectively at $B = 0$ and $V_{\mathrm{SD}} = 0$. **c,d** The non local signal $G^{(1)}(V_{\mathrm{G2a}})$ (red curve) for two on-resonance positions of QD1, marked by the **(c)** brown and **(d)** green arrows in figure **(a)**, when $G^{(2)}$ (black curve) is tuned through four resonances.

onance positions vary negligibly while tuning V_{G2a} due to the low capacitive cross talk from FSG2 to QD1. We also observe similar conductance maxima (ridges) with much larger amplitudes in $G^{(2)}$ for QD2, as plotted in Fig. 7.6b. These are predominantly tuned by V_{G2a}, which results in resonances perpendicular to those observed in Fig. 7.6a due to QD1. The resonances in Fig. 7.6b exhibit multiple small shifts in Vg2, most probably due to some nearby charge rearrangements on the substrate or the NW oxide. Nevertheless, we can still trace each individual resonance in $G^{(2)}$ as a function of V_{G1a}.

CPS is manifested by pronounced peaks when both QDs are in resonance. This is prominently visible in $G^{(1)}$ for gate configurations where resonances of QD1 and QD2 overlap. The conductance increases by 15% with respect to the corresponding conductance maximum away from the resonance of the other QD. QD1 is adjusted to an on-resonance position with V_{G1a} as marked by the brown arrow in Fig. 7.6a. QD2 is then tuned across four subsequent resonances, showing Coulomb blockade peaks when a QD2 level is in resonance (black curve) in Fig. 7.6c. We simultaneously measure $G^{(1)}(V_{\mathrm{G2a}})$ and observe a increase in the non-local conductance when QD2 is also tuned to on-resonance, while the background is due to local pair tunneling (LPT) processes [59]. The non-local conductance $G^{(1)}(V_{\mathrm{G2a}})$ for another on-resonance position of QD1 (green arrow in Fig. 7.6a) exhibits similar behavior on tuning QD2 through the same subsequent four resonances, as shown in Fig. 7.6d. In addition, we observe a suppressed non-local signal at the resonance crossings when the S contact is driven into the normal state by applying B greater than the critical field [52].

We expect the same non-local signal strength on the other arm, which, however, is below the signal to noise detection limit of our experiment, since the local signal is 10 times larger than in arm 1, i.e. $G^{(2)} \sim 10G^{(1)}$. The large amplitude of $G^{(2)}(V_{\mathrm{G1a}})$ limits the visibility of a small increase $\sim 1\%$ in its conductance from CPS. Such large background might be due to a LPT process, where the two Cooper pair electrons tunnel sequentially via a virtual quasiparticle state in S into QD2 [59] or resonant Andreev tunneling [230].

7.5. Spin correlation experiments in a CPS device

We now will investigate the spin correlation of the CPS currents. To do so, we now focus on individual resonance crossings to explicitly quantify the non-local CPS signal and determine its dependence on the four FSG magnetization states (two parallel and two anti-parallel). Fig. 7.7a and Fig. 7.7b show simultaneously measured $G^{(1)}$ and $G^{(2)}$ for two resonance crossings (L1,R1) and (L1,R2) at $B = 0$ (not shown in Fig. 7.6). Similar to Fig. 7.6, we observe prominent peaks in $G^{(1)}$ at gate voltages where the two QDs are resonant, while no such peaks are observed in $G^{(2)}$ due to the large background. To explicitly demonstrate CPS, we extract the non-local maximum conductance $G^{(1)}_{\mathrm{max}}(V_{\mathrm{G2a}})$ from Fig. 7.7a. This is achieved by taking cross sections of $G^{(1)}$ as a function of V_{G1a} at each V_{G2a} setting, followed by fitting with a Lorentzian to extract the maximum conductance, similar to chapter 6. $G^{(1)}_{\mathrm{max}}(V_{\mathrm{G2a}})$ extracted from Fig. 7.7a is shown in Fig. 7.7c. Sharp peaks (red line) are observed at the voltages of resonance R1 and R2, which are similar in shape and width as the resonances in $G^{(2)}$ (black line). For clarity, a zoom-in plot of $G^{(1)}_{\mathrm{max}}(V_{\mathrm{G2a}})$ (red line in Fig. 7.7c) is shown in Fig. 7.7d. In addition, when the superconductiv-

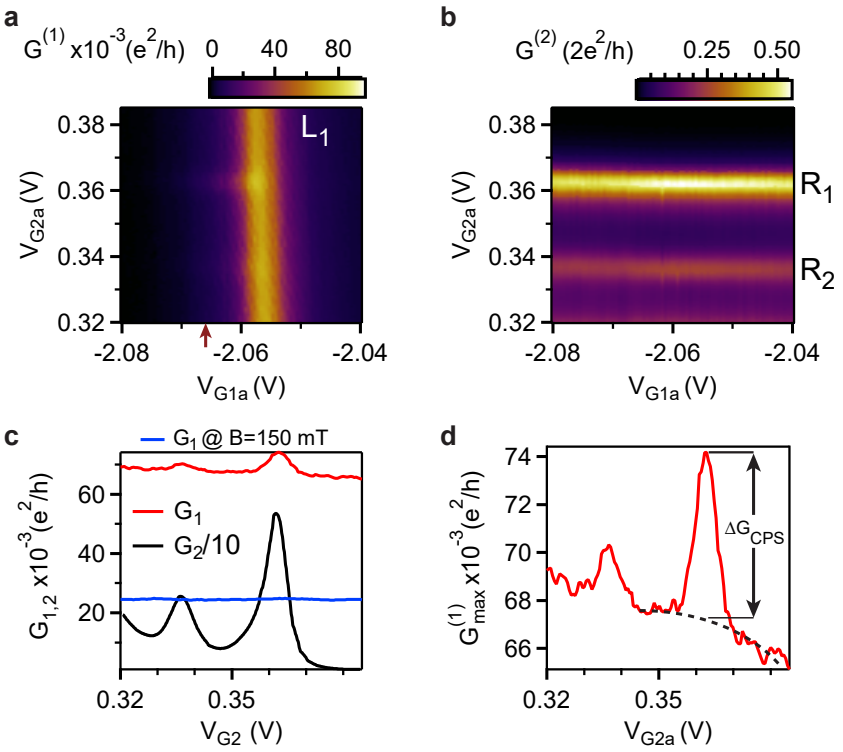

Figure 7.7. CPS for Individual Resonance Crossings. Maps of **(a)** $G^{(1)}$ and **(b)** $G^{(2)}$ as a function of gate voltages V_{G1a} and V_{G2a} respectively at $B = 0$ and $V_{\mathrm{SD}} = 0$. **c** The non local signal $G^{(1)\mathrm{max}}(V_{\mathrm{G2a}})$ at $B = 0$ (red curve) and $B = +150\,\mathrm{mT}$ (blue curve) when $G^{(2)}$ (black curve) is tuned through two resonances. **d** Zoom-in plot of $G^{(1)\mathrm{max}}(V_{\mathrm{G2a}})$ at $B = 0$ (red curve) showing the extracted CPS signal ΔG_{CPS}.

ity is suppressed with an external magnetic field $B = +150\,\mathrm{mT}$, we observe no peaks (blue line) in $G^{(1)}_{\mathrm{max}}(V_{\mathrm{G2a}})$, consistent with S being in the normal state.

To quantify the CPS signal in QD1, we use the amplitude $\Delta G_{\mathrm{CPS}} = G^{(1)}_{\mathrm{max}} - G_{\mathrm{background}}$ of the (L1,R1) peak in $G^{(1)}_{\mathrm{max}}(V_{\mathrm{G2a}})$, as shown in Fig. 7.7d. $G_{\mathrm{background}}$ is obtained by interpolating the local background with a 2nd-order polynomial (black dashed line in Fig. 7.7d). On the resonance crossing, we obtain $\Delta G_{\mathrm{CPS}} = 0.0085\, e^2/h$. We now define the *visibility* of CPS in the QD1 arm of the device as $\eta_1 = \Delta G_{\mathrm{CPS}}/G^{(1)}_{\mathrm{max}}$ [59], i.e. the ratio of the CPS conductance to

the total conductance in one arm, including the local processes. Similarly, one can define $\eta_2 = \Delta G_{\mathrm{CPS}}/G^{(2)}_{\mathrm{max}}$ for QD2. η_1 has a value of 9−10% on-resonance, comparable to the best NW CPS devices [54, 55], though below the theoretically possible 100% [59]. η_1 increases to $\eta_1 \approx 35\%$ slightly off-resonance for QD1, as marked by the brown arrow in Fig. 7.7a. For the sake of analysis, we assume that Cooper pair splitting results in conductance ΔG_{CPS} in both QD arms independent of other processes, although $\eta_2 \approx 0$ for QD2 due to the large local background. Therefore, we define the CPS efficiency [59] as

$$s = \frac{2\Delta G_{\mathrm{CPS}}}{G^{(1)}_{\mathrm{max}} + G^{(2)}_{\mathrm{max}}} \tag{7.2}$$

Using ΔG_{CPS} from Fig. 7.7d, we find a CPS efficiency of $\sim$ 2.3% in the presence of stray magnetic fields. Although these are not the best values, we still obtain clear CPS, with further techniques to improve the splitting efficiency discussed in chapter 9.

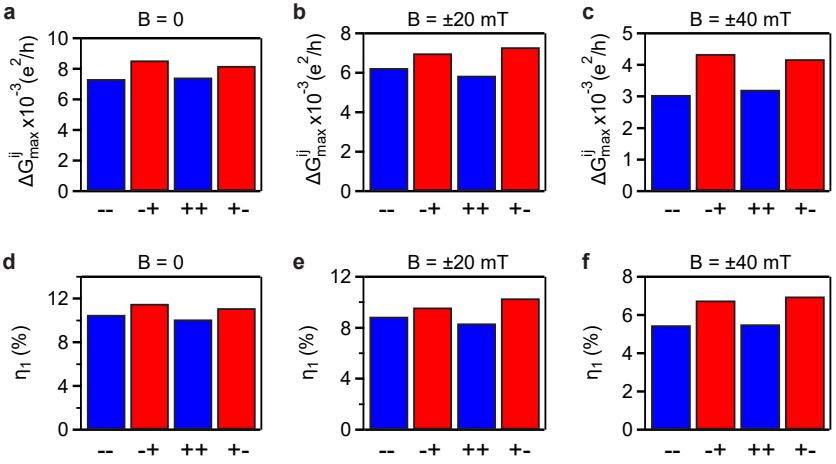

Figure 7.8. On-resonance CPS conductance and visibility. **(a-c)** CPS conductance $\Delta G^{ij}_{\mathrm{CPS}}$ and **(d-f)** visibility η_1 for the four FSG magnetization states at **(a,d)** $B = 0$, **(b,e)** $B = \pm 20\,\mathrm{mT}$ and **(c,f)** $B = \pm 40\,\mathrm{mT}$ for the resonance crossing (L1,R1) in Fig. 7.7.

We now investigate the effect of projecting the spin states of the CPS signal onto two axis given by the magnetization of the two FSGs. We apply an external magnetic field B along the FSG long axes to set the FSG magnetizations and then read out the corresponding CPS conductance $\Delta G^{ij}_{\mathrm{CPS}}$ and the CPS

visibility η_1. To reach the respective magnetization states of the FSGs, we use the following sweep patterns:

1. (-,-): Sweep the external magnetic field to $B = -500\,\mathrm{mT} << -B_{\mathrm{sw1}}$ in order to form a single magnetic domain along the FSG axis, followed by a sweep back to $B = 0$ (or $B = -40\,\mathrm{mT}$) to obtain the magnetization state $(-,-)$.

2. (-,+): Continue sweeping to $B = +60\,\mathrm{mT} > B_{\mathrm{sw2}}$ (but $< B_{\mathrm{sw1}}$) followed by a sweep back to $B = 0$ (or $B = +40\,\mathrm{mT}$) to obtain the magnetization state $(-,+)$.

3. (+,+): Sweep to $B = +500\,\mathrm{mT} >> B_{\mathrm{sw1}}$ to get a single magnetic domain along the $+B$ direction, followed by a sweep back to $B = 0$ (or $B = +40\,\mathrm{mT}$) to obtain $(+,+)$.

4. (+,-): Continue sweeping to $B = -60\,\mathrm{mT} < -B_{\mathrm{sw2}}$ (but $> -B_{\mathrm{sw1}}$) followed by a sweep back to $B = 0$ (or $B = -40\,\mathrm{mT}$) to obtain $(+,-)$.

We note that in the above sequence, parallel states are followed by antiparallel states and vice versa. We then simultaneously measure $G^{(1)}$ and $G^{(2)}$ at each magnetization state and extract ΔG_{CPS} and η_1 from $G^{(1)}_{\mathrm{max}}$, as described above. We note that the $G^{(1)}_{\mathrm{max}}$ shows CPS peaks at the same gate voltage for all four magnetization states, while the amplitude of the CPS peaks ΔG_{CPS} varies between the p and ap states. ΔG_{CPS} and η_1, measured on-resonance, for the four magnetization states at $B = 0, \pm 20, \pm 40\,\mathrm{mT}$ are shown in Fig. 7.8a-c and Fig. 7.8d-f, respectively. We find very similar CPS conductance and visibility for the same relative magnetization configurations and a clear suppression in ΔG_{CPS} and η_1 for the two p magnetization states compared to the two ap states. We note that the CPS conductance for ap states are larger than those of the parallel states, i.e. $\Delta G_{\mathrm{CPS,ap}} > \Delta G_{\mathrm{CPS,p}}$ in Fig. 7.8, qualitatively consistent with the interpretation of negative spin cross correlation between the split Cooper pair electrons originating from spin singlet BCS ground state (detailed discussion in section 7.6). In addition, we find that the magnitudes of ΔG_{CPS} and η_1 decreases with increasing B in Fig. 7.8a-c, consistent with Cooper pair splitting being suppressed in the presence of increasing external magnetic field.

Another Resonance Crossing

We measure $G^{(1)}$ and $G^{(2)}$ for another resonance crossing as presented in Fig. 7.9a and Fig. 7.9b at $B = 0$. Similar to resonance crossing (L1,R1) in Fig. 7.7, we observe prominent peaks in the non-local conductance $G^{(1)}(V_{\mathrm{G2a}})$ for QD1, as shown in Fig. 7.9c for the (-,+) magnetization state at $B = 0$. No

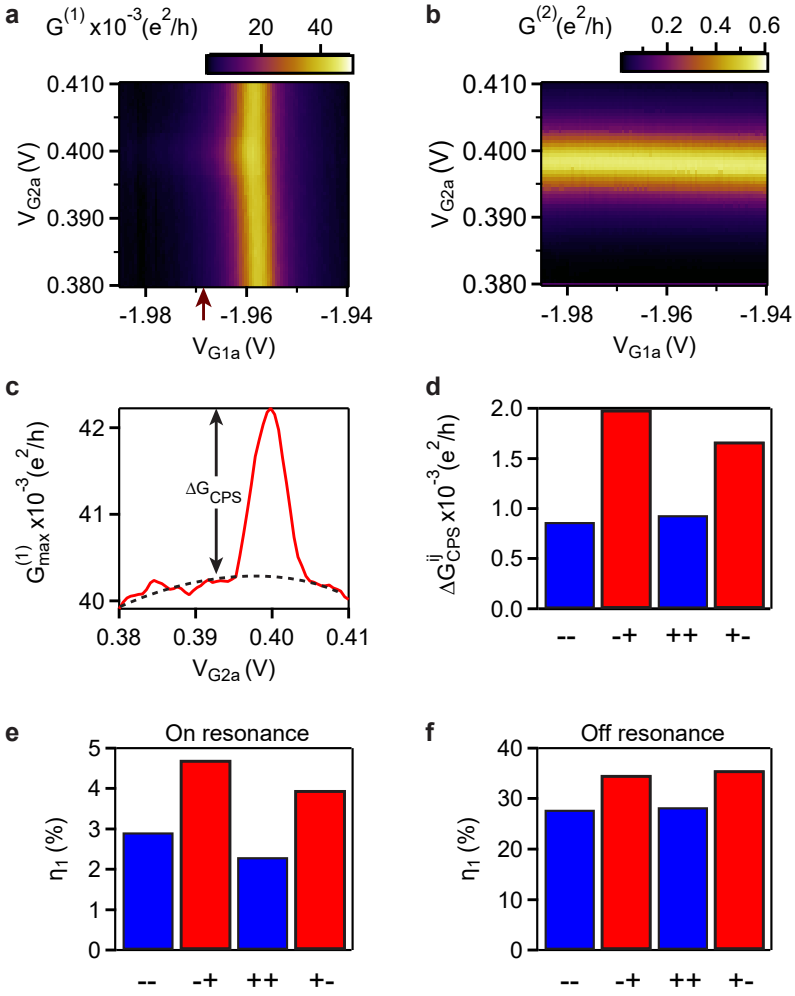

Figure 7.9. CPS for resonance crossing II. Maps of **(a)** $G^{(1)}$ and **(b)** $G^{(2)}$ as a function of gate voltages V_{G1a} and V_{G2a} respectively at $B = 0$ and $V_{\mathrm{SD}} = 0$. **c** The non-local signal $G^{(1)\mathrm{max}}(V_{\mathrm{G2a}})$ for the (-,+) magnetization state at $B = 0$ extracted from figure **(a)**. **(d)** CPS conductance $\Delta G^{ij}_{\mathrm{CPS}}$, **(e)** visibility η_1 on-resonance and **(f)** visibility η_1 off-resonance (brown arrow in figure **(a)**) for the four FSG magnetization states at $B = 0$.

such peaks are seen for QD2 due to a large local background. We extract an on-resonance visibility of $\eta_1 \approx 3-5\%$, which increases to $\eta_1 \approx 28-35\%$ when measured slightly off-resonance for QD1 (brown arrow in Fig. 7.9a). ΔG_{CPS} and η_1, measured on-resonance at $B = 0$, for each of the four magnetization states are shown in Fig. 7.9d and Fig. 7.9e respectively, while the off-resonance CPS visibility is plotted in Fig. 7.9e. The observations for this resonance crossing are also consistent with the interpretation of spin cross anti-correlated CPS, similar to resonance crossing(L1,R1) in Fig. 7.7.

7.6. Spin Correlation Calculation

In general, a correlation function is given by the expectation value of the product of two variables, $\langle \sigma_1 \otimes \sigma_2 \rangle$ in our case. In this section, we derive and calculate the expectation value of the spin cross correlation operator for our measured CPS conductance dependent on the FSG magnetization states. For the sake of analysis, we assume ΔG_{CPS} is same in both QDs and define the spin quantization axis along the $+\hat{z}$-direction.

Quantum description of ferromagnetic detectors

We use the term *non-ideal detectors* to signify partially polarized spin detectors, i.e. the spin polarization is $P_{1,2} < 1$ for the detectors QD1 and QD2 in our device. For such non-ideal ferromagnetic spin detectors with a finite DOS of both spin components at the Fermi energy E_{F}, an electron in state $|\uparrow\rangle_z$ can enter the detector with opposite majority spins and be wrongly detected as $|\downarrow\rangle_z$ with non-zero probability. Therefore, we define the non-ideal measurement operators of the spin detector by [140]:

$$\begin{aligned} M^{+} &= \Gamma_{\uparrow}^{+} |\uparrow\rangle \langle\uparrow| + \Gamma_{\downarrow}^{+} |\downarrow\rangle \langle\downarrow| \\ M^{-} &= \Gamma_{\uparrow}^{-} |\uparrow\rangle \langle\uparrow| + \Gamma_{\downarrow}^{-} |\downarrow\rangle \langle\downarrow| \end{aligned} \tag{7.3}$$

where +(-) denotes the detector magnetization set parallel (antiparallel) to the quantization axis. $\Gamma_{\uparrow,\downarrow}^{i}$ is related to the density of states (DOS) at the Fermi energy E_{F} by:

$$\Gamma_{\uparrow,\downarrow}^{i} = \frac{D_{\uparrow,\downarrow}(E_{\mathrm{F}})}{D_{\uparrow}(E_{\mathrm{F}}) + D_{\downarrow}(E_{\mathrm{F}})} \tag{7.4}$$

where $i \in \{+,-\}$ such that $\Gamma_{\uparrow}^{i} + \Gamma_{\downarrow}^{i} = 1$. Using the definition of spin polarization from Eq. 7.1, we can rearrange the $\Gamma_{\uparrow,\downarrow}^{i}$ to:

$$\begin{aligned}\Gamma^i_\uparrow &= \frac{1}{2}(1+P^i)\\ \Gamma^i_\downarrow &= \frac{1}{2}(1-P^i)\end{aligned} \tag{7.5}$$

where $P^i = \begin{cases} P, & i=+ \\ -P, & i=- \end{cases}$ and $P \in [0,1]$ is the absolute value of the spin polarization. For ideal spin detectors, $P=1$ which results in $\Gamma^+_\uparrow = \Gamma^-_\downarrow = 1$ and $\Gamma^-_\uparrow = \Gamma^+_\downarrow = 0$. This gives us the ideal projection operators $M^+ = |\uparrow\rangle\langle\uparrow|$ and $M^- = |\downarrow\rangle\langle\downarrow|$ from Eq. 7.3. The non-ideal spin projection operator along the $\hat{z}$-quantization axis for a single electron spin can then defined as

$$M_{\mathrm{s},\hat{z}} = M^+ - M^- = P(|\uparrow\rangle\langle\uparrow| - |\downarrow\rangle\langle\downarrow|) \tag{7.6}$$

where P is the polarization of the spin detector (spin polarized QD in our device). For ideal detectors, $P=1$ resulting in $M_{\mathrm{s},\hat{z}} = |\uparrow\rangle\langle\uparrow| - |\downarrow\rangle\langle\downarrow|$. Similarly, we define the non-ideal spin projection operator for measuring spin correlation between two electron spins as:

$$\begin{aligned}M_{\mathrm{d},\hat{z}} &= (M_1^+ - M_1^-)\otimes(M_2^+ - M_2^-)\\ &= P_1P_2(|\uparrow\uparrow\rangle\langle\uparrow\uparrow| - |\uparrow\downarrow\rangle\langle\uparrow\downarrow| - |\downarrow\uparrow\rangle\langle\downarrow\uparrow| + |\downarrow\downarrow\rangle\langle\downarrow\downarrow|)\end{aligned} \tag{7.7}$$

where P_1 and P_2 are the spin polarizations of the two spin detectors QD1 and QD2 respectively. For a spin singlet CPS state $|cps\rangle = \frac{1}{\sqrt{2}}[|\uparrow\downarrow\rangle - |\downarrow\uparrow\rangle]$, we obtain the expectation value $\langle cps| M_{\mathrm{d},\hat{z}} |cps\rangle = -P_1P_2 < 0$, demonstrating the anti-correlation of the spins in a singlet. For ideal detectors $P_1 = P_2 = 1$, we obtain $\langle cps| M_{\mathrm{d},\hat{z}} |cps\rangle = -1$, i.e. the experiment would show the full anti-correlation of a Cooper pair singlet. A smaller polarization would register as a smaller correlation, although the CPS state is fully anti-correlated. This shows that the detector quality is relevant. We note that the product state $|s\rangle = |\uparrow\downarrow\rangle$ also yields $\langle\uparrow\downarrow| M_{\mathrm{d},\hat{z}} |\uparrow\downarrow\rangle = -P_1P_2 < 0$, exactly as the $|cps\rangle$ state. On the other hand, the product state $|s\rangle = |\uparrow\uparrow\rangle$ gives $\langle\uparrow\uparrow| M_{\mathrm{d},\hat{z}} |\uparrow\uparrow\rangle = P_1P_2 > 0$ signifying positively correlated states.

Spin correlation operator

We now define the experimental spin correlation operator $\hat{C}_{\mathrm{exp}}$ for non-ideal detectors as:

$$\begin{aligned}\hat{C}_{\text{exp}} &= \frac{P_1P_2(|\uparrow\uparrow\rangle\langle\uparrow\uparrow| - |\uparrow\downarrow\rangle\langle\uparrow\downarrow| - |\downarrow\uparrow\rangle\langle\downarrow\uparrow| + |\downarrow\downarrow\rangle\langle\downarrow\downarrow|)}{|\uparrow\uparrow\rangle\langle\uparrow\uparrow| + |\uparrow\downarrow\rangle\langle\uparrow\downarrow| + |\downarrow\uparrow\rangle\langle\downarrow\uparrow| + |\downarrow\downarrow\rangle\langle\downarrow\downarrow|} \\ &= \frac{M_{\text{d},\hat{\text{z}}}}{|\uparrow\uparrow\rangle\langle\uparrow\uparrow| + |\uparrow\downarrow\rangle\langle\uparrow\downarrow| + |\downarrow\uparrow\rangle\langle\downarrow\uparrow| + |\downarrow\downarrow\rangle\langle\downarrow\downarrow|}\end{aligned} \tag{7.8}$$

Assuming constant tunnel barrier strength and attempt frequency f with which Cooper pairs are scattered at the interface to the QDs for all FSG magnetization states, the FSG dependent charge conductance for a stream of electrons in state $\sigma \in \{\uparrow,\downarrow\}$ through a single QD detector can be related to the non-ideal measurement operators as:

$$G^i \propto \Gamma^i_\uparrow |\uparrow\rangle\langle\uparrow| + \Gamma^i_\downarrow |\downarrow\rangle\langle\downarrow| \tag{7.9}$$

where $i \in \{+,-\}$ denote the QD FSG orientation. For a two QD detector system, the charge conductance is then given by the product of the individual QD transmissions. This results in the relation:

$$\begin{aligned}&G^{++} - G^{+-} - G^{-+} + G^{--} \propto P_1P_2(|\uparrow\uparrow\rangle\langle\uparrow\uparrow| - |\uparrow\downarrow\rangle\langle\uparrow\downarrow| - |\downarrow\uparrow\rangle\langle\downarrow\uparrow| + |\downarrow\downarrow\rangle\langle\downarrow\downarrow|) = M_{\text{d},\hat{\text{z}}} \\ &G^{++} + G^{+-} + G^{-+} + G^{--} \propto |\uparrow\uparrow\rangle\langle\uparrow\uparrow| + |\uparrow\downarrow\rangle\langle\uparrow\downarrow| + |\downarrow\uparrow\rangle\langle\downarrow\uparrow| + |\downarrow\downarrow\rangle\langle\downarrow\downarrow|\end{aligned} \tag{7.10}$$

Therefore, the CPS conductances are a result of the spin correlations. Assuming $G^{++} = G^{--}$ and $G^{+-} = G^{-+}$, one obtains using Eq. 7.8 and Eq. 7.10:

$$\langle cps|\,\hat{C}_{\text{exp}}\,|cps\rangle = \frac{G^{++} - G^{+-}}{G^{++} + G^{+-}} \approx -\frac{1}{3} < 0 \tag{7.11}$$

where G^{++} and G^{+-} are the on-resonance experimentally measured values in Fig. 7.9. This signifies that the measured CPS conductances in one arm are in agreement with spin cross anti-correlation between the split electrons. For the $|cps\rangle$ state, we find $\langle cps|\,\hat{C}_{\text{exp}}\,|cps\rangle = -P_1P_2 \approx -P^2 = -1/3$, where we assumed identical spin polarization P for both QDs in the last step. Assuming full singlet states from the CPS process, we obtain $P \approx 57\%$ on resonance at $B = 0$, very similar to values achieved in the double quantum dot spin valve experiment at $B = 0$ in chapter 6.

7.7. Discussion and Conclusion

In our experiments, current cross correlation was observed in only QD1, while it could not be resolved for the currents in QD2. However, there are various other transport mechanisms that can result in conductance change in only arm of a CPS device. These mechanisms are based on two basic principles:

(1) the probability of local and non-local processes depend on the individual QD transmissions, and (2) a finite interdot coupling between the two QDs results in a local process that depends on the occupation of both QDs.

The various single and two electron transport processes that can occur in our device are[54] : (1) tunneling of an electron from a filled QD to the respective N contact, known as single electron tunneling (SET); (2) LPT process where Cooper pair electrons can sequentially tunnel through the same QD via a quasiparticle state in S or a higher order tunneling process, e.g. Andreev tunneling, as described in section 2.3.3; (3) two particle CPS process as described in section 2.3.3; (4) single electron tunneling between the two QDs either directly through the InAs segment below S or through higher order processes mediated by S; and (5) a combination of processes where a Cooper pair electron sequentially tunnels into one QD and then tunnels to the other dot (sequential CPS). A schematics of all these processes can be found in Ref. [54].

Each process has a probability that predominantly depends on the tunnel couplings both to the respective normal metal contact Γ_{Ni}, S contact Γ_{Si} or interdot coupling Γ_{12} between the two dots, where the used notations are illustrated in Fig. 2.18. Such interplay between different processes is shown to result in non-ideal conductance correlations between the QDs [54]. Positive conductance correlations between the QDs occurs only if the probability of CPS process is non-zero [54]. On the other hand, negative or zero (no conductance change) conductance correlations between the two signals can occur due to: (1) finite interdot coupling that diverts tunneling current from one QD to the other, thereby increasing the current in one N contact and decreasing it in the other N contact; and (2) competition for occupying each QD by local and non local processes. For example, when both QDs are brought on-resonance, the probability of QD1 getting occupied due to CPS increases, which effectively decreases the frequency of the local processes. Similarly, another effect of such large occupation probability of a QD is that the conductance change in both arms are not identical i.e. ΔG_{CPS} is different for both QDs, which can manifest itself as negligible non-local signal in the populated QD arm if Γ_{12} between the dots is relevant [54, 59].

Such large QD occupation probability primarily depends on the individual tunnel barriers between the QD and the respective S and N contacts. If the barrier to N is very opaque, the inter dot tunnel coupling Γ_{12} comes into play, which can lead to no conductance variation in one QD arm as the electron takes the path to the other QD. Similarly, if the barrier to S become very weak, the QD population increases which can also lead to non-ideal current correlations. Therefore, the ideal case for CPS is to have negligible inter-dot coupling Γ_{12} and $\Gamma_{\mathrm{S}} << \Gamma_{\mathrm{N}}$ in each dot, which does not appear to be the case for QD2 in our CPS-FSG device. The tuning of FSG2 gate did not provide sufficient control over the tunnel barrier between S and QD2.

This necessitates the use of controllable tunnel barriers, which can be achieved

either by etching the NW with a dilute piranha solution [231], or by electrically tuning them using precise bottom gate structures [54, 55]. In addition, the direct tunneling of electrons through the NW segment beneath the superconductor can be suppressed by cutting the NW using focused ion beam (FIB) [232–234], which ensures two completely decoupled QDs.

In conclusion, we have performed bias spectroscopy to establish the formation of single QD in both arms of the CPS-FSG device as well as determine a superconducting gap of $\sim 110\,\mu$eV, which gets completely suppressed at $B_C \approx 90\,$mT. We demonstrated hysteretic MC in both QDs of the CPS device along with independent switching of the respective FSGs, signifying the presence of a non-zero B_{str} in each dot. This confirms the coexistence of B_{str} and superconductivity at close proximity in our device. We further demonstrated non-local signatures of Cooper pair splitting in the presence of B_{str} in one QD arm of our device. The investigation of this non-local CPS conductance for the four FSG magnetization states showed suppressed conductance for parallel magnetization states with respect to antiparallel states, consistent with the interpretation and calculation of spin cross anti-correlation for the spin singlet CPS ground state.

$$\langle \Delta G_{1,CPS} * \Delta G_{2,CPS} \rangle > 0 \tag{7.12}$$

8 Spin Blockade Effect at Large Magnetic Field

In this chapter, we investigate the Pauli spin blockade (PSB) effect in a DQD at zero as well as very large in-plane magnetic fields of $> 1\,\mathrm{T}$ applied along the FSG long axes. We show standard PSB at $B = 0$ and observe a complete suppression of the tunneling current at $B \sim 1.5\,\mathrm{T}$, consistent with the singlet-triplet ground state transition of the DQD. Simultaneously, we find an emergence of the tunneling current for an adjacent charge transition with one electron less (odd number of total electrons) in the DQD, which was completely suppressed around $B = 0$. This charge transition exhibits unconventional spin blockade for an odd number of total electrons at magnetic fields $B > 1.75\,\mathrm{T}$, which can potentially occur when the DQD achieves a quadruplet state similar to a three electron system [235, 236].

8.1. Introduction

Pauli Spin Blockade (PSB) is an important transport phenomenon for investigating fundamental physics in semiconductor quantum dot systems [85]. The spin to charge conversion mechanism in PSB [87] has been used to examine spin orbit effects [237], electron spin T_1 relaxation times [238], singlet-triplet splitting [239], electron spin coupling to lattice nuclear spins [240] as well as initialize and read-out electron spin states in the spin qubit. Yet, the magnetic field dependence of PSB has been mostly studied in the low (near zero) magnetic field regime. Here, we experimentally investigate the PSB phenomena at large ($> 1\,\mathrm{T}$) in-plane external magnetic fields B and find an unconventional spin blockade effect with an odd number of total electrons in the DQD.

In this chapter, we first demonstrate PSB at $B = 0$ in a double quantum dot (DQD) (same device as in chapter 6) for bias triangles with an even number of total electrons in the DQD. We then qualitatively investigate these charge transitions at $> 1\,\mathrm{T}$ in-plane external magnetic field, where the FSG magnetizations are oriented in a parallel configuration relative to each other. We observe a singlet-triplet ground state transition at $\sim 1.5\,\mathrm{T}$ as well as find the simultaneous emergence of a different bias triangle at $B > 1.5\,\mathrm{T}$ which was completely suppressed around $B = 0$. Such a bias triangle exhibits unconventional spin blockade effect at $\sim 1.75\,\mathrm{T}$, similar to PSB at $B = 0$, but with an odd number of total electrons in the DQD. Our experiment explicitly demonstrates control over the electron spin states at large magnetic fields in InAs nanowires (NWs) and provides insights into charge transfer mechanisms at large B where new physics is likely to be found.

8.2. Device and Characterization

The schematics and the scanning electron microscopy (SEM) image of the investigated InAs nanowire (NW) DQD device are shown in Fig. 8.1a and 8.1b, respectively. We note that the InAs NW device used here is the same double quantum dot spin valve (DQD-SV) device used in Chapter 6. In this experiment, the FSG magnetizations are oriented in a parallel configuration for $B > 1\,\mathrm{T}$, which is larger than the coercive fields of our Permalloy (Py) FSGs. For all measurements also around $B = 0$, we ensure parallel FSG magnetization by first sweeping B to $1\,\mathrm{T}$ and then back to zero. The DC current I resulting from a bias voltage V_{SD} and the differential conductance $G = \mathrm{d}I/\mathrm{d}V_{\mathrm{SD}}$, are then measured simultaneously using standard DC and lock-in techniques ($V_{\mathrm{ac}} = 10\,\mu\mathrm{V}$), at a base temperature of $\sim 50\,\mathrm{mK}$.

In Fig. 8.1c, we plot the current I flowing through the DQD at $V_{\mathrm{SD}} = 1\,\mathrm{mV}$ and $B = 0$, as a function of V_{G1} and V_{G4}. This map shows a typical DQD charge stability diagram with several bias triangles characteristic for a weakly coupled DQD. These triangles originate when a resonance from each QD aligns

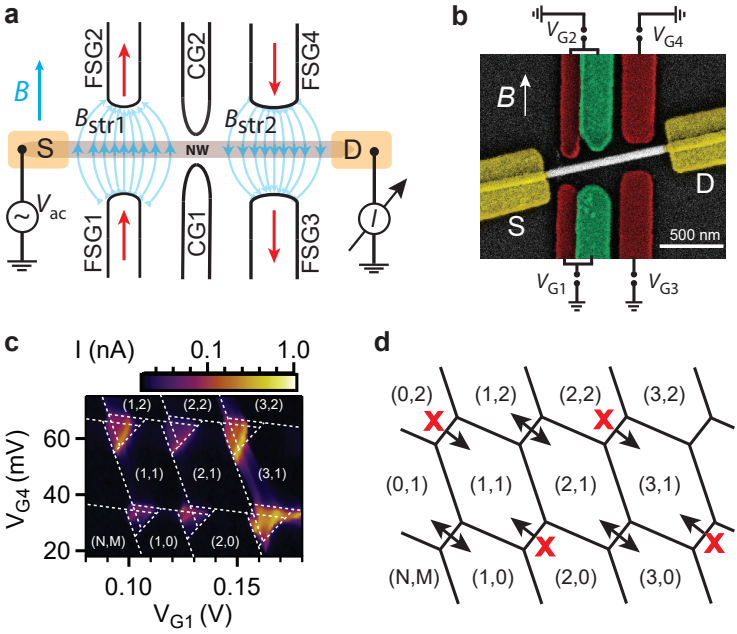

Figure 8.1. Double quantum dot (DQD) device. **a** Schematics and **b** scanning electron microscope (SEM) image of the DQD device. **c** Current I as a function of gate voltages V_{G1} and V_{G4}, at $V_{SD} = +1$ mV, showing bias triangles characteristic for weakly coupled DQDs. **d** Schematics of a DQD charge stability diagram illustrating the interdot transitions at which PSB is expected (purple cross).

in energy within the bias transport window. [97] We expect an odd-even charge filling of the DQD energy levels based on the Pauli exclusion principle, i.e. every odd electron tunneling into a QD occupies a new level, while every even electron pairs with the preceding odd electron to form a spin singlet. The exact electron occupation number in each QD is denoted by (N,M), where N and M are integers. However for the sake of simplicity, we use the notation (1,1) instead of (N+1,M+1), otherwise stated, to denote the effective occupation of the individual QDs in this chapter.

When the total number of electrons in the DQD is odd in the DQD as shown in Fig. 8.1d (details in chapter 2), the current can flow uninhibited in both bias directions inside the bias triangle via spin doublet states, as indicated by the double-sided arrows [241]. In contrast, when the total number of electrons

in the DQD is even, both QDs can have either an even number of electrons resulting in a spin singlet ground state, or an odd occupancy resulting in a charge state that can be either a spin triplet or spin singlet. For such bias triangles with odd occupancy in both QDs, current is blocked for one bias direction as marked by the red X in Fig. 8.1d when the applied bias voltage is less than the singlet-triplet splitting in the doubly even occupied charge state, i.e. energy gap between the singlet ground state and first triplet state. In the opposite bias direction, current can flow uninterrupted via the singlet states. This current blockade phenomenon is known as Pauli spin blockade (PSB) effect. We discuss the relevant DQD energy diagrams for PSB along with its experimental demonstration for the interdot charge transitions $(1,1) \rightarrow (0,2)$ and $(1,1) \rightarrow (2,0)$ in the following section.

8.3. Standard Pauli Spin Blockade

The current I through the DQD as a function of gate voltages V_{G1} and V_{G4} at $B = 0$ is shown in Figure 8.2a,b and Figure 8.2c,d for the interdot charge transitions $(1,1) \rightarrow (2,0)$ and $(1,1) \rightarrow (0,2)$ respectively. The left column Figure 8.2a,c is measured at a negative bias voltage $V_{\mathrm{SD}} = -1\,\mathrm{mV}$, while the middle column Figure 8.2b,d is measured at the positive bias voltage $V_{\mathrm{SD}} = +1\,\mathrm{mV}$. PSB is observed for the corresponding charge transitions predicted in Fig. 8.1d. For the $(1,1) \rightarrow (2,0)$ charge transition in Fig. 8.2b, we measure a current suppression at $V_{\mathrm{SD}} = +1\,\mathrm{mV}$ in the region enclosed by the white dashed lines. The corresponding DQD energy diagram is illustrated in Fig. 8.2f (for further details, see Chapter 2.1.7). An electron can enter the right dot into either the triplet T(1,1) or singlet S(1,1) state. If it enters the S(1,1) state, it can tunnel through the DQD via the S(2,0) state. However, if the T(1,1) state gets occupied, current flow is blocked as the electron can neither tunnel into the S(2,0) state as long as no spin flips occur nor it can go back into the right lead due to the Fermi distribution that is re-established on a much faster time scale [87]. Therefore, transport through the T(1,1) state requires a spin flip or second-order spin exchange process with one of the leads. These processes are relatively slow resulting in PSB. In contrast, at $V_{\mathrm{SD}} = -1\,\mathrm{mV}$ in Fig. 8.2a, current can flow from left to right through the S(2,0)$\rightarrow$S(1,1) states as shown in Fig. 8.2e.

For the mirror-symmetric $(0,1) \rightarrow (1,1) \rightarrow (0,2) \rightarrow (0,1)$ charge cycle, we expect PSB at $V_{\mathrm{SD}} = -1\,\mathrm{mV}$, as is intuitively clear from Fig. 8.1d. The current I through the DQD flows at $V_{\mathrm{SD}} = +1\,\mathrm{mV}$ as shown in Fig. 8.2d. In contrast, at $V_{\mathrm{SD}} = -1\,\mathrm{mV}$ in Fig. 8.2c, we observe a current suppression in the region enclosed by red dashed lines at the base of the bias triangle. The electron transport mechanism for PSB in the $(1,1) \rightarrow (0,2)$ transition at $V_{\mathrm{SD}} = -1\,\mathrm{mV}$ is similar to the $(1,1) \rightarrow (2,0)$ transition at $V_{\mathrm{SD}} = +1\,\mathrm{mV}$ (illustrated in

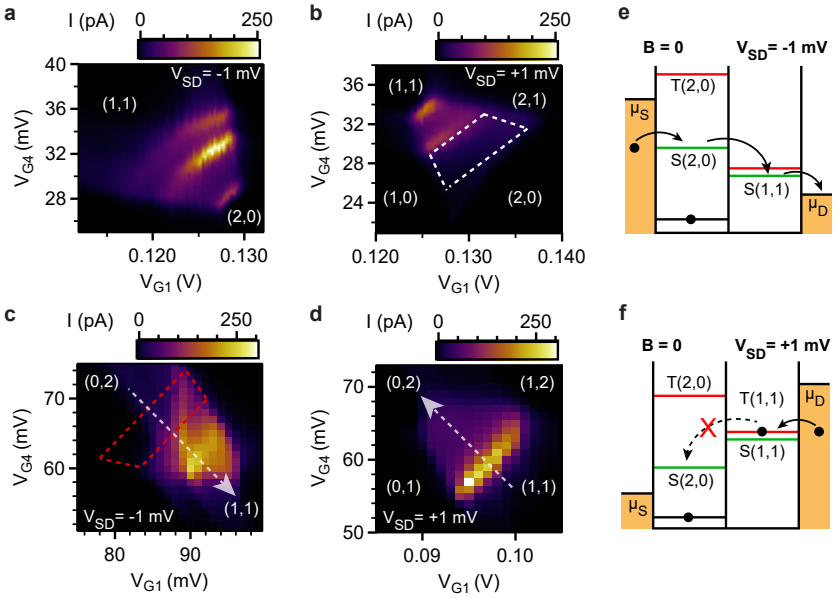

Figure 8.2. Pauli Spin Blockade at $B = 0$**. a-d** Current I as a function of gate voltages V_{G1} and V_{G4}, at **a,c** $V_{SD} = -1\,\text{mV}$ and **b,d** $V_{SD} = +1\,\text{mV}$ for the charge transitions **a,b** $(1,1) \rightarrow (2,0)$ and **c,d** $(1,1) \rightarrow (0,2)$ respectively. The region enclosed by the white and red dashed lines in **b** and **c** show current suppression due to PSB. **e,f** Energy level diagram showing electron transport process for the $(1,1) \rightarrow (2,0)$ transition at **e** $V_{SD} = -1\,\text{mV}$ and **f** $V_{SD} = +1\,\text{mV}$ respectively.

Fig. 8.2f), with the direction of current flow reversed. We note here that even in PSB, electron transport can become unblocked resulting in a finite leakage current due to coupling of the singlet and triplet states by various spin mixing mechanisms based on spin-orbit interaction [242], spin-flip cotunneling [243], hyperfine interaction [244] and g-factor differences in the DQD.

8.4. Magnetic Field Dependence

To experimentally investigate PSB, we perform magnetospectroscopy measurements by applying an in-plane external magnetic field B parallel to the FSG axes. The leakage current I as a function of V_{G1} and B along cross section C_1 and C_2 marked by the red arrow in Fig. 8.2c and Fig. 8.2d is shown in

Fig. 8.3a and Fig. 8.3b respectively. Both maps show a sharp suppression of the current at $\sim \pm 1.5\,\mathrm{T}$ irrespective of the applied bias direction, marked by the green dashed line in Fig. 8.3a,b. We identify this transition as a singlet-triplet (S-T) transition of the DQD ground state (GS) using a two electron DQD model [43, 85, 192, 245]. A schematics of the expected energy spectrum as a function of B at $V_{\mathrm{SD}} = -1\,\mathrm{mV}$ and $V_{\mathrm{SD}} = +1\,\mathrm{mV}$ is shown in Fig. 8.3e and Fig. 8.3f respectively. At $B = 0$, the triplet T(0,2) states are inaccessibly high in energy, similar to Fig. 8.2f. At finite B fields, the singlet states remains unperturbed with B, while the degeneracy of the triplet states is lifted due to Zeeman splitting, resulting in three distinguishable states T_0, T_+ and T_-. Assuming equal g-factors for the two dots, the T_- state is shifted lower in energy with B, while the T_+ shifts higher in energy such that the energy difference ΔE between the T_+ and T_- state is equal to the Zeeman splitting, i.e. $\Delta E = g\mu_{\mathrm{B}} B$.

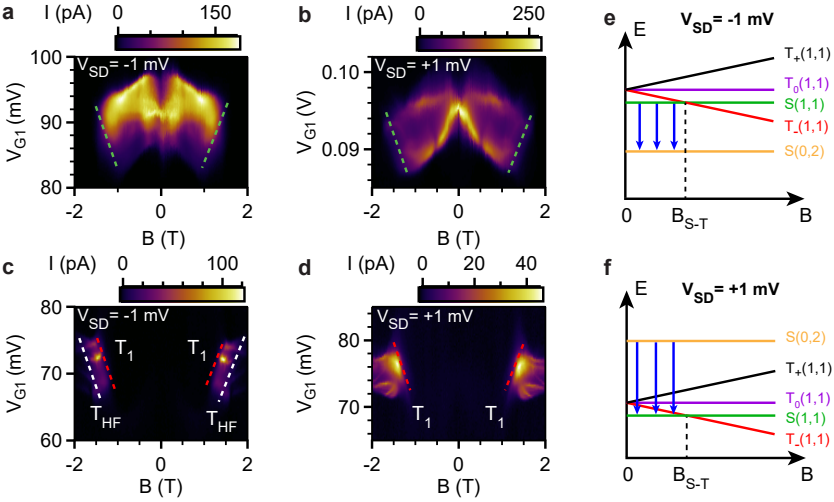

Figure 8.3. Magnetospectroscopy measurements. **a,b** Current I as a function of gate voltages V_{G1} and B along the cross section marked by white dashed arrows in **a** Fig. 8.2c and **b** Fig. 8.2d respectively. **c,d** Current I as a function of gate voltages V_{G1} and B taken along the cross section marked by green dashed line in Fig. 8.4c at **c** $V_{\mathrm{SD}} = -1\,\mathrm{mV}$ and **d** $V_{\mathrm{SD}} = +1\,\mathrm{mV}$ respectively. **e,f** Energy level diagram as a function of B for the charge transition $(1,1) \rightarrow (0,2)$ at **e** $V_{\mathrm{SD}} = -1\,\mathrm{mV}$ and **f** $V_{\mathrm{SD}} = +1\,\mathrm{mV}$ respectively

For $V_{\mathrm{SD}} = -1\,\mathrm{mV}$, the charge transport cycle through the DQD will be $(0,1) \rightarrow (1,1) \rightarrow (0,2) \rightarrow (0,1)$. For the inter-dot transition $(1,1) \rightarrow (0,2)$,

Fig. 8.3e shows that the ground state of the DQD changes from a S(1,1) state to a $T_-(1,1)$ at the S-T transition field $B_{\text{S-T}} \sim 1.5\,\text{T}$. For $B < 1.5\,\text{T}$, an electron can tunnel through the DQD via the ground state transition $S(1,1) \rightarrow S(0,2)$ (blue arrows in Fig. 8.3e) as the spin is conserved during tunneling. However, for $B > 1.5\,\text{T}$, the $T_-(1,1)$ state becomes the ground state as it shifts lower in energy than the S(1,1) state. An electron tunneling into the $T_-(1,1)$ state gets blocked as the $T(0,2)$ states are inaccessible in energy and the transition $T_-(1,1) \rightarrow S(0,2)$ is forbidden due to spin conservation. The ground state transition is hence blocked, resulting in a total suppression of current in the DQD for $B_{\text{S-T}} \geq 1.5\,\text{T}$ (Fig. 8.3a). On the other hand, the charge transport cycle through the DQD for the opposite bias direction $V_{\text{SD}} = +1\,\text{mV}$ is $(0,1) \rightarrow (0,2) \rightarrow (1,1) \rightarrow (0,1)$. Similar to the negative bias direction, an electron can tunnel via the $S(0,2) \rightarrow S(1,1)$ states for $B < 1.5\,\text{T}$ (blue arrows in Fig. 8.3f), while it gets blocked for $B > 1.5\,\text{T}$ as the $T_-(1,1)$ state becomes ground state. The ground state transition $S(0,2) \rightarrow T_-(1,1)$ is thus forbidden and the current I is suppressed beyond $B \sim 1.5\,\text{T}$, as shown in Fig. 8.3b (Fig. 8.3c and Fig. 8.3d are discussed later).

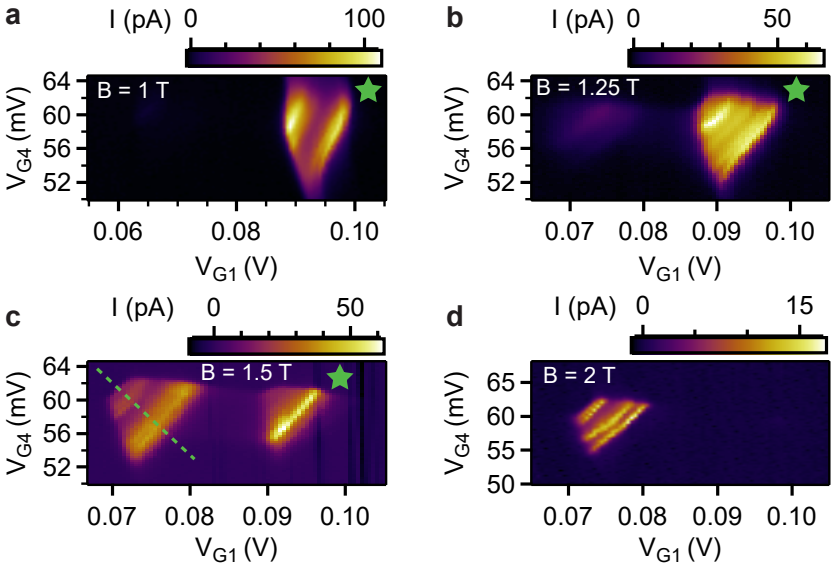

Figure 8.4. Bias Triangle Evolution with B. Current I as a function of gate voltages V_{G1} and V_{G4} for the bias triangle in Fig. 8.2d at $V_{\text{SD}} = +1\,\text{mV}$ for **a** $B = 1\,\text{T}$, **b** $B = 1.25\,\text{T}$, **c** $B = 1.5\,\text{T}$ and **d** $B = 2\,\text{T}$.

To further investigate the S-T transition, we measure current I as a function of gate voltages V_{G1} and V_{G4} at $V_{SD} = +1\,\text{mV}$ for $B = 1\,\text{T}$, $1.25\,\text{T}$, $1.5\,\text{T}$ and $2\,\text{T}$ as shown in Fig. 8.4a-d. The bias triangle for the charge transition $(0,2) \rightarrow (1,1)$, shown in Fig. 8.2d, is marked by the green star symbol in Fig. 8.4a. On increasing B from $1\,\text{T}$ to $2\,\text{T}$, we observe that the green star bias triangle completely disappears at $B \geq 1.5\,\text{T}$. Simultaneously, another bias triangle gradually begins to appear around $V_{G1} = 73\,\text{mV}$ at $B \sim 1.25\,\text{T}$ and becomes prominently visible from $B \sim 1.5\,\text{T}$ onwards. We note that the position of this new bias triangle does not have a significant shift along the V_{G4} gate axis compared to the green star marked bias triangle. In addition, the position of this emerging bias triangle fits the regular honeycomb pattern shown in Fig. 8.1c. Quantitatively, the addition energy of the QDs determined from the dimension of the corresponding hexagons taking into account the emerging bias triangle is found to be around $\sim 2.2\,\text{meV}$, which is in good agreement with the values determined from Fig. 8.1c as well as in Chapter 6. Therefore, this new bias triangle emerging at large B corresponds to a different charge transition, where the total number of electrons in the DQD is one less. The inter-dot charge transition can thus be denoted by $(-1,2) \rightarrow (0,1)$, i.e. $(N-1, M+2) \rightarrow (N, M+1)$, such that the total number of electrons in the DQD is now odd. We note that we also observe a similar characteristics of these bias triangles at the opposite bias polarity $V_{SD} = -1\,\text{mV}$.

We note that the new bias triangle is completely suppressed at $B = 0$. To explicitly understand its B dependence, we measure the current I as a function of V_{G1} at a series of external magnetic field B along the cross section C_2 marked by the green dashed line in Fig. 8.4c. Such maps for both bias directions $V_{SD} = -1\,\text{mV}$ and $V_{SD} = +1\,\text{mV}$ is shown in Fig. 8.3c and Fig. 8.3d respectively. We observe a total suppression of I until $B \sim \pm 1.5\,\text{T}$ irrespective of the bias direction. At $B = 1.5\,\text{T}$, we identify a sharp transition, termed *transition 1* (T_1), where the current suppression gets lifted as indicated by the red dashed line in Fig. 8.3c,d. We define the *slope of transition 1* as the slope of this red dashed line, which marks the onset of the transition. We find that this slope in Fig. 8.3c,d is equal to the transition slope in Fig. 8.3a,b for similar bias voltages. For same V_{SD}, the current I for the charge transition in Fig. 8.3a gets suppressed at the S-T transition $B_{S\text{-}T} \approx \pm 1.5\,\text{T}$, while simultaneously the current for the charge transition in Fig. 8.3c gets enhanced, i.e. the two transitions appear to complement each other separated by a voltage difference in V_{G1}. This is consistent with Fig. 8.4 where one bias triangle gets completely suppressed at $B_{S\text{-}T} \approx 1.5\,\text{T}$, while another bias triangle simultaneously appears at a different V_{G1}. In short, S-T transition for different charge transitions results in suppression either below or above $B_{S\text{-}T}$.

8.5. Unconventional spin blockade effect

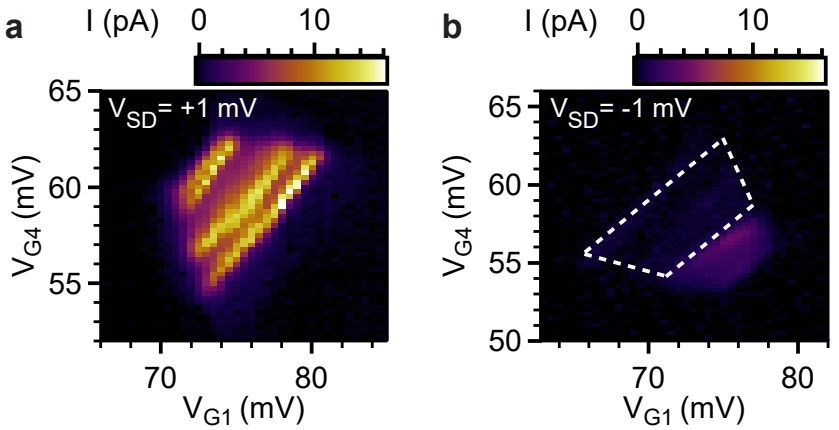

Figure 8.5. Unconventional spin blockade. Current I as a function of gate voltages V_{G1} and V_{G4} for the new emerging bias triangle at $B = 2\,\mathrm{T}$ and **a** $V_{SD} = +1\,\mathrm{mV}$ and **b** $V_{SD} = -1\,\mathrm{mV}$. The region enclosed by the white dashed lines show unconventional spin blockade with an odd number of total electrons in the DQD.

On further increasing B beyond 1.5 T, we identify another transition at $B \approx 1.75\,\mathrm{T}$ for $V_{SD} = -1\,\mathrm{mV}$ as shown by the white dashed line in Fig. 8.3c. This transition, denoted as the *high field transition* (T_{HF}), results in a total current suppression of the charge transition at $B > 1.75\,\mathrm{T}$. However, no such high field transition is observed in the mirror-symmetric $V_{SD} = +1\,\mathrm{mV}$ bias direction, in contrast to *transition 1* which was independent of the bias direction. This asymmetry in bias is investigated by measuring the corresponding bias triangle, i.e. I as a function of V_{G1} and V_{G4} at $B = 2\,\mathrm{T}$. The measured I maps for $V_{SD} = +1\,\mathrm{mV}$ and $V_{SD} = -1\,\mathrm{mV}$ is shown in Fig. 8.5a and b respectively. We observe a conductance suppression at $V_{SD} = -1\,\mathrm{mV}$ in the region enclosed by the white dashed lines in Fig. 8.5b. For $V_{SD} = +1\,\mathrm{mV}$, no such suppression in the conductance is observed (Fig. 8.5a). We denote this phenomenon as the *unconventional spin blockade* at large magnetic fields for an odd number of total electrons in the DQD, which closely resembles traditional Pauli spin blockade at $B = 0$.

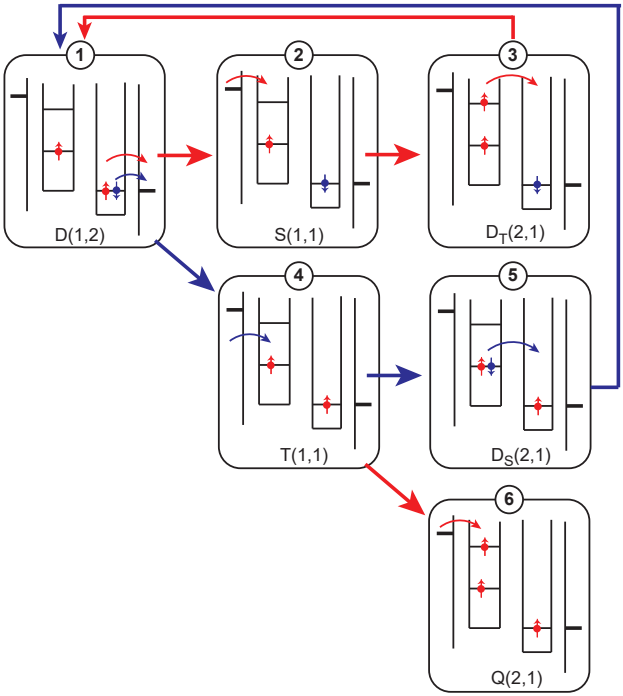

Figure 8.6. Schematics of charge and spin states and their transitions for the $(1,2) \rightarrow (1,1) \rightarrow (2,1) \rightarrow (1,2)$ charge transport cycle. Transport is blocked when the DQD achieves the state Q(2,1) with total spin $S = 3/2$ [235, 236].

8.6. Discussions and Conclusions

We now discuss the possible transport mechanisms which can result in such unconventional spin blockade with odd number of total electrons in the DQD. For the sake of simplicity, we consider the case of three electrons in the DQD system such that the interdot charge transition is $(2,1) \rightarrow (1,2)$. Thus the complete charge transfer cycle across the DQD is $(1,2) \rightarrow (1,1) \rightarrow (2,1) \rightarrow (1,2)$. At large V_{SD}, the charge state (2,1) can be classified into three sets of spin states: a doublet $D_S(2,1)$ state with total spin $S = 1/2$ and a singlet state in QD1; a doublet $D_T(2,1)$ state with total spin $S = 1/2$ and a triplet state in QD1; and a quadruplet Q(2,1) state with total spin $S = 3/2$ (see Fig. 8.6). When the Q(2,1) spin state is achieved via the tunneling pathway shown in Fig. 8.6 [235, 236], further electron transport is forbidden due to Pauli

exclusion principle. This results in a current suppression similar to standard PSB, but with an odd number of electrons in the DQD, as shown in Fig. 8.5b.

In conclusion, we demonstrated standard PSB at $B = 0$ for the interdot charge transitions with an even number of total electrons in the DQD. On applying an in-plane external magnetic field, we observe a complete suppression of the tunneling current at $B \sim 1.5\,\mathrm{T}$, consistent with the singlet-triplet ground state transition of the DQD. Simultaneously, we find an emergence of the tunneling current for an adjacent charge transition with one electron less (odd number of total electrons) in the DQD, which is completely suppressed around $B = 0$. This charge transition exhibits unconventional spin blockade effect for an odd number of total electrons in the DQD at magnetic fields $B > 1.75\,\mathrm{T}$, which can potentially occur when the DQD achieves a quadruplet spin state similar to a three electron DQD system [235, 236].

9 Summary and Outlook

To summarize, we have developed a new approach to control electron spin currents in semiconducting quantum dots (QDs) using the stray magnetic fields locally generated from individual nanomagnets. Using this approach, we demonstrated electrically tunable highly efficient spin injection and spin detection in a serial double quantum dot (DQD) at zero and small finite external magnetic fields. This efficient spin detection scheme, using Zeeman-split QDs, was then implemented in a Cooper pair splitter device to perform spin sensitive CPS experiments, demonstrating a strong negative correlation between the spin currents in the CPS device. In addition, we also demonstrated spin state engineering at very large magnetic fields for the DQD device via the Pauli spin blockade (PSB) effect.

In detail: In Chapter 5 and Ref. [105], we presented proof-of-principle magnetoconductance (MC) experiments for a single QD using local stray magnetic fields B_{str} generated from a single pair of Permalloy (Py) FSG. Using this novel approach, we demonstrated hysteretic smooth MC for multiple Coulomb blockade resonances of the single QD, which changes abruptly with the reorientation of the FSG magnetization at the characteristic FSG switching field. We observe only a single clear switching, suggesting that the two parts of the FSG switch in unison as determined by its width. We indirectly extract a stray magnetic field of $\sim 80\,\mathrm{mT}$ by exploiting the hysteretic behavior of the measured MC. In addition, we demonstrated a negligible B_{str} for a single QD located away from the FSG in the same device, which reinforces the suitability of our approach in close proximity to superconducting elements in nanoscale electronic devices. We further investigated Cobalt FSG devices, which showed a smooth change in the MC in contrast to Py, consistent with magnetocrystalline anisotropy dominating in Co strips.

Using such locally spin-polarized QDs, we demonstrated an alternative route for spin injection and spin detection in a semiconducting InAs NW device in Chapter 6 and Ref. [105]. We combined two QD-FSG units in series to form a DQD spin valve for tunneling magnetoresistance (TMR) measurements. We showed independent reorientation of the two FSG magnetizations, enabling us to establish four distinct magnetization states (two parallel and two antiparallel states) at zero external magnetic field $B = 0$. On applying a small finite external field $B = \pm 40\,\mathrm{mT}$, we demonstrated an optimized TMR signal

electrically tunable between +80% to −90% by exploiting the non-constant QD transmission DOS. This results in a gate and magnetic field tunable QD polarizations of ±80%, significantly larger than found in devices with conventional ferromagnetic contacts. Such large benchmark values demonstrates that the DQD spin valve serves as a highly efficient spin injector and detector, where electron transport can be electrically tuned from predominantly spin down electrons to spin up electrons. The demonstration of large efficiencies at such small finite fields and the location-specific nature of B_{str} as shown in Chapter 5 makes the QD-FSG units ideally compatible for detecting small spin correlated non-local signals with superconducting contacts.

In Chapter 7, we therefore implement this efficient spin detection technique by using QD-FSG units in both arms of a Cooper pair splitter device to perform spin readout of the CPS conductances. We performed bias spectroscopy to establish the formation of single QD in both arms of the CPS device as well as determine a superconducting gap of $\sim 110\,\mu$eV, which gets completely suppressed at $B \approx 90\,$mT. We demonstrated hysteretic MC in both QDs of the CPS device along with independent switching of the respective FSGs, signifying the presence of a non-zero B_{str} in each dot. This confirms the coexistence of B_{str} and superconductivity at close proximity in our device. We further demonstrated non-local signatures of Cooper pair splitting in the presence of B_{str} in one QD arm of our device. The investigation of this non-local CPS conductance for the four FSG magnetization states showed suppressed conductance for parallel magnetization states with respect to antiparallel states, consistent with the interpretation and calculation of spin cross anti-correlation for the spin singlet CPS ground state. However, spin readout of the CPS conductance simultaneously in both QD arms is still missing, which is essential for entanglement detection schemes in solid state systems.

In Chapter 8, we demonstrated electron spin state engineering via the Pauli spin blockade effect in the DQD spin valve device at very large magnetic fields, where the FSG magnetization states are always oriented in parallel in contrast to Chapter 6. We showed standard PSB at $B = 0$ for the interdot charge transitions with an even number of total electrons in the DQD. On applying an in-plane external magnetic field, we observe a complete suppression of the tunneling current at $B \sim 1.5\,$T, consistent with the singlet-triplet ground state transition of the DQD. Simultaneously, we find an emergence of the tunneling current for an adjacent charge transition with one electron less (odd number of total electrons) in the DQD, which was completely suppressed around $B = 0$. This charge transition exhibits unconventional spin blockade for an odd number of total electrons at magnetic fields $B > 1.75\,$T, which can potentially occur when the DQD achieves a quadruplet state similar to a three electron system [235, 236].

Outlook

Our spin injection and spin detection concept is not limited to InAs NWs, but can be implemented in any material device with a finite g-factor and non-constant transmission $T(E)$.

The efficiency of the TMR signal and the QD spin polarization can be further enhanced to near theoretical values by increasing B_{str}, either by reducing the FSG gap using smaller diameter NWs and precise lithography, or by using harder ferromagnetic materials such as Fe, Co. In addition, decreasing the QD lifetime broadening also leads to stronger polarization values. Such sharp line shapes with tunnel couplings $< 1\,\mu$eV have been demonstrated in in-situ grown InP tunnel barriers [83, 220, 221] as well as crystal phase engineered barriers in InAs NWs [72, 166]. Such predefined tunnel barriers also ensure precise location of the QD, enabling us to engineer homogeneous stray fields at the QD location.

For the Cooper pair splitter, the CPS splitting efficiency can be increased by reducing the tunnel coupling between S and the QD such that $\Delta >> \Gamma$. Controllable tunnel barriers can be achieved either by etching the NW with a dilute piranha solution [231], or by electrically tuning them using precise bottom gate structures [54, 55]. In addition, the direct tunneling of electrons through the NW segment beneath the superconductor can be suppressed by cutting the NW using focused ion beam (FIB) [232, 233], which ensures two completely decoupled QDs. Moreover, InP/InAs NW heterostructures with $\sim$ 200 nm apart InP barriers also ensure precisely located strong tunnel barriers, further supporting the ideal CPS working condition $\Gamma_{\mathrm{S}} << \Gamma_{\mathrm{N}}$ [121].

It has been predicted that when a normal metal is coupled to a topological superconductor with Majorana end states, electrons with spin pointing in a specific direction $\hat{n}$ are Andreev reflected as holes with the same spin [183], in contrast to ordinary Andreev reflection where the incident electron and reflected hole have opposite spin. In addition, electrons with opposite spin projection $-\hat{n}$ are totally reflected back as electrons with their spin unchanged. The QD-FSGs units are ideally suited to verify this phenomenon known as equal-spin Andreev reflection.

Furthermore, proposals for Bell tests [63, 64, 140] in a purely electronic system, i.e. with massive particles instead of photons, can be achieved by performing spin correlation measurements in a Cooper pair splitter. Using the approach demonstrated in Chapter 7, the change in the non-local CPS conductance with FSG magnetization states in both QD arms can be determined along three orthogonal directions for an entanglement witness. Although this is quite challenging to achieve, our work demonstrates that it is not impossible. In addition, an array of FSGs can be optimized to create a spatially modulating magnetic field [246] equivalent to a synthetic and externally controllable spin-orbit interaction [190, 225–227].

Bibliography

[1] G. E. Moore, Electronics Magazine **38** (1965).

[2] G. E. Moore, IEEE Solid-State Circuits Society Newsletter **11**, 36 (2006).

[3] M. M. Waldrop, Nature **530**, 144 (2016).

[4] G. A. Prinz, Physics Today **48**, 58 (1995).

[5] G. A. Prinz, Science **282**, 1660 (1998).

[6] A. Fert, Reviews of Modern Physics **80**, 1517 (2008).

[7] E. D. Herbschleb, H. Kato, Y. Maruyama, T. Danjo, T. Makino, S. Yamasaki, I. Ohki, K. Hayashi, H. Morishita, M. Fujiwara, and N. Mizuochi, Nature Communications **10** (2019), 10.1038/s41467-019-11776-8.

[8] N. Bar-Gill, L. Pham, A. Jarmola, D. Budker, and R. Walsworth, Nature Communications **4** (2013), 10.1038/ncomms2771.

[9] T. Kobayashi, J. Salfi, C. Chua, J. van der Heijden, M. G. House, D. Culcer, W. D. Hutchison, B. C. Johnson, J. C. McCallum, H. Riemann, N. V. Abrosimov, P. Becker, H.-J. Pohl, M. Y. Simmons, and S. Rogge, Nature Materials (2020), 10.1038/s41563-020-0743-3.

[10] L. M. K. Vandersypen and M. A. Eriksson, Physics Today **72**, 38 (2019).

[11] A. Hirohata, K. Yamada, Y. Nakatani, L. Prejbeanu, B. Diény, P. Pirro, and B. Hillebrands, Journal of Magnetism and Magnetic Materials , 166711 (2020).

[12] R. Jansen, Nature Materials **11**, 400 (2012).

[13] I. Žutić, J. Fabian, and S. D. Sarma, Reviews of Modern Physics **76**, 323 (2004).

[14] S. D. Sarma, J. Fabian, X. Hu, and I. Zutic, IEEE Transactions on Magnetics **36**, 2821 (2000).

[15] S. D. Sarma, J. Fabian, X. Hu, and I. Zutic, Solid state Communications **119** (2001).

[16] T. D. Ladd, F. Jelezko, R. Laflamme, Y. Nakamura, C. Monroe, and J. L. O'Brien, Nature **464**, 45 (2010).

[17] M. N. Baibich, J. M. Broto, A. Fert, F. N. V. Dau, F. Petroff, P. Etienne, G. Creuzet, A. Friederich, and J. Chazelas, Physical Review Letters **61**, 2472 (1988).

[18] G. Binasch, P. Grünberg, F. Saurenbach, and W. Zinn, Physical Review B **39**, 4828 (1989).

[19] B. Dieny, in *Magnetoelectronics* (Elsevier, 2004) pp. 67–377.

[20] T. Prevenslik, in *2013 13th IEEE International Conference on Nanotechnology (IEEE-NANO 2013)* (IEEE, 2013).

[21] R. Jansen, Journal of Physics D: Applied Physics **36**, R289 (2003).

[22] D. Abramovitch and G. Franklin, IEEE Control Systems **22**, 28 (2002).

[23] C. Chappert, A. Fert, and F. N. V. Dau, Nature Materials **6**, 813 (2007).

[24] S. Sahoo, T. Kontos, J. Furer, C. Hoffmann, M. Gräber, A. Cottet, and C. Schönenberger, Nature Physics **1**, 99 (2005).

[25] A. Hernández-Mínguez, K. Biermann, R. Hey, and P. V. Santos, Physical Review B **94** (2016), 10.1103/physrevb.94.125311.

[26] A. Cottet, C. Feuillet-Palma, and T. Kontos, Physical Review B **79** (2009), 10.1103/physrevb.79.125422.

[27] S. Datta and B. Das, Applied Physics Letters **56**, 665 (1990).

[28] M. Johnson, IEEE Spectrum **31**, 47 (1994).

[29] B. Huang, D. J. Monsma, and I. Appelbaum, Physical Review Letters **99** (2007), 10.1103/physrevlett.99.177209.

[30] V. A. Chitta, M. Z. Maialle, S. A. Leão, and M. H. Degani, Applied Physics Letters **74**, 2845 (1999).

[31] A. V. Vedyaev, Physics-Uspekhi **45**, 1296 (2002).

[32] L. P. Kouwenhoven, C. M. Marcus, P. L. McEuen, S. Tarucha, R. M. Westervelt, and N. S. Wingreen, in *Mesoscopic Electron Transport* (Springer Netherlands, 1997) pp. 105–214.

[33] L. P. Kouwenhoven, D. G. Austing, and S. Tarucha, Reports on Progress in Physics **64**, 701 (2001).

[34] R. J. Elliott, Physical Review **96**, 266 (1954).

[35] T. Tanttu, B. Hensen, K. W. Chan, C. H. Yang, W. W. Huang, M. Fogarty, F. Hudson, K. Itoh, D. Culcer, A. Laucht, A. Morello, and A. Dzurak, Physical Review X **9** (2019), 10.1103/physrevx.9.021028.

[36] I. Aleiner and V. Falko, Physical Review Letters **87** (2001).

[37] M. Governale, Physical Review Letters **89** (2002), 10.1103/physrevlett.89.206802.

[38] P. Boross, B. Dóra, A. Kiss, and F. Simon, Scientific Reports **3** (2013), 10.1038/srep03233.

[39] L. Szolnoki, A. Kiss, B. Dóra, and F. Simon, Scientific Reports **7** (2017), 10.1038/s41598-017-09759-0.

[40] L. C. Camenzind, L. Yu, P. Stano, J. D. Zimmerman, A. C. Gossard, D. Loss, and D. M. Zumbühl, Nature Communications **9** (2018), 10.1038/s41467-018-05879-x.

[41] E. R. Andrew, Physics Bulletin **24**, 741 (1973).

[42] D. D. Awschalom, L. C. Bassett, A. S. Dzurak, E. L. Hu, and J. R. Petta, Science **339**, 1174 (2013).

[43] D. Loss and D. P. DiVincenzo, Physical Review A **57**, 120 (1998).

[44] C. Kloeffel and D. Loss, Annual Review of Condensed Matter Physics **4**, 51 (2013).

[45] C. H. Bennett and D. P. DiVincenzo, Nature **404**, 247 (2000).

[46] X. Hu and S. D. Sarma, Physical Review A **64** (2001), 10.1103/physreva.64.042312.

[47] L. R. Schreiber and H. Bluhm, Science **359**, 393 (2018).

[48] N. Gisin, G. Ribordy, W. Tittel, and H. Zbinden, Reviews of Modern Physics **74**, 145 (2002).

[49] M. Bashar, M. Chowdhury, R. Islam, M. Rahman, and S. Das, in *2009 International Conference on Computer and Automation Engineering* (IEEE, 2009).

[50] R. Horodecki, P. Horodecki, M. Horodecki, and K. Horodecki, Reviews of Modern Physics **81**, 865 (2009).

[51] J. Bardeen, L. N. Cooper, and J. R. Schrieffer, Physical Review **108**, 1175 (1957).

[52] L. Hofstetter, S. Csonka, J. Nygård, and C. Schönenberger, Nature **461**, 960 (2009).

[53] L. Hofstetter, S. Csonka, A. Baumgartner, G. Fülöp, S. d'Hollosy, J. Nygård, and C. Schönenberger, Physical Review Letters **107** (2011), 10.1103/physrevlett.107.136801.

[54] G. Fülöp, S. d'Hollosy, A. Baumgartner, P. Makk, V. Guzenko, M. Madsen, J. Nygård, C. Schönenberger, and S. Csonka, Physical Review B (2014).

[55] G. Fülöp, F. Domínguez, S. d'Hollosy, A. Baumgartner, P. Makk, M. Madsen, V. Guzenko, J. Nygård, C. Schönenberger, A. L. Yeyati, and S. Csonka, Physical Review Letters **115** (2015), 10.1103/physrevlett.115.227003.

[56] A. Das, Y. Ronen, M. Heiblum, D. Mahalu, A. V. Kretinin, and H. Shtrikman, Nature Communications **3** (2012), 10.1038/ncomms2169.

[57] S. Baba, C. Jünger, S. Matsuo, A. Baumgartner, Y. Sato, H. Kamata, K. Li, S. Jeppesen, L. Samuelson, H. Q. Xu, C. Schönenberger, and S. Tarucha, New Journal of Physics **20**, 063021 (2018).

[58] L. G. Herrmann, F. Portier, P. Roche, A. L. Yeyati, T. Kontos, and C. Strunk, Physical Review Letters **104** (2010), 10.1103/physrevlett.104.026801.

[59] J. Schindele, A. Baumgartner, and C. Schönenberger, Physical Review Letters **109** (2012), 10.1103/physrevlett.109.157002.

[60] Z. Tan, D. Cox, T. Nieminen, P. Lähteenmäki, D. Golubev, G. Lesovik, and P. Hakonen, Physical Review Letters **114** (2015), 10.1103/physrevlett.114.096602.

[61] I. V. Borzenets, Y. Shimazaki, G. F. Jones, M. F. Craciun, S. Russo, M. Yamamoto, and S. Tarucha, Scientific Reports **6** (2016), 10.1038/srep23051.

[62] B. Braunecker, P. Burset, and A. L. Yeyati, Physical Review Letters **111** (2013), 10.1103/physrevlett.111.136806.

[63] N. M. Chtchelkatchev, G. Blatter, G. B. Lesovik, and T. Martin, Physical Review B **66** (2002), 10.1103/physrevb.66.161320.

[64] G. Lesovik, T. Martin, and G. Blatter, The European Physical Journal B **24**, 287 (2001).

[65] S. Csonka, L. Hofstetter, F. Freitag, S. Oberholzer, C. Schönenberger, T. Jespersen, M. Aagesen, and J. Nygård, Nano Letters **8** (2008).

[66] H. A. Nilsson, P. Caroff, C. Thelander, M. Larsson, J. B. Wagner, L.-E. Wernersson, L. Samuelson, and H. Q. Xu, Nano Letters **9**, 3151 (2009).

[67] J. Gramich, *Andreev and Spin Transport in Carbon Nanotube Quantum Dot Hybrid Devices*, Ph.D. thesis, University of Basel (2016).

[68] G. Abulizi, *Quantum transport in hexagonal boron nitride carbon nanotube heterostructures*, Ph.D. thesis, University of Basel (2017).

[69] J. Schindele, *Observation of Cooper Pair Splitting and Andreev Bound States in Carbon Nanotubes*, Ph.D. thesis, University of Basel (2014).

[70] G. Fabian, *Engineered Magnetoconductance in InAs Nanowire Quantum Dots*, Ph.D. thesis, University of Basel (2015).

[71] M. T. Deng, S. Vaitiekėnas, E. B. Hansen, J. Danon, M. Leijnse, K. Flensberg, J. Nygård, P. Krogstrup, and C. M. Marcus, Science **354**, 1557 (2016).

[72] M. Nilsson, L. Namazi, S. Lehmann, M. Leijnse, K. A. Dick, and C. Thelander, Physical Review B **93** (2016), 10.1103/physrevb.93.195422.

[73] M. Nilsson, L. Namazi, S. Lehmann, M. Leijnse, K. A. Dick, and C. Thelander, Physical Review B **94** (2016), 10.1103/physrevb.94.115313.

[74] S. Wang, N. Kharche, E. C. Girão, X. Feng, K. Müllen, V. Meunier, R. Fasel, and P. Ruffieux, Nano Letters **17**, 4277 (2017).

[75] S. J. Tans, M. H. Devoret, H. Dai, A. Thess, R. E. Smalley, L. J. Geerligs, and C. Dekker, Nature **386**, 474 (1997).

[76] G. Abulizi, A. Baumgartner, and C. Schönenberger, physica status solidi (b) **253**, 2428 (2016).

[77] M. Jung, J. Schindele, S. Nau, M. Weiss, A. Baumgartner, and C. Schönenberger, Nano Letters **13**, 4522 (2013).

[78] J. Weis, R. J. Haug, K. v. Klitzing, and K. Ploog, Physical Review Letters **71**, 4019 (1993).

[79] L. P. Kouwenhoven, N. C. van der Vaart, A. T. Johnson, W. Kool, C. J. P. M. Harmans, J. G. Williamson, A. A. M. Staring, and C. T. Foxon, Zeitschrift für Physik B Condensed Matter **85**, 367 (1991).

[80] L. J. Klein, K. A. Slinker, J. L. Truitt, S. Goswami, K. L. M. Lewis, S. N. Coppersmith, D. W. van der Weide, M. Friesen, R. H. Blick, D. E. Savage, M. G. Lagally, C. Tahan, R. Joynt, M. A. Eriksson, J. O. Chu, J. A. Ott, and P. M. Mooney, Applied Physics Letters **84**, 4047 (2004).

[81] M. Eich, R. Pisoni, A. Pally, H. Overweg, A. Kurzmann, Y. Lee, P. Rickhaus, K. Watanabe, T. Taniguchi, K. Ensslin, and T. Ihn, Nano Letters **18**, 5042 (2018).

[82] R. T. Tung, Applied Physics Reviews **1**, 011304 (2014).

[83] F. Thomas, A. Baumgartner, L. Gubser, C. Jünger, G. Fülöp, M. Nilsson, F. Rossi, V. Zannier, L. Sorba, and C. Schoenenberger, Nanotechnology (2019), 10.1088/1361-6528/ab5ce6.

[84] E. A. Laird, F. Kuemmeth, G. A. Steele, K. Grove-Rasmussen, J. Nygård, K. Flensberg, and L. P. Kouwenhoven, Reviews of Modern Physics **87**, 703 (2015).

[85] R. Hanson, L. P. Kouwenhoven, J. R. Petta, S. Tarucha, and L. M. K. Vandersypen, Reviews of Modern Physics **79**, 1217 (2007).

[86] F. S. Thomas, *Deterministic Tunnel Barriers in One-Dimensional Quantum Electronic Systems*, Ph.D. thesis, University of Basel (2020).

[87] T. Ihn, *Semiconductor Nanostructures* (Oxford University Press, 2009).

[88] C. W. J. Beenakker, Physical Review B **44**, 1646 (1991).

[89] S. D. Franceschi, S. Sasaki, J. M. Elzerman, W. G. van der Wiel, S. Tarucha, and L. P. Kouwenhoven, Physical Review Letters **86**, 878 (2001).

[90] P. ZEEMAN, Nature **55**, 347 (1897).

[91] R. S. Deacon, Y. Kanai, S. Takahashi, A. Oiwa, K. Yoshida, K. Shibata, K. Hirakawa, Y. Tokura, and S. Tarucha, Physical Review B **84** (2011), 10.1103/physrevb.84.041302.

[92] C. E. Pryor and M. E. Flatté, Physical Review Letters **96** (2006), 10.1103/physrevlett.96.026804.

[93] A. De and C. E. Pryor, Physical Review B **76** (2007), 10.1103/physrevb.76.155321.

[94] K. Ono, H. Shimada, and Y. Ootuka, Journal of the Physical Society of Japan **67**, 2852 (1998).

[95] H. Shimada, K. Ono, and Y. Ootuka, Journal of Applied Physics **93**, 8259 (2003).

[96] S. J. van der Molen, N. Tombros, and B. J. van Wees, Physical Review B **73** (2006), 10.1103/physrevb.73.220406.

[97] W. G. van der Wiel, S. D. Franceschi, J. M. Elzerman, T. Fujisawa, S. Tarucha, and L. P. Kouwenhoven, Reviews of Modern Physics **75**, 1 (2002).

[98] W. Pfaff, D. Weinmann, W. Heusler, B. Kramer, and U. Weiss, Zeitschrift fur Physik B Condensed Matter **96**, 201 (1994).

[99] K. Ono, Science **297**, 1313 (2002).

[100] S. Joachim, Siegmann, and H. Christoph, *Magnetism* (Springer Berlin Heidelberg, 2006).

[101] M. Getzlaff, *Fundamentals of Magnetism* (Springer Berlin Heidelberg, 2006).

[102] A. Friedman, in *Mathematics in Industrial Problems* (Springer New York, 1992) pp. 182–192.

[103] C. Tannous and J. Gieraltowski, European Journal of Physics **29**, 475 (2008).

[104] E. C. Stoner and E. P. Wohlfarth, Trans. Roy. Soc. (London) **A240** (1948).

[105] A. Bordoloi, V. Zannier, L. Sorba, C. Schönenberger, and A. Baumgartner, Communications Physics **3** (2020), 10.1038/s42005-020-00405-2.

[106] H. Aurich, A. Baumgartner, F. Freitag, A. Eichler, J. Trbovic, and C. Schönenberger, Applied Physics Letters **97**, 153116 (2010).

[107] I. I. Mazin, Physical Review Letters **83**, 1427 (1999).

[108] N. Mott, Advances in Physics **13**, 325 (1964).

[109] A. Fert and I. A. Campbell, Physical Review Letters **21**, 1190 (1968).

[110] R. Meservey and P. Tedrow, Physics Reports **238**, 173 (1994).

[111] E. I. Rashba, Physical Review B **62**, R16267 (2000).

[112] M. Jullière, Physics Letters A **54**, 225 (1975).

[113] T. McGuire and R. Potter, IEEE Transactions on Magnetics **11**, 1018 (1975).

[114] J. Samm, J. Gramich, A. Baumgartner, M. Weiss, and C. Schönenberger, Journal of Applied Physics **115**, 174309 (2014).

[115] W. Meissner and R. Ochsenfeld, Die Naturwissenschaften **21**, 787 (1933).

[116] V. L. Ginzburg, Il Nuovo Cimento **2**, 1234 (1955).

[117] A. Andreev, JETP **19** (1964).

[118] G. E. Blonder, M. Tinkham, and T. M. Klapwijk, Physical Review B **25**, 4515 (1982).

[119] A. Kleine, A. Baumgartner, J. Trbovic, and C. Schönenberger, EPL (Europhysics Letters) **87**, 27011 (2009).

[120] G. Falci, D. Feinberg, and F. W. J. Hekking, Europhysics Letters (EPL) **54**, 255 (2001).

[121] P. Recher, E. V. Sukhorukov, and D. Loss, Physical Review B **63** (2001), 10.1103/physrevb.63.165314.

[122] D. B. Suyatin, C. Thelander, M. T. Björk, I. Maximov, and L. Samuelson, Nanotechnology **18**, 105307 (2007).

[123] C. H. Jünger, *Transport Spectroscopy of Semiconductor Superconductor Nanowire Hybrid Devices*, Ph.D. thesis, University of Basel (2019).

[124] F. Pobell, *Matter and Methods at Low Temperatures* (Springer Berlin Heidelberg, 2007).

[125] Y.-S. Kim, K. Hummer, and G. Kresse, Physical Review B **80** (2009), 10.1103/physrevb.80.035203.

[126] N. Gupta, Y. Song, G. W. Holloway, U. Sinha, C. M. Haapamaki, R. R. LaPierre, and J. Baugh, Nanotechnology **24**, 225202 (2013).

[127] S. Dayeh, D. P. Aplin, X. Zhou, P. K. Yu, E. Yu, and D. Wang, Small **3**, 326 (2007).

[128] A. C. Ford, J. C. Ho, Y.-L. Chueh, Y.-C. Tseng, Z. Fan, J. Guo, J. Bokor, and A. Javey, Nano Letters **9**, 360 (2009).

[129] M. B. Rota, A. S. Ameruddin, H. A. Fonseka, Q. Gao, F. Mura, A. Polimeni, A. Miriametro, H. H. Tan, C. Jagadish, and M. Capizzi, Nano Letters **16**, 5197 (2016).

[130] T. S. Jespersen, M. Aagesen, C. Sørensen, P. E. Lindelof, and J. Nygård, Physical Review B **74** (2006), 10.1103/physrevb.74.233304.

[131] C. Fasth, A. Fuhrer, L. Samuelson, V. N. Golovach, and D. Loss, Physical Review Letters **98** (2007), 10.1103/physrevlett.98.266801.

[132] S. Nadj-Perge, S. M. Frolov, E. P. A. M. Bakkers, and L. P. Kouwenhoven, Nature **468**, 1084 (2010).

[133] Y. Oreg, G. Refael, and F. von Oppen, Physical Review Letters **105** (2010), 10.1103/physrevlett.105.177002.

[134] M.-T. Deng, S. Vaitiekėnas, E. Prada, P. San-Jose, J. Nygård, P. Krogstrup, R. Aguado, and C. M. Marcus, Physical Review B **98** (2018), 10.1103/physrevb.98.085125.

[135] D. Rainis, L. Trifunovic, J. Klinovaja, and D. Loss, Physical Review B **87** (2013), 10.1103/physrevb.87.024515.

[136] L. Fu, Physical Review Letters **104** (2010), 10.1103/physrevlett.104.056402.

[137] M. Leijnse and K. Flensberg, Physical Review B **84** (2011), 10.1103/physrevb.84.140501.

[138] J. Alicea, Y. Oreg, G. Refael, F. von Oppen, and M. P. A. Fisher, Nature Physics **7**, 412 (2011).

[139] D. Aasen, M. Hell, R. V. Mishmash, A. Higginbotham, J. Danon, M. Leijnse, T. S. Jespersen, J. A. Folk, C. M. Marcus, K. Flensberg, and J. Alicea, Physical Review X **6** (2016), 10.1103/physrevx.6.031016.

[140] W. Kłobus, A. Grudka, A. Baumgartner, D. Tomaszewski, C. Schönenberger, and J. Martinek, Physical Review B **89** (2014), 10.1103/physrevb.89.125404.

[141] F. Vigneau, V. Prudkovkiy, I. Duchemin, W. Escoffier, P. Caroff, Y.-M. Niquet, R. Leturcq, M. Goiran, and B. Raquet, Physical Review Letters **112** (2014), 10.1103/physrevlett.112.076801.

[142] S. Dhara, H. S. Solanki, V. Singh, A. Narayanan, P. Chaudhari, M. Gokhale, A. Bhattacharya, and M. M. Deshmukh, Physical Review B **79** (2009), 10.1103/physrevb.79.121311.

[143] S. F. Karg, V. Troncale, U. Drechsler, P. Mensch, P. D. Kanungo, H. Schmid, V. Schmidt, L. Gignac, H. Riel, and B. Gotsmann, Nanotechnology **25**, 305702 (2014).

[144] R. S. Wagner and W. C. Ellis, Applied Physics Letters **4**, 89 (1964).

[145] X. Yan, X. Zhang, X. Ren, H. Huang, J. Guo, X. Guo, M. Liu, Q. Wang, S. Cai, and Y. Huang, Nano Letters **11**, 3941 (2011).

[146] M. Tchernycheva, L. Travers, G. Patriarche, F. Glas, J.-C. Harmand, G. E. Cirlin, and V. G. Dubrovskii, Journal of Applied Physics **102**, 094313 (2007).

[147] L. E. Jensen, M. T. Björk, S. Jeppesen, A. I. Persson, B. J. Ohlsson, and L. Samuelson, Nano Letters **4**, 1961 (2004).

[148] U. P. Gomes, D. Ercolani, V. Zannier, S. Battiato, E. Ubyivovk, V. Mikhailovskii, Y. Murata, S. Heun, F. Beltram, and L. Sorba, Nanotechnology **28**, 065603 (2017).

[149] K. A. Dick, K. Deppert, T. Mårtensson, B. Mandl, L. Samuelson, and W. Seifert, Nano Letters **5**, 761 (2005).

[150] P. Caroff, K. A. Dick, J. Johansson, M. E. Messing, K. Deppert, and L. Samuelson, Nature Nanotechnology **4**, 50 (2008).

[151] A. I. Hochbaum, R. Fan, R. He, and P. Yang, Nano Letters **5**, 457 (2005).

[152] P. H. M. Böttger, Z. Bi, D. Adolph, K. A. Dick, L. S. Karlsson, M. N. A. Karlsson, B. A. Wacaser, and K. Deppert, Nanotechnology **18**, 105304 (2007).

[153] U. P. Gomes, D. Ercolani, V. Zannier, F. Beltram, and L. Sorba, Semiconductor Science and Technology **30**, 115012 (2015).

[154] T. Mårtensson, P. Carlberg, M. Borgström, L. Montelius, W. Seifert, and L. Samuelson, Nano Letters **4**, 699 (2004).

[155] K. A. Dick, C. Thelander, L. Samuelson, and P. Caroff, Nano Letters **10**, 3494 (2010).

[156] S. Lehmann, J. Wallentin, D. Jacobsson, K. Deppert, and K. A. Dick, Nano Letters **13**, 4099 (2013).

[157] J. Gooth, M. Borg, H. Schmid, V. Schaller, S. Wirths, K. Moselund, M. Luisier, S. Karg, and H. Riel, Nano Letters **17**, 2596 (2017).

[158] F. Krizek, T. Kanne, D. Razmadze, E. Johnson, J. Nygård, C. M. Marcus, and P. Krogstrup, Nano Letters **17**, 6090 (2017).

[159] S. Gazibegovic, D. Car, H. Zhang, S. C. Balk, J. A. Logan, M. W. A. de Moor, M. C. Cassidy, R. Schmits, D. Xu, G. Wang, P. Krogstrup, R. L. M. O. het Veld, K. Zuo, Y. Vos, J. Shen, D. Bouman, B. Shojaei, D. Pennachio, J. S. Lee, P. J. van Veldhoven, S. Koelling, M. A. Verheijen, L. P. Kouwenhoven, C. J. Palmstrøm, and E. P. A. M. Bakkers, Nature **548**, 434 (2017).

[160] S. R. Plissard, I. van Weperen, D. Car, M. A. Verheijen, G. W. G. Immink, J. Kammhuber, L. J. Cornelissen, D. B. Szombati, A. Geresdi, S. M. Frolov, L. P. Kouwenhoven, and E. P. A. M. Bakkers, Nature Nanotechnology **8**, 859 (2013).

[161] P. Krogstrup, N. L. B. Ziino, W. Chang, S. M. Albrecht, M. H. Madsen, E. Johnson, J. Nygård, C. M. Marcus, and T. S. Jespersen, Nature Materials **14**, 400 (2015).

[162] M. Bjergfelt, D. J. Carrad, T. Kanne, M. Aagesen, E. M. Fiordaliso, E. Johnson, B. Shojaei, C. J. Palmstrøm, P. Krogstrup, T. S. Jespersen, and J. Nygård, Nanotechnology **30**, 294005 (2019).

[163] D. J. Carrad, M. Bjergfelt, T. Kanne, M. Aagesen, F. Krizek, E. M. Fiordaliso, E. Johnson, J. Nygård, and T. S. Jespersen, Advanced Materials **32**, 1908411 (2020).

[164] M. T. Björk, B. J. Ohlsson, T. Sass, A. I. Persson, C. Thelander, M. H. Magnusson, K. Deppert, L. R. Wallenberg, and L. Samuelson, Nano Letters **2**, 87 (2002).

[165] V. Zannier, F. Rossi, D. Ercolani, and L. Sorba, Nanotechnology **30**, 094003 (2019).

[166] C. Jünger, A. Baumgartner, R. Delagrange, D. Chevallier, S. Lehmann, M. Nilsson, K. A. Dick, C. Thelander, and C. Schönenberger, Communications Physics **2** (2019), 10.1038/s42005-019-0162-4.

[167] Z. Liu, Z. Zhang, R. Jiang, X. Li, M. Zhang, and D. Qiu, Scripta Materialia **121**, 79 (2016).

[168] D. Kriegner, C. Panse, B. Mandl, K. A. Dick, M. Keplinger, J. M. Persson, P. Caroff, D. Ercolani, L. Sorba, F. Bechstedt, J. Stangl, and G. Bauer, Nano Letters **11**, 1483 (2011).

[169] A. C. Ford, S. B. Kumar, R. Kapadia, J. Guo, and A. Javey, Nano Letters **12**, 1340 (2012).

[170] A. E. Hansen, M. T. Björk, C. Fasth, C. Thelander, and L. Samuelson, Physical Review B **71** (2005), 10.1103/physrevb.71.205328.

[171] M. Speckbacher, J. Treu, T. J. Whittles, W. M. Linhart, X. Xu, K. Saller, V. R. Dhanak, G. Abstreiter, J. J. Finley, T. D. Veal, and G. Koblmüller, Nano Letters **16**, 5135 (2016).

[172] Y. Xiong, H. Tang, X. Wang, Y. Zhao, Q. Fu, J. Yang, and D. Xu, Scientific Reports **7** (2017), 10.1038/s41598-017-13792-4.

[173] M. J. L. Sourribes, I. Isakov, M. Panfilova, and P. A. Warburton, Nanotechnology **24**, 045703 (2013).

[174] D. Liang and X. P. Gao, Nano Letters **12**, 3263 (2012).

[175] I. van Weperen, B. Tarasinski, D. Eeltink, V. S. Pribiag, S. R. Plissard, E. P. A. M. Bakkers, L. P. Kouwenhoven, and M. Wimmer, Physical Review B **91** (2015), 10.1103/physrevb.91.201413.

[176] A. Pfund, I. Shorubalko, K. Ensslin, and R. Leturcq, Physical Review B **76** (2007), 10.1103/physrevb.76.161308.

[177] Y. Kanai, R. S. Deacon, S. Takahashi, A. Oiwa, K. Yoshida, K. Shibata, K. Hirakawa, Y. Tokura, and S. Tarucha, Nature Nanotechnology **7**, 75 (2011).

[178] S. Heedt, N. T. Ziani, F. Crépin, W. Prost, S. Trellenkamp, J. Schubert, D. Grützmacher, B. Trauzettel, and T. Schäpers, Nature Physics **13**, 563 (2017).

[179] M. Pioro-Ladrière, T. Obata, Y. Tokura, Y.-S. Shin, T. Kubo, K. Yoshida, T. Taniyama, and S. Tarucha, Nature Physics **4**, 776 (2008).

[180] M. Pioro-Ladrière, Y. Tokura, T. Obata, T. Kubo, and S. Tarucha, Applied Physics Letters **90**, 024105 (2007).

[181] Z. Su, A. B. Tacla, M. Hocevar, D. Car, S. R. Plissard, E. P. A. M. Bakkers, A. J. Daley, D. Pekker, and S. M. Frolov, Nature Communications **8** (2017), 10.1038/s41467-017-00665-7.

[182] S. Vaitiekėnas, Y. Liu, P. Krogstrup, and C. M. Marcus, (2020).

[183] J. J. He, T. Ng, P. A. Lee, and K. Law, Physical Review Letters **112** (2014), 10.1103/physrevlett.112.037001.

[184] J. Klinovaja, P. Stano, and D. Loss, Physical Review Letters **109** (2012), 10.1103/physrevlett.109.236801.

[185] J. Klinovaja and D. Loss, Physical Review Letters **110** (2013), 10.1103/physrevlett.110.126402.

[186] J. Klinovaja and D. Loss, Physical Review B **90** (2014), 10.1103/physrevb.90.045118.

[187] D. Rainis, A. Saha, J. Klinovaja, L. Trifunovic, and D. Loss, Physical Review Letters **112** (2014), 10.1103/physrevlett.112.196803.

[188] D. Rainis and D. Loss, Physical Review B **90** (2014), 10.1103/physrevb.90.235415.

[189] A. Saha, D. Rainis, R. P. Tiwari, and D. Loss, Physical Review B **90** (2014), 10.1103/physrevb.90.035422.

[190] M. M. Desjardins, L. C. Contamin, M. R. Delbecq, M. C. Dartiailh, L. E. Bruhat, T. Cubaynes, J. J. Viennot, F. Mallet, S. Rohart, A. Thiaville, A. Cottet, and T. Kontos, Nature Materials **18**, 1060 (2019).

[191] O. Malkoc, C. Bergenfeldt, and P. Samuelsson, EPL (Europhysics Letters) **105**, 47013 (2014).

[192] G. Fábián, P. Makk, M. H. Madsen, J. Nygård, C. Schönenberger, and A. Baumgartner, Physical Review B **94** (2016), 10.1103/physrevb.94.195415.

[193] R. P. G. McNeil, R. J. Schneble, M. Kataoka, C. J. B. Ford, T. Kasama, R. E. Dunin-Borkowski, J. M. Feinberg, R. J. Harrison, C. H. W. Barnes, D. H. Y. Tse, T. Trypiniotis, J. A. C. Bland, D. Anderson, G. A. C. Jones, and M. Pepper, Nano Letters **10**, 1549 (2010).

[194] R. P. Cowburn, D. K. Koltsov, A. O. Adeyeye, M. E. Welland, and D. M. Tricker, Physical Review Letters **83**, 1042 (1999).

[195] S. Zihlmann, *Spin and charge relaxation in graphene*, Ph.D. thesis, University of Basel (2018).

[196] H. D. Arnold and G. W. Elmen, Bell System Technical Journal **2**, 101 (1923).

[197] X. Mi, M. Benito, S. Putz, D. M. Zajac, J. M. Taylor, G. Burkard, and J. R. Petta, Nature **555**, 599 (2018).

[198] F. Borjans, X. G. Croot, X. Mi, M. J. Gullans, and J. R. Petta, Nature **577**, 195 (2019).

[199] A. Corna, L. Bourdet, R. Maurand, A. Crippa, D. Kotekar-Patil, H. Bohuslavskyi, R. Laviéville, L. Hutin, S. Barraud, X. Jehl, M. Vinet, S. D. Franceschi, Y.-M. Niquet, and M. Sanquer, npj Quantum Information **4** (2018), 10.1038/s41534-018-0059-1.

[200] T. Dietl and H. Ohno, Reviews of Modern Physics **86**, 187 (2014).

[201] A. Fert, N. Reyren, and V. Cros, Nature Reviews Materials **2** (2017), 10.1038/natrevmats.2017.31.

[202] V. Baltz, A. Manchon, M. Tsoi, T. Moriyama, T. Ono, and Y. Tserkovnyak, Reviews of Modern Physics **90** (2018), 10.1103/revmodphys.90.015005.

[203] J. M. Elzerman, R. Hanson, L. H. W. van Beveren, B. Witkamp, L. M. K. Vandersypen, and L. P. Kouwenhoven, Nature **430**, 431 (2004).

[204] P. Chuang, S.-C. Ho, L. W. Smith, F. Sfigakis, M. Pepper, C.-H. Chen, J.-C. Fan, J. P. Griffiths, I. Farrer, H. E. Beere, G. A. C. Jones, D. A. Ritchie, and T.-M. Chen, Nature Nanotechnology **10**, 35 (2014).

[205] K.-R. Jeon, C. Ciccarelli, A. J. Ferguson, H. Kurebayashi, L. F. Cohen, X. Montiel, M. Eschrig, J. W. A. Robinson, and M. G. Blamire, Nature Materials **17**, 499 (2018).

[206] W. Han, S. Maekawa, and X.-C. Xie, Nature Materials (2019), 10.1038/s41563-019-0456-7.

[207] T. Nakajima, A. Noiri, J. Yoneda, M. R. Delbecq, P. Stano, T. Otsuka, K. Takeda, S. Amaha, G. Allison, K. Kawasaki, A. Ludwig, A. D. Wieck, D. Loss, and S. Tarucha, Nature Nanotechnology **14**, 555 (2019).

[208] J.-C. L. Breton, S. Sharma, H. Saito, S. Yuasa, and R. Jansen, Nature **475**, 82 (2011).

[209] B. Varaprasad, A. Srinivasan, Y. Takahashi, M. Hayashi, A. Rajanikanth, and K. Hono, Acta Materialia **60**, 6257 (2012).

[210] N. A. Spaldin and R. Ramesh, Nature Materials **18**, 203 (2019).

[211] Z. Yang, B. Heischmidt, S. Gazibegovic, G. Badawy, D. Car, P. A. Crowell, E. P. Bakkers, and V. S. Pribiag, Nano Letters **20**, 3232 (2020).

[212] B. T. Jonker, G. Kioseoglou, A. T. Hanbicki, C. H. Li, and P. E. Thompson, Nature Physics **3**, 542 (2007).

[213] D. D. Awschalom and M. E. Flatté, Nature Physics **3**, 153 (2007).

[214] A. Bernand-Mantel, P. Seneor, K. Bouzehouane, S. Fusil, C. Deranlot, F. Petroff, and A. Fert, Nature Physics **5**, 920 (2009).

[215] R. Hanson, L. M. K. Vandersypen, L. H. W. van Beveren, J. M. Elzerman, I. T. Vink, and L. P. Kouwenhoven, Physical Review B **70** (2004), 10.1103/physrevb.70.241304.

[216] J. A. Folk, R. Potok, C. Marcus, and V. Umansky, Science **299**, 679 (2003).

[217] R. M. Potok, J. A. Folk, C. M. Marcus, and V. Umansky, Physical Review Letters **89** (2002), 10.1103/physrevlett.89.266602.

[218] V. Mourik, K. Zuo, S. M. Frolov, S. R. Plissard, E. P. A. M. Bakkers, and L. P. Kouwenhoven, Science **336**, 1003 (2012).

[219] H. Zhang, C.-X. Liu, S. Gazibegovic, D. Xu, J. A. Logan, G. Wang, N. van Loo, J. D. S. Bommer, M. W. A. de Moor, D. Car, R. L. M. O. het Veld, P. J. van Veldhoven, S. Koelling, M. A. Verheijen, M. Pendharkar, D. J. Pennachio, B. Shojaei, J. S. Lee, C. J. Palmstrøm, E. P. A. M. Bakkers, S. D. Sarma, and L. P. Kouwenhoven, Nature **556**, 74 (2018).

[220] A. Fuhrer, L. E. Fröberg, J. N. Pedersen, M. W. Larsson, A. Wacker, M.-E. Pistol, and L. Samuelson, Nano Letters **7**, 243 (2007).

[221] S. Roddaro, A. Pescaglini, D. Ercolani, L. Sorba, and F. Beltram, Nano Letters **11**, 1695 (2011).

[222] C. Jünger, R. Delagrange, D. Chevallier, S. Lehmann, K. A. Dick, C. Thelander, J. Klinovaja, D. Loss, A. Baumgartner, and C. Schönenberger, Physical Review Letters **125** (2020), 10.1103/physrevlett.125.017701.

[223] T. Obata, M. Pioro-Ladrière, Y. Tokura, Y.-S. Shin, T. Kubo, K. Yoshida, T. Taniyama, and S. Tarucha, Physical Review B **81** (2010), 10.1103/physrevb.81.085317.

[224] S. Sun, Science **287**, 1989 (2000).

[225] B. Braunecker, G. I. Japaridze, J. Klinovaja, and D. Loss, Physical Review B **82** (2010), 10.1103/physrevb.82.045127.

[226] M. Kjaergaard, K. Wölms, and K. Flensberg, Physical Review B **85** (2012), 10.1103/physrevb.85.020503.

[227] J. J. Viennot, M. C. Dartiailh, A. Cottet, and T. Kontos, Science **349**, 408 (2015).

[228] N. Brunner, D. Cavalcanti, S. Pironio, V. Scarani, and S. Wehner, Reviews of Modern Physics **86**, 419 (2014).

[229] R. Ursin, F. Tiefenbacher, T. Schmitt-Manderbach, H. Weier, T. Scheidl, M. Lindenthal, B. Blauensteiner, T. Jennewein, J. Perdigues, P. Trojek, B. Ömer, M. Fürst, M. Meyenburg, J. Rarity, Z. Sodnik, C. Barbieri, H. Weinfurter, and A. Zeilinger, Nature Physics **3**, 481 (2007).

[230] J. Gramich, A. Baumgartner, and C. Schönenberger, Physical Review Letters **115** (2015), 10.1103/physrevlett.115.216801.

[231] G. Fülöp, S. d'Hollosy, L. Hofstetter, A. Baumgartner, J. Nygård, C. Schönenberger, and S. Csonka, Nanotechnology **27**, 195303 (2016).

[232] J. Naik, P. Prewett, K. Das, and A. Raychaudhuri, Microelectronic Engineering **88**, 2840 (2011).

[233] X. Sun and K. Cheng, in *Micromanufacturing Engineering and Technology* (Elsevier, 2015) pp. 35–59.

[234] Z. Scherübl, G. Fülöp, C. P. Moca, J. Gramich, A. Baumgartner, P. Makk, T. Elalaily, C. Schönenberger, J. Nygård, G. Zaránd, and S. Csonka, Nature Communications **11** (2020), 10.1038/s41467-020-15322-9.

[235] S. Amaha, W. Izumida, T. Hatano, S. Teraoka, S. Tarucha, J. A. Gupta, and D. G. Austing, Physical Review Letters **110** (2013), 10.1103/physrevlett.110.016803.

[236] S. Amaha, W. Izumida, T. Hatano, S. Tarucha, K. Kono, and K. Ono, Physical Review B **89** (2014), 10.1103/physrevb.89.085302.

[237] J.-Y. Wang, G.-Y. Huang, S. Huang, J. Xue, D. Pan, J. Zhao, and H. Xu, Nano Letters **18**, 4741 (2018).

[238] R. Li, F. E. Hudson, A. S. Dzurak, and A. R. Hamilton, Nano Letters **15**, 7314 (2015).

[239] N. S. Lai, W. H. Lim, C. H. Yang, F. A. Zwanenburg, W. A. Coish, F. Qassemi, A. Morello, and A. S. Dzurak, Scientific Reports **1** (2011), 10.1038/srep00110.

[240] T. Fujita, P. Stano, G. Allison, K. Morimoto, Y. Sato, M. Larsson, J.-H. Park, A. Ludwig, A. Wieck, A. Oiwa, and S. Tarucha, Physical Review Letters **117** (2016), 10.1103/physrevlett.117.206802.

[241] A. C. Johnson, J. R. Petta, C. M. Marcus, M. P. Hanson, and A. C. Gossard, Physical Review B **72** (2005), 10.1103/physrevb.72.165308.

[242] S. Nadj-Perge, S. M. Frolov, J. W. W. van Tilburg, J. Danon, Y. V. Nazarov, R. Algra, E. P. A. M. Bakkers, and L. P. Kouwenhoven, Physical Review B **81** (2010), 10.1103/physrevb.81.201305.

[243] M. Brauns, J. Ridderbos, A. Li, E. P. A. M. Bakkers, W. G. van der Wiel, and F. A. Zwanenburg, Physical Review B **94** (2016), 10.1103/physrevb.94.041411.

[244] F. H. L. Koppens, Science **309**, 1346 (2005).

[245] M. Wagner, U. Merkt, and A. V. Chaplik, Physical Review B **45**, 1951 (1992).

[246] K. Szulc, F. Lisiecki, A. Makarov, M. Zelent, P. Kuświk, H. Głowiński, J. W. Kłos, M. Münzenberg, R. Gieniusz, J. Dubowik, F. Stobiecki, and M. Krawczyk, Physical Review B **99** (2019), 10.1103/physrevb.99.064412.

A Fabrication Recipes

The fabrication techniques used in this thesis are discussed in chapter 3. This appendix provides details of the fabrication recipes.

A.1. Fabrication of InAs NW Devices

A.1.1. Wafer Characteristics

- **Substrate Material:** Highly doped Silicon
- **Dopant:** p-type, Boron
- **Resistivity:** $0.003 - 0.005\,\Omega\mathrm{m}$
- **Capping Layer:** 400 nm thick thermally grown SiO_2

A.1.2. Wafer Cleaning

1. Dice the wafer into 2.5 cm x 2.5 cm pieces.
2. Sonicate in acetone for ~ 20 min.
3. Sonicate in IPA for ~ 20 min.
4. Blow dry with N_2

A.2. E-beam Lithography, Development and Lift-off

A.2.1. PMMA resist for contacts and etching

- **Resist:** PMMA 950K dissolved in Anisole.
- **Spin Coating:** 4000 RPM for 40s resulting in a thickness of $\sim 300\,\mathrm{nm}$.
- **Baking:** 180°C on a hotplate for 5 minutes.
- **Area Dose:** $240\,\mu\mathrm{C/cm^2}$ at 20 kV and high current mode

- **Development:** 3:1 Isopropyl alcohol (IPA) / Methylisobutyl ketone (MIBK) for 60 seconds followed by a dip in IPA and blow dry with N_2.
- **Liftoff:** 30 minutes in 50°C warm acetone.

A.2.2. ZEP resist for Permalloy FSGs

- **Resist:** ZEP520A resist dissolved in the ratio 6:1 ZEP:Anisole.
- **Spin Coating:** 4000 RPM for 40s resulting in a thickness of $\sim 300\,\text{nm}$.
- **Baking:** 180°C on a hotplate for 3 minutes.
- **Area Dose:** $35\,\mu\text{C/cm}^2$ at 10 kV.
- **Development:** Pentylacetate for 60 seconds, followed by MIBK:IPA (9:1 ratio) for 10 seconds and blow dry with N_2.
- **Liftoff:** 30 minutes in 80°C N-Methyl-2-pyrrolidone (NMP).

A.3. Reactive ion etching - O_2 Plasma Etching

This process is used to remove residue with PMMA resist only.

- **Parameters:**
  - **O_2 Flow:** 16 %
  - **RF Power:** 30 W
  - **Process Pressure:** 250 mTorr
  - **Time:** 60 s
- **Etch Rates:**
  - **SiO_2:** negligible
  - **PMMA:** ∼20 nm/min

A.4. Etching of the NW native oxide

A.4.1. Sulphur passivation

1. Dilute 0.96195 g Sulfur in 10 mL of 20 % NH_4S_x.
2. Stir for at least 12 hours at 35 °C.
3. Filter 2.5 mL of NH_4S_x to remove sulfur residues.

4. Heat 25 mL of H_2O on a hotplate at 40 °C for minimum 10 min.
5. Add NH_4S_x right before etching, otherwise it degrades very fast.
6. Etch for 210 seconds on the hotplate.
7. Stop etching by stirring in H_2O for 20 seconds.
8. Blow dry with N_2 and immediately put the sample in vacuum.

A.5. Contacts

A.5.1. Ti/Au contacts

This process is used for the base structures and normal metal contacts and gates.

1. **Type:** E-beam evaporation in the Sharon.
2. Pump to a base pressure of $\sim 9e^{-7}$ mbar.
3. Evaporate 5 nm of Ti (0.5 Å per second).
4. Evaporate 45 nm of Au (1.0 Å per second).

A.5.2. Ti/Al contacts

This process is used for Al as the superconducting contact.

1. **Type:** E-beam evaporation in the Balzers.
2. Pump to a base pressure of $\sim 5e^{-7}$ mbar.
3. Evaporate 5 nm of Ti (0.5 Å per second).
4. Evaporate 65 nm of Au (1.4 Å per second).

A.5.3. Permalloy Evaporation

This process is used for Permalloy (Py) as the ferromagnetic material for the FSGs.

1. **Type:** E-beam evaporation in the Balzers.
2. Pump to a base pressure of $\sim 5e^{-7}$ mbar.
3. Evaporate 30-35 nm of Py (0.6 Å per second).

B Additional data on a double quantum dot spin valve

B.1. Determination of B_{switch}

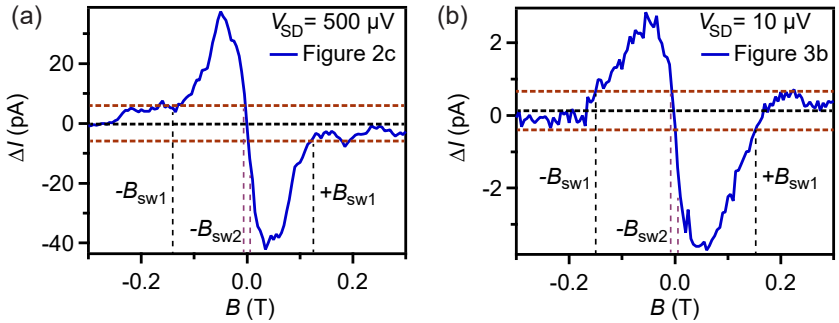

Figure B.1. Determination of FSG switching fields. (a) $\Delta I = I_{\mathrm{up}}^{\mathrm{max}} - I_{\mathrm{down}}^{\mathrm{max}}$ as a function of B for the experiment in Figure 2c at $V_{\mathrm{SD}} = 500\,\mu\mathrm{V}$. (b) ΔI as a function of B for the experiment in Figure 3b at $V_{\mathrm{SD}} = 10\,\mu\mathrm{V}$.

To determine the characteristic switching fields B_{sw} of the FSGs in the DQD-SV, we plot $\Delta I = I_{\mathrm{up}}^{\mathrm{max}} - I_{\mathrm{down}}^{\mathrm{max}}$ as a function of B in figure B.1a, where $I_{\mathrm{up}}^{\mathrm{max}}$ and $I_{\mathrm{down}}^{\mathrm{max}}$ refer to the up and down sweep in figure 2c of the main text, measured at $V_{\mathrm{SD}} = 500\,\mu\mathrm{V}$. We assign an average zero level of the measured data, shown as black dashed line and define a lower and upper current limit for a significant deviation of ΔI from the average zero. We use the B values at which the upper horizontal line meets ΔI as the two switching fields, $B_{\mathrm{sw1}} \approxeq 140\,\mathrm{mT}$ and $B_{\mathrm{sw2}} \approxeq 5\,\mathrm{mT}$, respectively. We use a similar analysis for the lower horizontal line. We point out that a similar analysis of Figure 3b, i.e. on a different resonance, results in the same switching fields, as shown in figure B.1b.

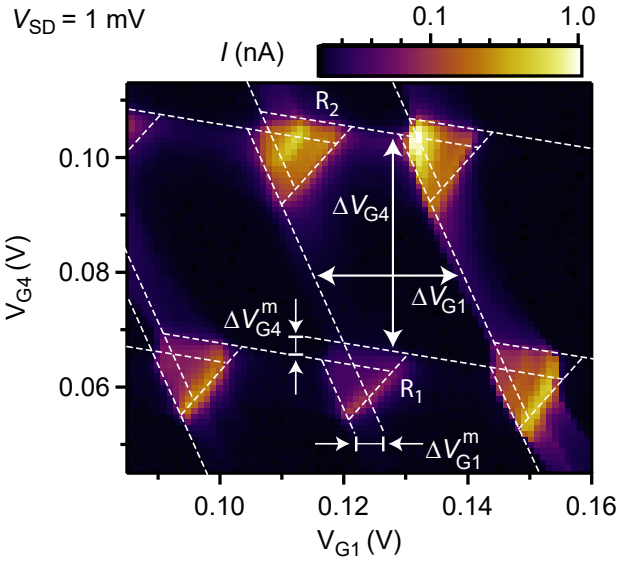

Figure B.2. Characterization of the double quantum dot. Colorscale plot of the current I as a function of V_{G1} and V_{G4} at $V_{SD} = 1$ mV.

B.2. DQD Characterization

Figure B.2 shows the current I as a function of V_{G1} and V_{G4} at $V_{SD} = 1$ mV to characterize the weakly-coupled serial DQD. The other gates are kept constant at $V_{BG} = -0.25$ V, $V_{G2} = -0.2$ V and $V_{G3} = 0.0$ V. From the honeycomb structure [97], we obtain $\Delta V_{G1} = 25$ mV, $\Delta V_{G4} = 30$ mV, $\Delta V^{m}_{G1} = 3$ mV and $\Delta V^{m}_{G4} = 4$ mV, as shown in figure B.2. The capacitance between the QD and the respective gate is given by: $C_G = e/\Delta V_G$. We find $C_{G1} = 6.4$ aF and $C_{G4} = 5.94$ aF to the respective QD. The total capacitances of the two QDs are $C_1 = 64$ aF and $C_2 = 65.2$ aF, while the mutual capacitance is $C_m = 7$ aF. The addition energy of the QDs are $E_{add,1} \approx 2.5$ meV and $E_{add,2} \approx 2.7$ meV, while the level spacings are $\delta E_1 \approx 0.7$ meV and $\delta E_2 \approx 0.81$ meV, respectively. The lever arms for both dots are found as: $a_{11} \approx 0.1$, $a_{12} \approx 0.015$, $a_{21} \approx 0.0$ and $a_{22} \approx 0.09$, i.e. the cross lever arms are one order of magnitude smaller than the direct lever arms.

B.3. Width and Position of the DQD-SV resonances

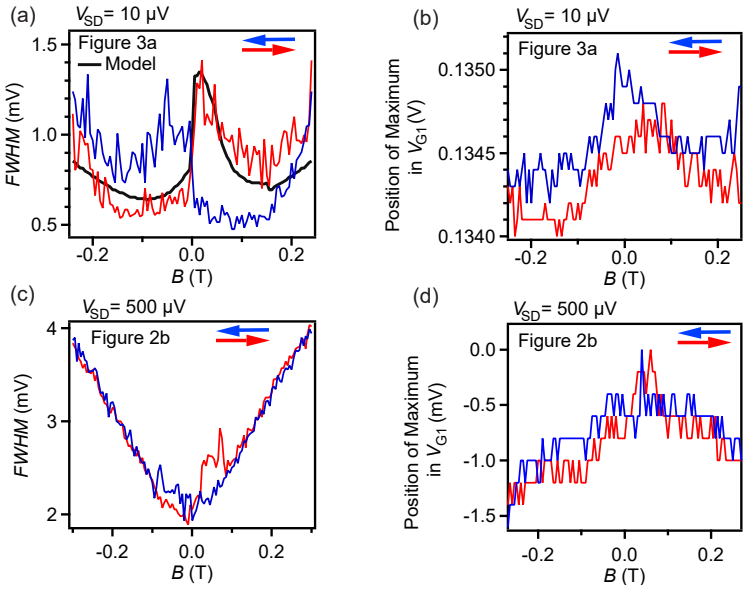

Figure B.3. FWHM and position of the resonance maximum. (a) Full width at half maximum (FWHM) of the DQD-SV resonance as a function of B for the up (red) and down (blue) sweep for the experiments in Figure 3a at $V_{SD} = 10\,\mu$V. The black line shows the FWHM obtained from the resonant tunneling model using the same parameters as in the main text. (b) Position of the current maximum in V_{G1} as a function of B for the up (red) and down (blue) sweep for experiments in Figure 3a at $V_{SD} = 10\,\mu$V. (c) FWHM as a function of B for the up (red) and down (blue) sweep for experiments in Figure 2b at $V_{SD} = 500\,\mu$V. (d) Position of the current maximum in V_{G1} as a function of B for the up (red) and down (blue) sweep for experiments in Figure 2b.

B.4. Bias Triangle for the Four Magnetization States

The current I as a function of V_{G1} and V_{G4} for the four magnetization states at $B = \pm 40\,$mT and $V_{SD} = 10\mu$V is shown in Figure B.4. The $(-,-)$ and $(+,-)$ magnetization states were measured at $B = -40\,$mT, while the $(+,+)$ and $(-,+)$ magnetization states were measured at $B = +40\,$mT. For the same

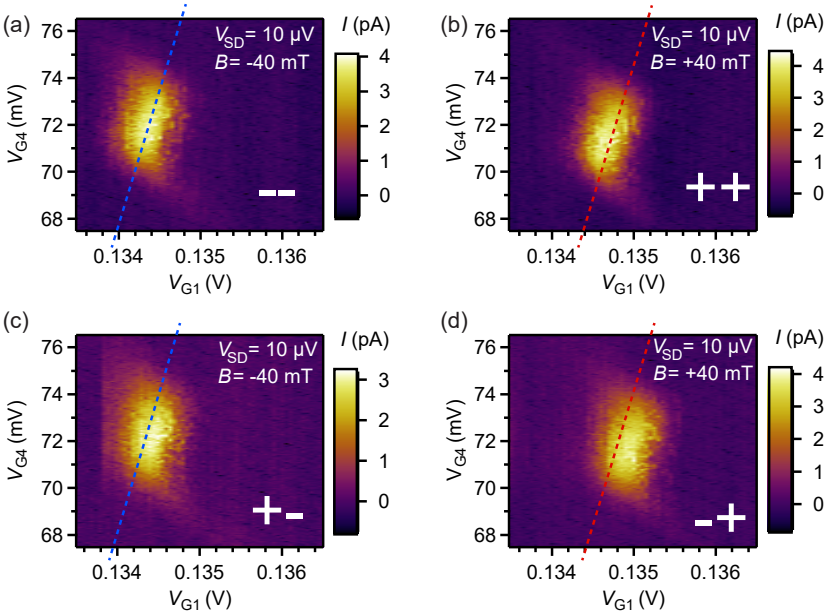

Figure B.4. Bias triangles for four magnetization states. I as a function of V_{G1} and V_{G4} for the magnetization state (a) $(-,-)$ at $B = -40\,\mathrm{mT}$ (b) $(+,+)$ at $B = +40\,\mathrm{mT}$ (c) $(+,-)$ at $B = -40\,\mathrm{mT}$ and (d) $(-,+)$ at $B = +40\,\mathrm{mT}$, measured at $V_{SD} = 10\mu\mathrm{V}$. The dashed red and blue lines are guide to the eyes.

B, we observe that the anti-parallel states are shifted in V_{G1} relative to the parallel states. For example, at $B = +40\,\mathrm{mT}$, the total magnetic field $B_{tot}^{(1)}$ at QD 1 changes when the FSG magnetization state switches from $(+,+)$ to $(-,+)$. This consequently changes the transmission DoS of QD1 at E_F, resulting in a shift of the bias triangle position in V_{G1}. We observe a similar shift in V_{G1} for the magnetization states $(-,-)$ and $(+,-)$ at $B = -40\,\mathrm{mT}$, thereby enabling us to optimize the TMR signal.

B.5. Analysis of a Third Resonance

We present additional data (figure B.5a) for the cross section C_3 of bias triangle R_2 in Figure 1d of the main text. I as a function of V_{G1} and B are clearly hysteretic for the up and down sweep, mirrored around $B = 0$. The hysteresis

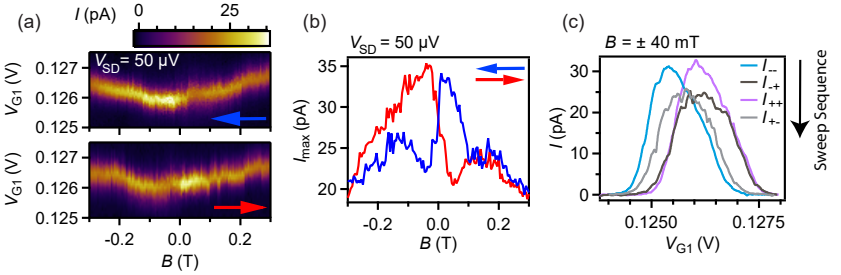

Figure B.5. Data for resonance R_2 in figure 1d of the main text. (a) I as a function of V_{G1} and B for the up (red) and down (blue) sweep for $V_{SD} = 50\mu V$ measured along the cross section C_3 in Figure 1d. (b) I_{max} vs B for the up and down sweeps extracted from B.5a. (c) I as a function of V_{G1} for the four magnetization states measured at $B = \pm 40$ mT along the cross section C_4 in Figure 1d, parametrized by V_{G1}.

is clearly visible in the I_{max} vs B curves (figure B.5b) extracted from figure B.5a, showing similar characteristics as the resonance in figure 3b. In addition, we measure I as a function of V_{G1} for each magnetization state at $B = \pm 40$ mT along the cross section C_4 (figure 1d), similar to figure 3c in the main text. The $(-,-)$ [blue] and $(+,-)$ [grey] magnetization states in Figure B.5c were measured at $B = -40$ mT, while the $(+,+)$ [purple] and $(-,+)$ [black] magnetization states were measured at $B = +40$ mT. Similar to Fig 3c, we observe a suppression of 11% in I for the anti-parallel magnetizations relative to the parallel ones.

The resonances R_1 and R_2 as well as resonance A in Figure 2 in the main text can be reproduced by the resonant tunneling model with very similar parameters, as summarized in table S1. The B_{str1} and B_{str2} values mentioned in the main text are consistent with all the observed resonances. The model curves for the four magnetization states at $B = \pm 40\,\mathrm{mT}$ along cross section C_2 (figure 1d in the main text), reproducing the experiments of Figure 3c is shown in Figure B.6.

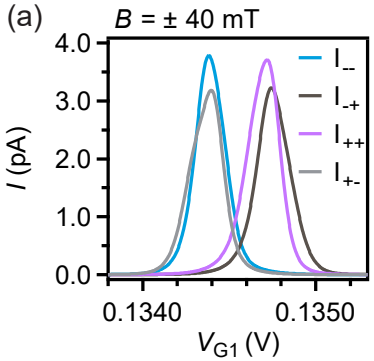

Figure B.6. Resonant tunneling model. (a) I as a function of V_{G1} extracted from the resonant tunneling model for all four magnetization states at $B = \pm 40$ mT, reproducing experiments in Figure 3c of the main text. The $(-,-)$ [blue] and $(+,-)$ [grey] magnetization states are measured at $B = -40$ mT, while the $(+,+)$ [purple] and $(-,+)$ [black] magnetization states measured at $B = +40$ mT.

Resonance	g_1	g_2	$E_2^{(0)}$ (μeV)
R_1 Up sweep	5.2 - 5.9	6.1 - 6.5	7.5 - 8.5
R_1 Down sweep	5.0 - 5.6	6.1 - 6.5	7.5 - 8.5
A (Figure 2)	5.8 - 6.5	5.0 - 6.0	8.0 - 13.0
R_2	5.0 - 5.6	5.1 - 5.4	8.0 - 9.0

Table B.1. Summary of the parameters extracted from the resonant tunneling model for the three resonances measured (g-factors and energy offset $E^{(0)}$ of the two QDs).

Curriculum Vitae

Arunav Bordoloi
Born on 28th July, 1994 in Tinsukia, Assam, India

Education

9/2016–9/2020	**PhD in Experimental Physics at the University of Basel, Switzerland**
	- Dissertation in the group of Prof. Dr. Christian Schönenberger *"Spin Projection and Correlation Experiments in Nanoelectronic Devices"*
8/2011–8/2016	**Bachelor of Science and Master of Science in Physics at Indian Institute of Science Education and Research, Kolkata, India**
	- Master thesis in the group of Prof. Chiranjib Mitra *"Microwave Cavity Perturbation on $NH_4CuPO_4.H_2O$ Single Crystals and YBCO Thin Films at Low Temperatures"*
2009–2011	**High School at Army Public School, Narangi, India**

Positions

9/2016–	Teaching assistant for physics at the University of Basel
5/2015–7/2015	Research intern in the group of Prof. Chiranjib Mitra at the Indian Institute of Science Education and Research, Kolkata, India *'Broadband Microwave Analysis of High-T_c Superconducting Thin Films using Corbino Geometry"*
5/2014–7/2014	Research intern in the group of Prof. Fabien Bretenaker at the Laboratoire Aime Cotton, Ecole Polytechnique, CNRS, France *"Phase Sensitive Amplification in Nonlinear Optical Fibers"*

5/2013–7/2013	Research intern in the group of Dr. Anil K. Pandey at the Aryabhatta Research Institute of Observational Sciences, Nainital, India
	"A Multiwavelength Polarimetric Study towards the Open Cluster Stock 8"

Scholarships and Awards

2019	*Best poster prize at the international conference "One-Dimensional Systems for Quantum Technology" 2019*
2011–2015	*INSPIRE Scholarship*
2014	*Charpak Scholarship*
2013	*Summer Research Fellowship, Indian Academy of Sciences*
2012	*Delegation of India,* 6^{th} *Asian Science Camp, Israel*

Publications

- *"Spin readout in a Cooper pair splitter"*
  A. Bordoloi, V. Zannier, L. Sorba, C. Schönenberger and A. Baumgartner
  in preparation

- *"Unconventional Pauli spin blockade at large in-plane magnetic fields"*
  A. Bordoloi, V. Zannier, L. Sorba, C. Schönenberger and A. Baumgartner
  in preparation

- *"A double quantum dot spin valve"*
  A. Bordoloi, V. Zannier, L. Sorba, C. Schönenberger and A. Baumgartner
  Communications Physics **3**, 135 (2020)

Talks

- *A double quantum dot spin valve*
  QCQT Research Seminar, Basel (Switzerland), December 2019

- *Towards Synthetic Spin-Orbit Interaction in InAs Nanowires using Ferromagnetic Sidegates*
  Summer school "Transport in Nanostructures" Capri (Italy), April 2017

Poster Contributions

- *"Transport Spectroscopy in Semiconducting Nanowire Electronic Devices"*
  QSIT General Meeting, Arosa (Switzerland), February 2020

- *"Double Quantum Dot Tunneling Magnetoresistance without Ferromagnetic Contacts"*
  One-Dimensional Systems for Quantum Technology, Bad Honnef (Germany), June 2019, poster prize.

- *"Quantum Transport in Semiconducting Nanowires"*
  Symposium Basel-Freiburg, Basel (Switzerland), 2018

- *"Towards Synthetic Spin-Orbit Interaction in InAs Nanowires using Ferromagnetic Sidegates"*
  NCCR QSIT Quantum Systems and Technology, Monte Verita (Switzerland), May 2018

- *"Novel quantum transport features in low-dimensional systems"*
  QSIT Winter School, Arosa (Switzerland), February 2017

Acknowledgements

When I first arrived in Basel in early September 2016, it was a nice sunny Autumn day with people swimming in the Rhine at a temperature of 22°C. I had just arrived from $>$ 40°C hot and humid India, where 20°C would have been extreme winter for me. The new place felt so different to what I was accustomed back home. Yet the group was very nice and friendly, and the physics seemed very interesting. Looking backwards now after four years, I can definitely say that it has been one of the most exciting and important period of my life. This would not have been possible without the help, contribution and support of numerous people to the four years of research in the Quantum Nanoelectronics group at University of Basel and, more importantly, towards the many amazing moments in this important period of life. Therefore, I would like to sincerely express my gratitude and cherish the precious support from each of you.

First of all, I would like to thank my advisor Prof. Dr. Christian Schönenberger for giving me the opportunity and freedom to explore whatever I wanted in my PhD project. Thank you for your never-ending enthusiasm and passion for physics, which has really fascinated me the last four years. I genuinely admire your ability to ask the tough right questions at the right moment, which always challenges one to think beyond the conventional. Looking back, it was one such tough session of questioning during my first year review meeting, which motivated me to work hard and seek deeper insight in my work. Thank you for pushing me hard that day. It was the perfect medication I needed to turn around my PhD. Thank you for the words “You, Arunav, you will make it" that day. I have always remembered these words thereafter and strived my best to respect the trust you put on me. I am also very thankful for the very informal atmosphere you have created in the group, which has allowed me to combine my research and personal life perfectly. The group trips and the Christmas dinners were always fun and enjoyable. Furthermore, your kindness, support and encouragement at tough times is something that I will always try to achieve myself. Your encouragement to not give up after failures, especially after the initial negative reviewer comments on our paper, was very inspiring. Overall, it was a very wonderful and rewarding four years working with you, Christian. I wholeheartedly appreciate you for making all these possible and hope, one day, I too can become a leader and kind person

like you.

Secondly, I would like to thank Prof. Dr. Thomas Schäpers and Prof. Dr. Takis Kontos for taking out the time and effort to read my thesis. It is a great privilege to have two such excellent physicists in my PhD defense committee.

I am also very grateful to Dr. Andreas Baumgartner. This thesis would never have been possible without the enormous contribution and support from you. Thank you for continuously supporting me when things were unfavorable in the project. I still remember one such day when I was very unsure about the project due to repeated unclear measurements in the lab. The 2-hour pep talk over lunch at the mensa terrace, where you explained me the roadmap ahead and motivated me to fabricate more, worked wonders. Surprisingly, the next device I fabricated and measured was the working DQD spin valve device. I would also like to thank you for the enormous freedom you gave me and unlimited patience you showed while interpreting the spin valve data. I would always come to you after every half an hour when I figured out an equation or found something new in the data while trying to understand our results. You never said "No, I don't have time now" to any such discussions, although you clearly had other things to do. I will always cherish this amazing support and empathy during the ups and downs in my research. In addition, I am grateful to you for teaching me so many things — measurement setups, cryostat operating principle, helium transfer, fabrication in the cleanroom (although it did not go very well! We cleaved the chip into hundreds of pieces), scientific writing and the multiple MATLAB programs, from which I picked up countless new functions and codes. Thank you so much for everything, and I hope we will continue similarly for the coming experiments, and maybe future endeavors as well.

I would also like to thank our collaborators in Pisa, Dr. Valentina Zannier and Prof. Dr. Lucia Sorba, for growing the amazing NWs without which the thesis would not have been possible. The high quality NWs you sent us served as the material platform for all the experiments in this thesis. I would also like to thank Dr. Joost Ridderbos and Dr. Gergo Fülöp for all their efforts with Qcodes, which made all the measurements possible.

I have shared my whole PhD time here with four amazing colleagues in the group - Dr. Frederick Thomas, Dr. Lujun Wang, Dr. Christian Jünger and soon-to-be-Dr. David Indolese. With Frederick Thomas, I shared a lot of time chilling outside the department while taking a break from the lab. They were always enjoyable due to his lame one-liner jokes and gossips and provided the much-needed refreshment from research. I also enjoyed skiing with him at Kanderstag, and hope we can ski again in the winter of 2020. In addition, thank you very much for proof reading parts of my thesis. With Lujun Wang, I did a lot of things together - from playing badminton until he destroyed his wrist, to swimming and hill biking in the Jura, where we simply pushed our bikes up three hills. These were really fun along with the several dinners we

went for exploring buffet Chinese food around Basel. I also enjoyed the ski trip to Feldberg although we did not ski together that day, and hope we can continue doing so while you are in Zurich. Christian Jünger was the first guy to teach me fabrication when I first arrived in Basel. Thank you for helping me start my thesis and also for the many barbecues which you organized as well as the 'elephant' joke you created from your creativity. It was a wonderful time knowing you. I started my PhD at the same time as David Indolese. The rowing competition in Mohlin was really fun and my first time at competitive rowing. It was surprising that we finished last in the race with two Swiss champions in our boat, nevertheless it was amazing. The subsequent fresh water Fischknusperli was amazing.

More recently, I also shared some wonderful time with some amazing colleagues. With Alessia Pally, I had the privilege of organizing the group trip, where I pushed her to call the hotel multiple times for booking our trip, which she clearly hated doing so. It was an amazing trip, with awesome and clear weather. Thank you for also taking out time to quickly read parts of my thesis as well as bring me lunch multiple times without any hesitation during my thesis writing. This was very kind of you. With Blesson Sam Varghese and Paritosh Karnatak, I enjoyed a lot participating in cricket tournaments as well as playing football, badminton and volleyball outside the lab. It was crazy that our team "The Wisden Philosophers" had the courage to compete against semi-professional teams without proper gears and training. Thank you also for the many dinners together.

Furthermore, I would like to thank all former and current members of the Nanoelectronics group: Gergő Fülöp, Jörg Gramich, Thomas Hasler, Simon, Zihlmann, Clevin Handschin, Vishal Ranjan, Kishan Todkar, Gulibusitan Abulizi, Roy Haller, Peter Makk, Maria El Abbassi, Mihai-Cezar Harabula, Jann Overbeck, Anton Vladyka, Michel Calame, Artem Kononov, MArtin Endres, Luk Yi Cheung, Ian Correa Sampaio, Olivier Faist, Lukas Gubser, Zarina Mingazheva, Mehdi Ramezani, Jann Ungerer, Carlo Ciaccia, Dario Sufra, Melissa Osterwalder, Libin Wang, Han Zheng and Matthijs Hermans.

Although the Physics department in Basel is known for its research, very few people know about the phenomenal people working behind the scenes at the Department. Barbara Kammermann and Astrid Kalt were the best secretaries I ever met, from whom I got extremely helpful and kind assistance in all administrative work. I am especially thankful to Sascha Martin and his excellent team at the mechanical workshop, who always helped us with new parts for the cryostats. I would also like to thank Dominik Sifrig for the regular supply of helium, Patrick Stöcklin for the help in the cryolab, Daniel Sacker and Laurent Marot for the help with the DI water system.

Here in Basel, I have met many people whose friendship I would appreciate all my life. Special thanks to Carmen Necibi, Debdeep Ghosal, Debashish Koner, Debsankar De, Padmabati Mondal, Manisha Thakurathi, Rejaul SK,

Shantanu Roy, Aisha Ahsan and Yashpreet Kaur. Thank you very much for the awesome get-togethers, dinners (all the mouthwatering food that I will never be capable of cooking) and the crazy trip to Mallorca, Spain and the nice one to Belgium. It was a great pleasure participating in so many hikes and events with you all. You guys are a family to me away from home. I would also like to thank my college friends, Purba Kashyap and Sneha Ray Sarkar, for the wonderful hiking trips in the Alps as well as in Italy. With them, I could always talk about the stress and frustrations of a PhD, and get some nice advices and suggestions. I hope we can continue going on such trips in the future as well.

Furthermore, I am very grateful to my parents, Rupanjoli and Nogen, for their continuous support and care for me while I stayed far away from them. I would certainly be not here without the contribution of my parents. Thanks to my brother, Attrishu, for bearing me being away for such a long time. Their understanding and encouragement gave me a lot of strength to get through the hard times away from home.

Thank you all very much. Without you all, the PhD life would not have been so fulfilling. You all will be forever cherished in this chapter of my life.